DOCTOR OF ENGINEERING (ENGD)

Techniques for monitoring ionospheric dynamics

Cooper, Chelsey Amber

Award date:
2019

Awarding institution:
University of Bath

TECHNIQUES FOR MONITORING IONOSPHERIC DYNAMICS

Chelsey Amber Cooper

A thesis submitted for the degree of Doctor of Engineering

University of Bath

Department of Electronic and Electrical Engineering

September 2018

Abstract

Fluctuations in the ionospheric electron density can have consequences for a range of terrestrial systems including satellites, navigation and communications. Accurate modelling of these fluctuations is needed to ensure that affected systems perform effectively. Enhancing our understanding of the ionosphere can help to improve ionospheric models. In this project changes in the ionosphere are studied using existing and new approaches to enhance our understanding. The parameters investigated are the E region critical frequency (foE) and the corresponding height (hmE), F region critical frequency (foF2) and corresponding height (hmF2), and total electron content (TEC). These parameters were observed by ionosondes, and by a new technique that analyses signals transmitted between geostationary satellites of the Global Positioning System (GPS) constellation and single frequency receivers on the ground.

Ionosonde data were analysed over six Decembers, and GPS TEC over a full year. foF2 and GPS derived TEC were strongly correlated. The parameters hmF2 and foF2 were strongly anti-correlated, as were hmF2 and GPS derived TEC. E region parameters were found not to be well correlated with any other parameters. Attempts to use the IRI-2012 and IRI-2016 models to remove the diurnal cycle showed large discrepancies between ionosonde measurements and IRI time series. Removing the diurnal cycle showed that the observed correlations were mostly the result of solar forcing. One parameter pair, foE and hmE, showed a correlation of 0.5 without the diurnal cycle, which has not yet been explained. foF2 and hmF2 as well as foF2 and GPS derived TEC remained strongly correlated in geomagnetically disturbed conditions, but a range of responses were seen for disturbed correlations between hmF2 and GPS TEC.

This correlation analysis is a powerful tool which is used in this project to demonstrate and validates a new technique of TEC derivation using single frequency signals transmitted between geostationary satellites and ground-based GPS receivers. The correlation analysis showed good agreement over a year both between pairs of GPS receivers and between GPS receivers and ionosonde observations. Correlations between pairs of GPS receivers were consistently high during disturbed conditions, and good agreement was also seen between derived TEC and data from the Multi Instrument Data Analysis System (MIDAS). The analysis suggests that the technique is capable of routinely producing realistic TEC time series in both calm and disturbed geomagnetic conditions. The technique shows potential to become a routine method for real-time TEC derivation.

Contents:

List of Abbreviations:

Abbreviation	Full Name
AGW	Atmospheric Gravity Wave
EGNOS	European Geostationary Overlay System
EOF	Empirical Orthogonal Function
EUV	Extreme Ultra Violet
foE	E region critical frequency for the ordinary wave
foF1	F1 region critical frequency for the ordinary wave
foF2	F2 region critical frequency for the ordinary wave
fxF2	F2 region critical frequency for the extraordinary wave
fxI	Penetration frequency of the ionosphere
GNSS	Global Navigation Satellite System
GPS	Global Positioning System
HF	High Frequency (3-30MHz)
hmE	Height of E region peak electron density
hmF1	Height of F1 region peak electron density
hmF2	Height of F2 region peak electron density
IMF	Interplanetary magnetic field
IRI	International Reference Ionosphere
Kp	Planetary index of level of geomagnetic disturbance
LEO	Low Earth Orbit
MIDAS	Multi Instrument Data Analysis System
NmE	Peak electron density of the E region
NmF1	Peak electron density of the F1 region
NmF2	Peak electron density of the F2 region
SBAS	Satellite-based augmentation system
SSW	Sudden stratospheric warming
TEC	Total Electron Content
TECU	Total Electron Content Unit
TID	Travelling Ionospheric Disturbance
UT	Universal Time
UV	Ultraviolet
WAAS	Wide Area Augmentation System

List of tables

List of Figures

Acknowledgements

Thank you to my supervisors Cathryn Mitchell and David Jackson for their guidance and support, and also to Corwin Wright and Ben Witvliet for teaching me so much and supporting me throughout my research. Thanks also to all my friends at Bath university, past and present, for making the office a great place to be!

I would like to thank the Met Office and the Engineering and Physical Sciences Research Council (EPSRC) funded Industrial Doctorate Centre in Systems for supporting my work. Thanks also to the Lowell Digital Ionogram DataBase (DIDBase) for their ionosonde data and the EUREF Permanent GNSS Network and The International GNSS Service (IGS) for their GPS data. This thesis also makes use of the International Reference Ionosphere (IRI) and the Multi Instrument Data Analysis System (MIDAS).

Special thanks to my friends and family for their love, support, encouragement, Skype calls, care packages and chocolate. Mum, Dad, Squad, Serena, Jemma, Livia, Grace, Talini, THANK YOU! Most of all thank you to Kirsty for repeatedly telling me not to give up, and Becky for refusing to let me.

Chapter 1

Introduction

At altitudes of approximately 60 to 600 km above the Earth's surface there exists an ionised region of the atmosphere, known as the ionosphere. The ionosphere is a plasma composed of positive ions and free electrons created when electrons are split from their neutral atoms by solar radiation, by particle precipitation and by charge exchange processes. The ionosphere can be divided into four regions known as the D (60-90 km), E (90 - 150 km) and F (150 - 500 km) regions, and the topside. The ionosphere from the densest point of the F region upwards is known as the topside.

Beginning in the 1920s the ionosphere began to be studied scientifically with radio waves, radar, rockets and later satellites (Appleton & Barnett 1925; Hargreaves 1992). Variations in the ionosphere can disrupt a range of terrestrial systems including HF radio communications and GNSS positioning, navigation and timing. However, if these variations can be accurately modelled, corrections can be applied and steps can be taken to protect vulnerable systems. Continued studying of the Earth's ionosphere remains important to enhance our understanding of the region. This allows accurate modelling and forecasts of ionospheric fluctuations, which enables the required corrections to be determined.

In this study, pairs of ionospheric parameters are investigated via a cross-correlation analysis. This research will contribute towards a greater understanding of the ionosphere, and unlock a potential new data source, which may lead to improvements in ionospheric products.

1.1 Thesis aims

The overall aims of this thesis are to investigate how well correlated pairs of ionospheric parameters are, both in quiet and geomagnetically disturbed conditions, and to introduce and validate a new technique for total electron content (TEC) derivation. To achieve these aims this thesis will answer the following questions:

1. How well correlated are 24-hour time series of pairs of parameters observed by a single ionosonde?
2. Can ionospheric TEC be determined using a new method involving a geostationary satellite and a single frequency Global Positioning System (GPS) receiver?
3. Does cross-correlation validation imply that the new TEC derivation technique produces consistent, reliable results?

4. How well correlated are time series of TEC derived using this new method with time series of ionosonde parameters?
5. Do the correlation relationships identified hold for geomagnetically disturbed conditions?

These questions are explored in Chapters 4, 5 and 6. Before these, Chapters 2 and 3 explore the background science of the ionosphere, the techniques by which it is observed and surrounding topics.

1.2 Thesis overview

Chapter 2 introduces the ionosphere and the surrounding neutral atmosphere. The processes of ionisation and recombination are explored and the structure of the ionosphere is described. Chapter 2 also discusses variations to the ionosphere and thermosphere with season, latitude and solar activity. The chapter also contains sections exploring atmospheric tides, the Earth's magnetic field, geomagnetic storms, gravity waves and travelling ionospheric disturbances. The potential impacts of ionospheric research are also mentioned.

Chapter 3 gives an overview of the methods by which the ionosphere is observed and measured. This Chapter includes explanations of ionosonde observations and how Global Positioning System (GPS) receivers can be used to measure the ionosphere. The chapter also introduces new ionospheric observation methods that are being explored in the form of geostationary satellites and single-frequency GPS receivers. Ionospheric models are also discussed, with a focus on the International Reference Ionosphere (IRI) and the tomography/assimilative algorithm called the Multi Instrument Data Analysis System (MIDAS).

Chapter 4 begins the investigation into the ionosphere via a cross-correlation analysis of ionospheric parameters observed by both ionosondes and a satellite working with ground-based GPS receivers. A cross-correlation analysis is used to investigate the relationship between the ionosonde parameters: E region critical frequency (foE) and the corresponding height (hmE), F region critical frequency (foF2) and the corresponding height (hmF2), along with GPS derived total electron content (TEC). Cross-correlations are found between pairs of variables for both raw time series and for 24-hour time series with the diurnal cycle removed.

Chapter 5 introduces a new technique for TEC derivation using a geostationary satellite and single frequency GPS receivers, and performs validation of the new technique using the cross-correlation technique introduced in Chapter 4. The issues of clock drift and the consequent implications for the new technique are also discussed in Chapter 5.

Chapter 6 aims to determine whether the cross-correlation relationships identified in Chapters 4 and 5 hold under geomagnetically disturbed conditions. The cross-correlations both between pairs of ionosonde parameters and between ionosonde parameters and GPS derived TEC are re-examined using several geomagnetically disturbed days. After this the strongest storm is taken as a case study for more in-depth analysis. Chapter 7 provides concluding statements for the entire thesis.

Chapter 2

The Ionosphere and Neutral Atmosphere

This chapter introduces the ionosphere and the surrounding neutral atmosphere, to provide the background information needed to understand this thesis. In Section 2.1 an overview of the atmosphere is given. Section 2.2 introduces the ionosphere and explains the processes of ionisation and recombination. Section 2.3 introduces the regions that exist within the ionosphere; the relationship between observations of these regions will be investigated in Chapter 4. Section 2.4 discusses the variations observed in the thermosphere and ionosphere due to factors such as solar activity, time of day, season and planetary latitude. Section 2.4 also includes a section discussing the ionospheric response to geomagnetic storms, which is further investigated in this thesis in Chapter 6. Section 2.5 discusses coupling between the ionised and neutral atmosphere, including sections about atmospheric tides and gravity waves. Section 2.6 explains the Earth's magnetic field and section 2.7 explores the impacts of the ionosphere and thermosphere on daily life, justifying why continued ionospheric research is important. Section 2.8 provides a summary of the chapter.

2.1 Overview of The Atmosphere

The Earth's atmosphere is a gaseous layer surrounding the planet. It is reasonably thin, extending vertically for a distance approximately equal to just 1% of the length of the planet's radius, and is composed predominately of nitrogen (78.08%) and oxygen (20.98%) (Barry & Chorley 2003; Ahrens 2009). There exists no exact upper boundary to the Earth's atmosphere: it reaches hundreds of kilometres above the Earth's surface. The density at high altitudes is much lower than near the ground as 99% of the air molecules are found within 30 km of the Earth's surface (Ahrens 2009). The atmosphere is often divided into four regions with the boundaries defined using either the temperature profile or chemical composition (Ahrens 2009). Here we will define the regions by temperature. Figure 2.1 depicts the atmospheric regions defined by temperature profile.

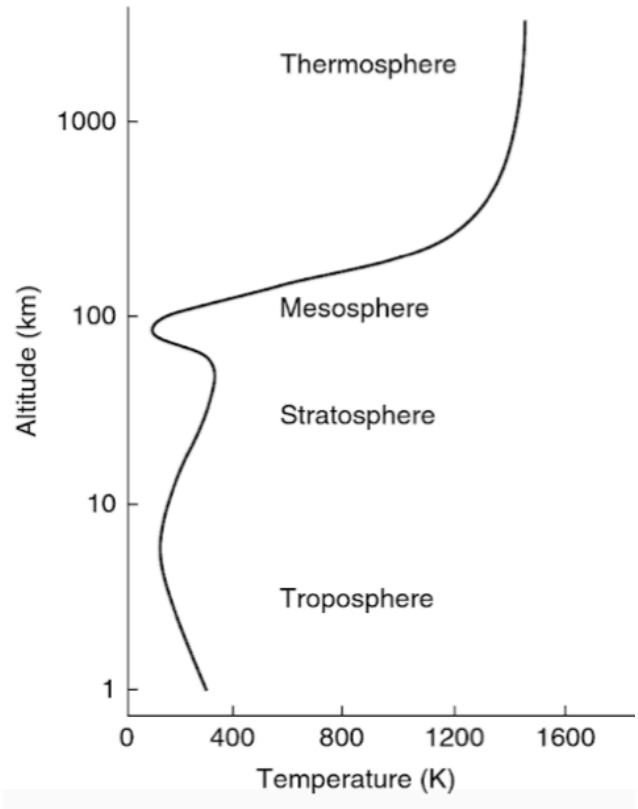

Figure 2.1: Temperature profile through the atmosphere, from Kelley 2009.

2.1.1 The Troposphere

The lowest region of the atmosphere extends from the Earth's surface up to a height of roughly 11 km (with a strong latitude dependence) and is known as the troposphere (Ahrens 2009). It is in this atmospheric region that the majority of meteorological phenomena are found, and the upper boundary is referred to as the tropopause (Barry & Chorley 2003; Ahrens 2009).

2.1.2 The Stratosphere

Above the tropopause extending to an altitude of approximately 50 km (the stratopause) lies the stratosphere, which contains approximately 10% of the atmosphere's mass (Barry & Chorley 2003; Ahrens 2009). It is within this region of the atmosphere that the ozone density reaches a maximum, at an altitude of approximately 22 km (Ahrens 2009; Barry & Chorley 2003). The boundary at the top of the stratosphere is known as the stratopause.

2.1.3 The Mesosphere

The region extending upwards from the stratopause to a height of approximately 90 km is known as the mesosphere, the upper boundary of which is termed the mesopause (Barry & Chorley 2003; Ahrens 2009). The density of this region of the atmosphere is very low, with the entire atmosphere above the stratopause containing only 0.1% of the Earth's total atmosphere (Ahrens 2009).

2.1.4 The Thermosphere

Above the mesopause lies the thermosphere. In this region temperatures increase with altitude as the atmosphere is heated by the absorption of extreme ultraviolet (EUV) energy by oxygen molecules (Ahrens 2009; Barry & Chorley 2003). The upper limit of the thermosphere is defined to be roughly 750 km above the Earth's surface, above which lies the exosphere, where Earth's gravity is no longer sufficiently strong to prevent atoms from escaping into space (Tascione 1994; Hargreaves 1992).

The thermosphere is part of the neutral atmosphere, the physics of which play a key role in determining the dynamics of the ionised region of the Earth's atmosphere, known as the ionosphere (the ionosphere will be discussed in greater detail in Section 2.2.). The distribution and movement of neutral particles are fundamentally important for the process of ionisation and consequently the creation of the ionosphere (Hargreaves 1979; Makela et al. 2012). The density of the thermosphere is very low compared to the lower atmospheric regions, and the distance thermospheric particles move between collisions can be greater than a kilometre (Ahrens 2009). The temperature is maintained in the thermosphere as heat from solar UV and EUV radiation is absorbed by particles and transferred between molecules to lower altitudes (Killeen 1987) Temperatures in this region are consequently influenced by the solar cycle and can be noticeably different over time scales of days and seasons (Barry & Chorley 2003; Ahrens 2009). Another important source of heat in the thermosphere is Joule heating, which results from friction between plasma and neutral particles and is thus dependent upon collisions between ionised and neutral particles (Killeen et al. 1984; Vasyliunas & Song 2005).

As the density of the thermosphere is low, high air temperatures can be reached when only a small quantity of radiation is absorbed (Ahrens 2009), and the thermosphere is the region of the atmosphere where the highest temperatures are attained, frequently above 1000 K (Hargreaves 1992, Kelley 2009). The low thermospheric density allows diffusion to occur, and therefore the distribution of constituents within the thermosphere is determined by their molecular weights (Tascione 1994; Ahrens 2009). The positive temperature gradient within the thermosphere prevents mixing (Hargreaves 1992). At low thermospheric altitudes (below 200 km) the predominate atmospheric constituents are nitrogen and oxygen, the second of which is present in both molecular and atomic states (Barry & Chorley 2003). Above 200 km atomic oxygen is the prevalent atmospheric component, with other low weight elements such as helium and hydrogen also being present (Barry & Chorley 2003; Ahrens 2009). Activity within the thermosphere is highly dependent upon solar activity, which can cause significant changes in the characteristics of the thermosphere over both short and long time periods (Ahrens 2009).

2.2 The Ionosphere

Within the upper mesosphere and thermosphere, starting at altitudes of around 60 km and continuing up into the exosphere, is located a region which is ionised and is known as the ionosphere (Ahrens 2009). Within this region incoming solar energy splits an electron from its neutral parent molecule or atom, causing the parent particle to gain a positive charge and become an ion (Barry & Chorley 2003). This section of the atmosphere enables radio waves to be transmitted around the globe, as the layer reflects the transmitted radio signals (Ahrens 2009). The reflection of radio signals with frequencies from 2 to 30 MHz from the ionosphere allows communication between receivers on different sides of the horizon, which would not be possible otherwise (Davies 1990; Mitchell & Spencer 2003; Zolesi & Cander 2014). It was this reflective property of the ionosphere that lead to its initial discovery (Appleton & Barnett 1925) and the determination of its constituents (Kelley 2009).

The term ionosphere, coined by Watson-Watt (Gardiner 1969) is used to define the electrified gaseous region of a planet's atmosphere, on Earth this extends from roughly 60 to 600 km in altitude (Kivelson & Russell 1995; Kelley 2009; Rishbeth 1988). The Earth's ionosphere is located mostly within the planet's thermosphere, as illustrated in Figure 2.2.

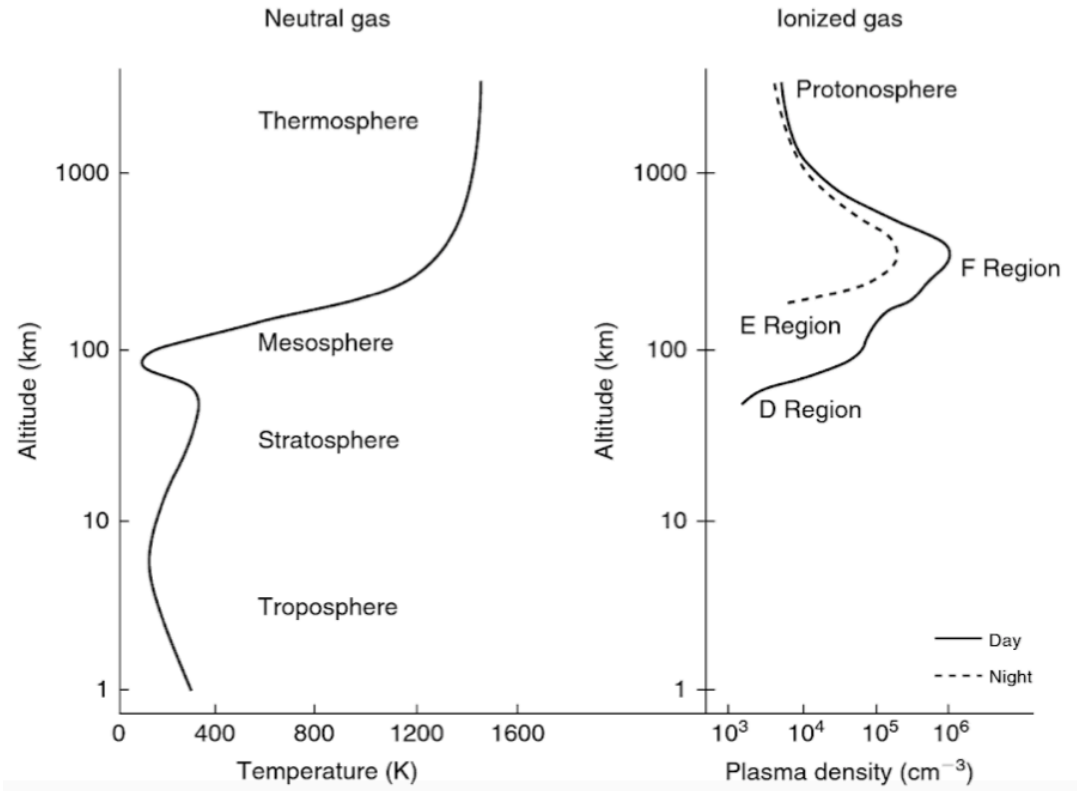

Figure 2.2: Temperature profile and plasma density through the atmosphere, from Kelley 2009.

The ionosphere is created as the neutral constituents of the upper atmosphere are ionised, principally by interactions with solar originating photons (Meyer-Vernet 2007; Kivelson & Russell 1995). Ionisation can also occur due to processes related to particle precipitation involving the planet's magnetic field (Baumjohann & Treumann 2011). As will be described in Section 2.3, there is a clear diurnal cycle in the ionosphere which is predominantly driven by ionisation and recombination processes, so it is important to first briefly describe these processes.

2.2.1 Ionisation

If a photon with sufficient energy collides with an atom of neutral charge the atom can absorb the photon. This can allow an electron to be released from the atom, turning the atom into a positively charged ion (McNamara 1991). This method of creating ions is known as photoionisation and can occur when extreme ultra violet (EUV) light from the sun or Lyman-alpha photons interact with atmospheric particles (McNamara 1991, Kelley 2009). Figure 2.3 illustrates the photoionisation process.

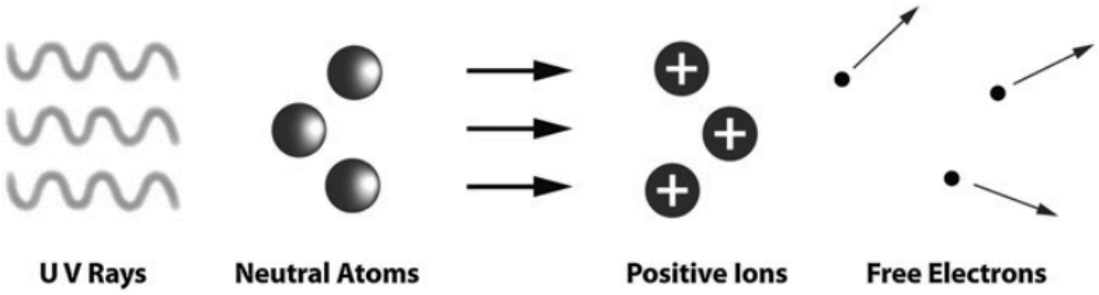

Figure 2.3: Solar UV rays split neutral atoms in the atmosphere into positive ions and free electrons in a process known as photoionisation. Reprinted by permission from Springer: Ionospheric prediction and forecasting, Zolesi & Cander © 2014.

The photoionisation process can also be represented by Equation 2.1, from (Tascione 1994):

$$A + h\nu \rightarrow A^{*} \qquad \textit{Equation 2.1}$$

Here, A represents an atmospheric molecule which absorbs an amount of energy (usually solar), $h\nu$, and thus enters an excited state, A*, which can take the form of an ionised atom. The availability of the photons required for ionisation (the source of $h\nu$ in Equation 2.1) decreases with proximity to the surface as they are absorbed during ionisation. However the availability of neutral constituents increases with proximity to the surface. This results in an ideal ionisation height located in the upper atmosphere, which is where the ionosphere is found (Meyer-

Vernet 2007; Kivelson & Russell 1995). This concept was first described mathematically by Chapman, and a purely mathematical distribution of ionisation with height is known as a Chapman function (Hargreaves 1992; Chapman 1931).

It should be noted that the ionosphere exists in the state of a plasma, i.e. it is an ionised gas with no overall charge (it is neutral) (Tascione 1994). Plasma is created when at least one electron leaves a neutral atom resulting in a positively charged ion being formed, meaning that an equal number of electrons and charged ions are always created (Hargreaves 1979; Kelley 2009). As a result of this, plasma retains a neutral charge overall, with the amount of electrons and ions being almost balanced (Kelley 2009).

2.2.2 Recombination

The reverse of the ionisation process is referred to as recombination. In this process the collision of an electron (which has a negative charge) and an ion (which has a positive charge) results in the creation of an atom (with a neutral charge) (McNamara 1991). The more simple form of recombination is known as radiative recombination, in which a direct interaction between an electron and a positive ion forms an atom with an overall neutral charge (McNamara 1991). Radiative recombination can be expressed by Equation 2.2 from (Tascione 1994):

$$A^+ + e \rightarrow A^* + h\nu \qquad \textit{Equation 2.2}$$

where A^+ is an ion with positive charge, (here the excited molecule A^* has a neutral charge).

Another more complicated, and more efficient, method of recombination is known as dissociative recombination (McNamara 1991). This mechanism has two stages, the first is represented by Equation 2.3.

$$A^+ + X_2 \rightarrow AX^+ + X \qquad \textit{Equation 2.3}$$

Here, a positive ion, A^+, splits a neutral molecule X_2 and combines with one of the atoms to create a temporary, unstable molecule with an overall positive charge, AX^+ (McNamara 1991; Tascione 1994). The second stage of dissociative recombination is represented by Equation 2.4:

$$AX^+ + e \rightarrow A + X \qquad \textit{Equation 2.4}$$

Here, the unstable molecule has combined with an electron allowing the molecule to separate into two atoms with neutral charge, A and X (McNamara 1991; Tascione 1994).

The rate at which dissociative recombination occurs is significantly greater (~100,000x) than that of radiative recombination (Tascione 1994). At lower ionospheric altitudes electrons can also be lost via attachment, when they combine with a neutral atom to form an ion with negative charge (McNamara 1991). The process of attachment can be represented by Equation 2.5:

$$X + e \rightarrow X^{-} \qquad \textit{Equation 2.5}$$

Both forms of recombination and attachment are ubiquitous throughout the ionosphere (McNamara 1991). In all forms of recombination, the speed at which ions and electrons are lost is dependent upon the availability of neutral molecules at the altitude at which the process is occurring (McNamara 1991).

2.2.3 Maintaining the ionosphere

The ionosphere is maintained through continuous ion and electron processes, including their creation, decay, interactions and movement, all of which are regulated by the distribution of neutral particles (Meyer-Vernet 2007; Rishbeth 1998; Hargreaves 1979). Neutral particles are much more abundant in this region of the atmosphere than free electrons, with approximately 1 electron for every 100 neutral particles (Hargreaves 1979). The variation in the ionospheric electron density at any given height can be described using Equation 2.6 (Hargreaves 1992; Rishbeth 1998).

$$\frac{\partial N}{\partial t} = q - L - div(Nv) \qquad \textit{Equation 2.6}$$

In this continuity equation, $\frac{\partial N}{\partial t}$ represents variation in local electron density; q represents the rate at which electrons are created; L the decrease in electron availability due to recombination processes; and $div(Nv)$ represents the decrease in electron availability resulting from the migration of electrons (with v representing the electron mean drift velocity) (Hargreaves 1979; Hargreaves 1992). In simple terms this equation states that change in electron density is equal to production of electrons minus loss and movement of electrons (Hargreaves 1992; Rishbeth 1998).

The ionosphere exists in a state of constant fluctuation. Changes are larger in the vertical dimension, where typical scale values are around tens of km, than in the horizontal dimension, where typical spatial scales range from 100 to 1000 km (Rishbeth 1998). Movement in the vertical dimension is seen to be slower, with average speeds being around 3 ms^{-1}, whilst horizontally directed air motions reach on average speeds of roughly 100 ms^{-1} (Rishbeth 1998). Vertical particle motion in the ionosphere is predominantly dictated by gravity and pressure

gradients, whilst horizontal ionospheric movement is controlled by neutral winds and the surrounding electric field dynamics (Verhulst & Stankov 2017).

2.3 Ionospheric Regions

The ionosphere is created by interactions between neutral particles and photons (Rishbeth 1998). The amount of incoming flux of solar ultraviolet radiation over the solar cycle originating at the Sun and arriving at the Earth can be estimated to take an average value of approximately 3×10^{-3} Wm^{-2} (Meyer-Vernet 2007). This flux is dependent upon the solar cycle, and is seen to be halved and doubled at solar minimum and maximum respectively (Meyer-Vernet 2007).

The ionosphere can be divided into four sections, known as the D, E and F regions and the topside. These regions exist due to the variation in solar absorption and atmospheric composition (which influences recombination) with height through the atmosphere (Tascione 1994). A diagram illustrating the structure of the ionosphere is shown in Figure 2.4.

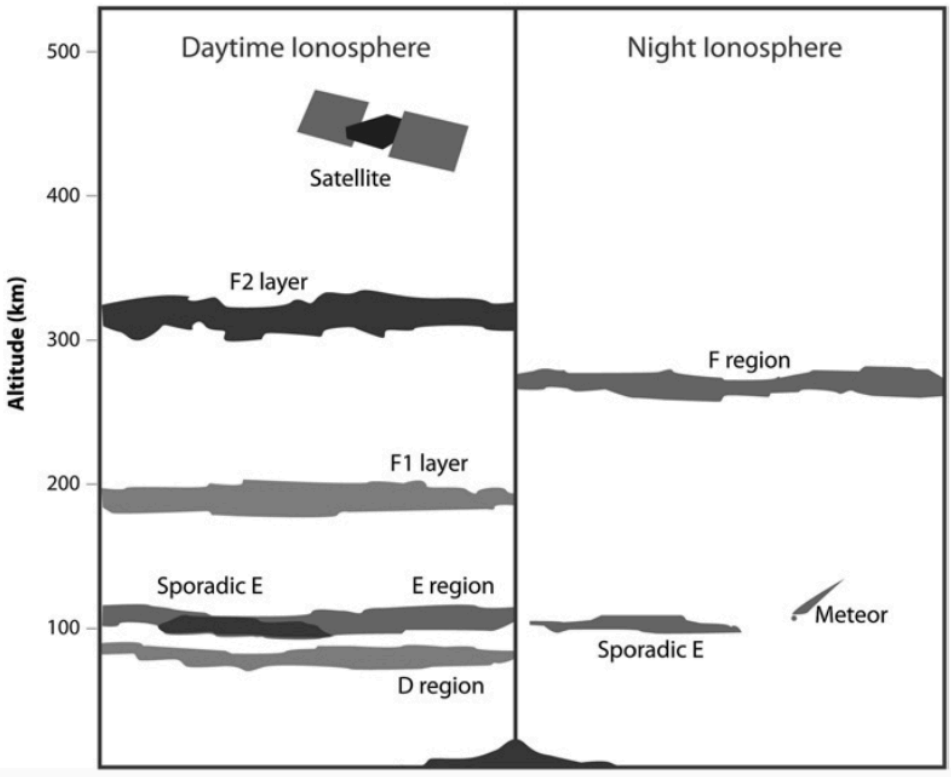

Figure 2.4: Structure of the ionosphere during the day and night. Reprinted by permission from Springer: Ionospheric prediction and forecasting, Zolesi & Cander © 2014.

Sunrise and sunset are the periods of most rapid change in ionisation rates, and consequently plasma density. These parts of the day are the hardest times to accurately represent in models (Verhulst & Stankov 2017). Due to the angle of

incoming solar energy as the sun rises, sunrise occurs at different times at different altitudes, with high altitudes receiving sunlight before lower altitudes. The F region is able to persist overnight (as is shown in Figure 2.4) due to the lower atmospheric density at this height, which reduces the amount of recombination. During the night-time hours the D region of the ionosphere is entirely absent; the E region is significantly less pronounced; and the F1 region becomes indiscernible which allows the formation of a single, less intense F region (Tascione 1994; Hargreaves 1992; Hargreaves 1979).

2.3.1 The D region

The D region is the closest to the surface and extends from altitudes of 60 to 90 km (Rishbeth 1998; Hargreaves 1992). Here, the dominant source of ionisation is Lyman-alpha radiation ionising nitric oxide (NO) (Kelley 2009). X-rays can also ionise NO in the D region, and consequently the region can be strengthened by solar flare activity, which increases x-ray flux (Ratcliffe 1972; Kelley 2009; Tascione 1994; Hayes et al. 2017; Dellinger 1937). Typical D region daytime maximum electron densities are around 1.5×10^{4} cm^{-3} (Tascione 1994). Attachment is the dominant form of electron and ion loss in the D region, as positive and negative ions then interact to return to an overall neutral charge in a process known as mutual neutralisation (Tascione 1994). Recombination is the dominant process during the night-time and consequently during these hours the D region of the ionosphere is entirely absent.

2.3.2 The E region

The E region begins at the top of the D region and extends up to a height of 150 km, with peak electron densities observed at an altitude of roughly 105-110 km (Rishbeth 1998; Hargreaves 1992). Ions are created in the E region as solar EUV ionises predominantly N_2 and O_2 (Ratcliffe 1972; Hargreaves 1979). Equation 2.1 adapted for the E region thus appears in the following forms, from (Tascione 1994):

$$O_2 + h\nu \rightarrow O_2^+ + e \qquad \textit{Equation 2.7}$$

$$N_2 + h\nu \rightarrow N_2^+ + e \qquad \textit{Equation 2.8}$$

By a process known as rapid charge exchange N_2^+ then interacts with O as follows:

$$N_2^+ + O \rightarrow N + NO^+ \qquad \textit{Equation 2.9}$$

Here, O_2^+ and NO^+ are the dominant E region ions, and e represents an electron. Typical noontime maximum electron densities in the E region are in the range of 1.5×10^{5} cm^{-3} (Tascione 1994).

Thin layers of high ionisation occurring seemingly randomly within the E region are known as sporadic-E layers. Sporadic-E (Es) layers originate due to a combination of geomagnetic field activity and local wind shearing, which together can cause a local ionisation compression (Hargreaves 1979; Hargreaves 1992). These layers have been observed to have small spatial extents, sometimes below a kilometre when detected at the planet's mid-latitudes, and are found across a variety of latitudes (Hargreaves 1979; Hargreaves 1992). Dissociative recombination is the dominant method of ion and electron loss in the E regions (Tascione 1994), and during night-time hours the E region is significantly less pronounced.

2.3.3 The F region

The F region begins at the top of the E region (150 km) and extends up to approximately 500 km (Rishbeth 1998; Kelley 2009; Hargreaves 1979). The F region is created as solar EUV ionises atmospheric O and N_2 (Hargreaves 1979; Ratcliffe 1972). In the F region Equation 2.1 takes the form:

$$O + h\nu \rightarrow O^+ + e \qquad \textit{Equation 2.10}$$

with the reactions for N_2 as stated for the E region. O^+ is the dominant F region ion (Tascione 1994).

The F region can be subdivided into two layers, F1 and F2. The F1 layer does not consistently exist, and is more likely to be observed during summer months and when sunspot numbers are low. It is entirely absent during winter months and when sunspot numbers are high (Hargreaves 1992). The solar zenith angle also determines F1 region parameters, and the region is consequently absent at night (Yiğit et al. 2018), allowing the formation of a single night-time F region, as is seen in Figure 2.4. The F1 region has a peak electron density at a height between 160 and 180 km (Hargreaves 1992), and peak midday electron densities of around 2.5×10^5 cm^{-3} (Tascione 1994).

The point of maximum plasma density across the entire ionosphere is normally located within the F2 region, most often at altitudes between 200 and 400 km, and is known as the F2 peak (Kelley 2009; Hargreaves 1979). The plasma density here can reach midday maximum values of 10^6 cm^{-3} (Kelley 2009; Hargreaves 1979). The value of the F2 peak is controlled by the recombination of electrons and ions as together they return to being a particle without charge; in the daytime the creation and decay of ions are in approximate equilibrium for altitudes at and below the F2 peak (Rishbeth 1998; Kelley 2009). Figure 2.5 shows the ionospheric profile with typical densities for each of the ionospheric regions.

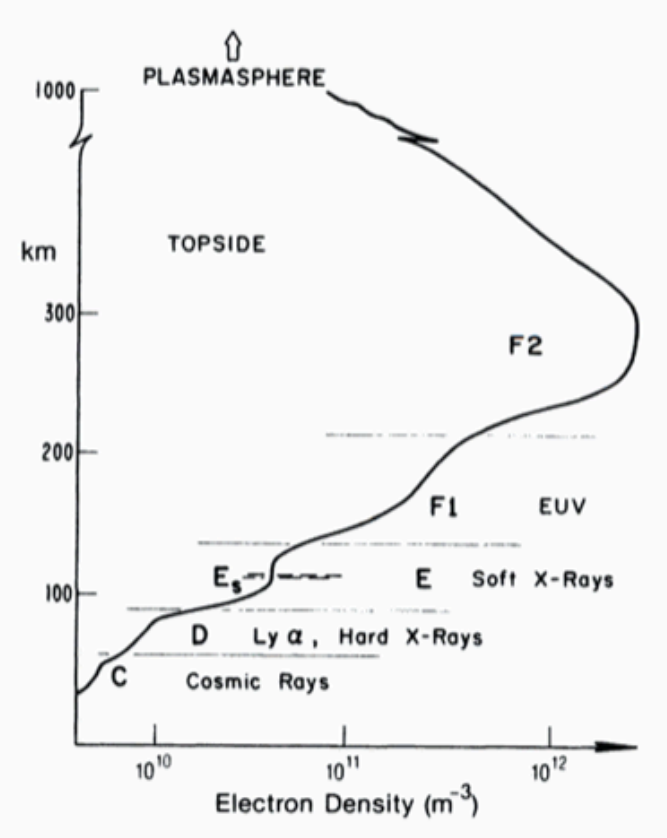

Figure 2.5: Typical profile of ionospheric regions as observed at mid-latitudes, Reproduced with permission from Davies 1990.

The location of the F2 peak can move in the vertical dimension due to either the flow of air containing neutral particles, or due to interactions with electric fields (Rishbeth 1998). Like the E region the dominant method of ion and electron loss in the F region is via dissociative recombination (Tascione 1994).

The term 'topside ionosphere' is used to refer to the ionosphere above the F2 peak, after which the electron density falls with altitude (Hargreaves 1992; Katamzi 2011). Here, the most abundant ion species is O^+, progressing to H^+ above approximately 700 km, and the electron density is determined by diffusion processes (Hargreaves 1979; Hargreaves 1992; Rishbeth 1988)

The diurnal variations in the D, E, and F regions are also seen in total electron content (TEC). Figure 2.6 shows an example time series of TEC over a 24-hour period. The TEC value represents the number of electrons through a column measured between a satellite and the ground. The units of TEC are TECU, where one TECU is equal to 10^{16} electrons m^{-2}.

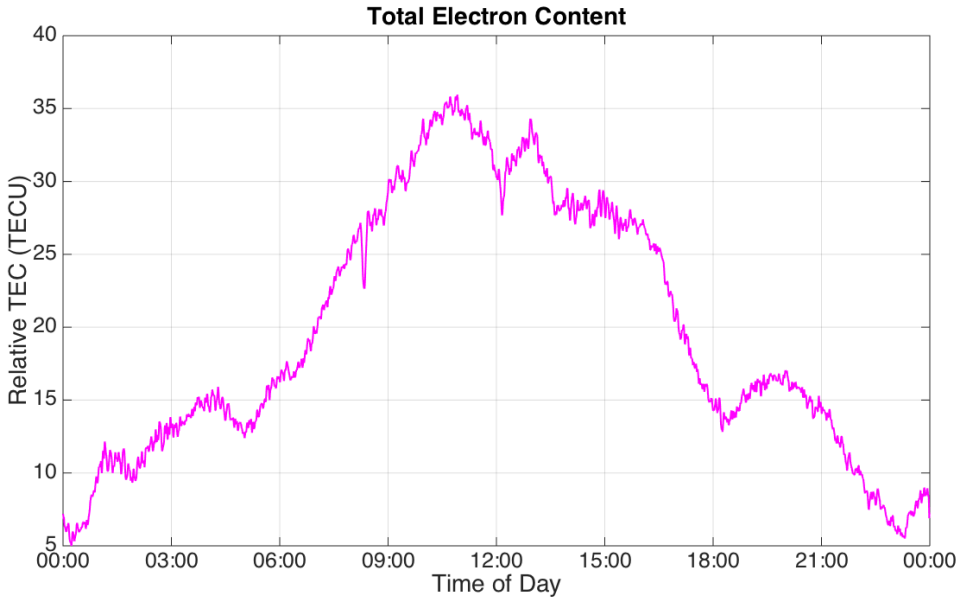

Figure 2.6: 24-hour time series of TEC on 22/11/2015 observed at San Fernando, Spain.

2.4 Variations in thermosphere and ionosphere behaviour

In addition to the diurnal variations described in Section 2.3, the ionosphere also shows considerable latitudinal, seasonal and solar cycle variations. At high latitudes, the solar wind entering the Earth system has a significant impact on the magnetosphere, which geomagnetic field lines link to the local ionosphere (Hargreaves 1992). Additionally, at polar regions the elevation of the sun is lower than is found at lower latitudes, which results in reduced levels of solar driven ionisation (Hargreaves 1979). This process however is counteracted by an increase in ionisation caused by energetic particles originating from the auroras (Hargreaves 1979). Ionospheric activity at the equator is also somewhat counter intuitive. With an overhead sun allowing the highest possible value for ionisation, a planetary maximum for electron density could be reasonably expected (Hargreaves 1979). However in reality, bands of maximum electron density are located on either side of the magnetic equator, from 10 to 20 degrees latitude (Hargreaves 1979; Tascione 1994). This anomaly is caused by a fountain effect where the combined action of magnetic and electric fields, which both have a horizontal alignment at the equator, cause local plasma to move upwards through the atmosphere (Hargreaves 1979). This plasma then interacts with higher altitude magnetic field lines, which, combined with the effects of gravity, direct the plasma along magnetic field lines and away from the equator. This results in a decrease in electron density over the equator and an increase at nearby latitudes on either side (Hargreaves 1979). This process is known as the Equatorial Ionospheric Anomaly (Hargreaves 1979).

As the ionosphere is solar driven it will be affected by any variations in solar activity. Increased solar activity will result in increased EUV arriving at Earth, which will increase the critical frequencies (the highest value of plasma frequency in a given region) observed in each of the ionospheric regions (McNamara 1991; Hargreaves 1979). The ionospheric F region is also observed to be noticeably different in solar minimum and solar maximum (Denton et al. 2009). Oliver et al. 2008 observed F region parameters over a ten-year period to investigate their variations. The study found that the peak F region height varies with solar cycle due predominantly to the expansion of the surrounding thermosphere. The average peak electron density was also observed to vary over both diurnal and seasonal time periods during the solar cycle investigated, which was attributed predominantly to the variation in incoming EUV radiation. Figure 2.7 illustrates how electron densities vary with sunspot number, which acts as an indication of the level of solar activity.

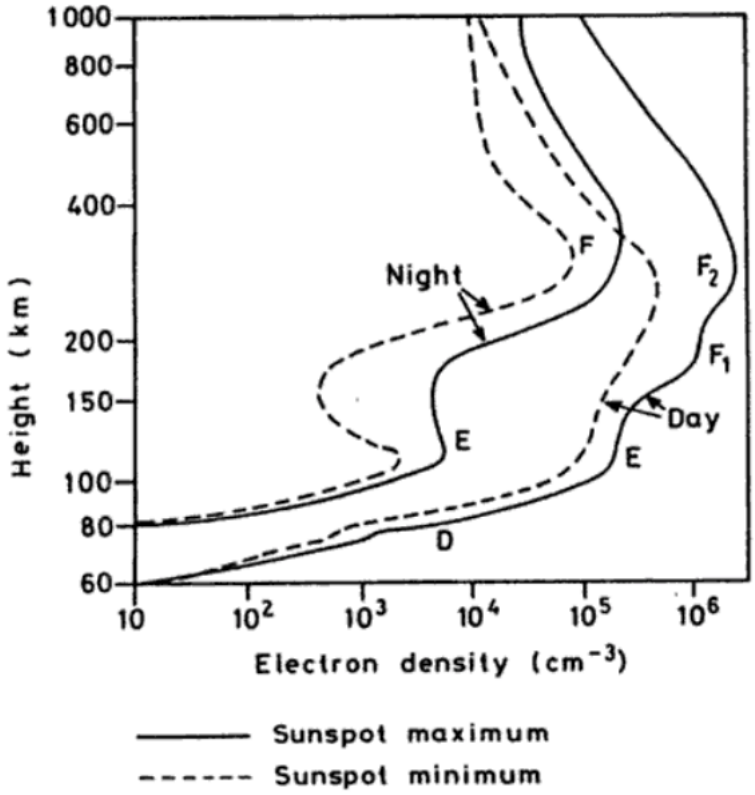

Figure 2.7: Variation in mid-latitude electron densities with sunspot number, from Hargreaves 1992.

The ionosphere also varies on both diurnal and seasonal scales. Electron densities increase towards local noon and decrease afterwards. During local night-time the primary source of ionisation, the sun, is unavailable and consequently recombination dominates and electron density values across the ionosphere decrease (Hargreaves 1992). Peak values of ionospheric electron

density are observed to be lower during local night-time, falling by up to two orders of magnitude (Tascione 1994).

The ionospheric E and F regions also experience seasonal variations. This is caused by the change in solar elevation with season, with low solar elevations causing reduced ionisation due to a reduction in EUV and X-rays (Hargreaves 1979; Verhulst & Stankov 2017). In summer, solar elevation angles are higher than in winter (Katamzi 2011), so a higher rate of ionisation would be expected. In the E region, ionisation levels are observed to be higher in summer than in winter (Tascione 1994), as recently observed by Verhulst & Stankov 2017. The same pattern is observed in the F1 layer, but the opposite scenario is found between seasons in the F2 region, in a process known as the F2 seasonal anomaly (Tascione 1994; Hargreaves 1979). This anomaly occurs as the result of variations in the concentrations of atmospheric constituents between seasons (McNamara 1991). Verhulst & Stankov 2017 found that in the E region the height of peak electron density values also change with season due to the variation in solar elevation angle through the year, however peak height in the F region was found to be unaffected by season. In a study by Oliver et al. 2008 however seasonal variations in height of peak density in the F region (hmF2) were observed, and were attributed to variations in the neutral wind.

2.4.1 The ionosphere and thermosphere during geomagnetic storm conditions

A solar disturbance such as a coronal mass ejection (CME), which can lead to fluctuations in the Earth's magnetic field and influence the ionosphere is referred to as a geomagnetic storm (McNamara 1991). The changes these storms cause to the Earth's magnetic field are often significant (Rishbeth 1988; McNamara 1991). Both the ionospheric structure and the processes within the ionosphere are highly sensitive to geomagnetic activity (Zolesi & Cander 2014), as well as the composition and winds within the thermosphere (Lei et al. 2008).

The energy added to the Earth system during geomagnetic storms alters both the chemistry and dynamics of the thermosphere and consequently the ionosphere. The initial response is observed at high latitudes, but the response then propagates around the globe via wave and particle motions. This results in significant variations to the electron density in the ionosphere, and thus to observed values of both electron density and total electron content (Lei et al. 2008). The energy input can cause lifting of the F2 region and variations in the composition of the neutral atmosphere, which will influence the ionisation and recombination rates (Rishbeth 1988; Hargreaves 1992). Enhancements in geomagnetic conditions can cause a strengthening in the neutral winds (Dandenault & Richards 2015).

Often during a storm the electron density in the F2 layer will experience an increase followed by a decrease and then a recovery period as values return to

background, this spike can last for several days (Rishbeth 1988; Hargreaves 1992; Denton et al. 2009). Geomagnetic storms can cause the amount of atomic oxygen to decrease at the planet's high and mid-latitudes relative to the amount of molecular nitrogen, decreasing the O/N_2 ratio (see section 2.5) (Immel et al. 2001). This change can be as large as a factor of 10 (Immel et al. 2001). Lei et al. (2008) found that that an increase in the ratio of atomic oxygen to molecular nitrogen did not always cause an increase in observed F2 region electron density. Whilst the increased ratio enhanced the loss of ions this was counterbalanced by an increase in electron density due to transport processes.

In the mid-latitude F region positive electron density responses to storms are caused by alterations to neutral winds in the thermosphere, whilst negative responses result from changes to the availability of constituents of the ionosphere, specifically the O/N_2 ratio (Klimenko et al. 2011). The added energy from the storm can cause molecular nitrogen and oxygen to move upwards from lower altitudes into the F region, and lower the concentrations of atomic oxygen in the region (Tascione 1994). Additionally, the introduced molecular nitrogen and oxygen can combine with F region electrons, further reducing the electron density (see Section 2.2, Equation 2.2) (Tascione 1994).

Solar disturbances can also alter the temperature of the neutral atmosphere (Makela et al. 2012; Killeen 1987). Increased levels of particle precipitation can cause the local temperature of the ionosphere to increase, which can enhance recombination and consequently cause lower values of peak electron density to be observed (Denton et al. 2009). Increased temperatures of both the ionosphere and surrounding neutral components results in the expansion of some regions, causing gradients in pressure which result in strong circulations of neutral air (Buonsanto 1999). Thermospheric winds are also enhanced through the exchange of momentum between ions and neutral particles and due to heating of the thermosphere (Zhang & Shepherd 2002).

Geomagnetic storms influence the strength of the local magnetic field, which in turn affects the composition and particle movement within the thermosphere via the process of Joule heating. Joule heating can cause upwards movement of air with high amounts of nitrogen, which can then be transported horizontally (Immel et al. 2001). The amount of Joule heating is increased by high latitude auroral precipitation and convection, both of which are driven by storm-time changes to the interplanetary magnetic field (IMF), as discussed in Chartier et al. 2013.

2.5 Coupling between the ionosphere and neutral atmosphere

The coupling between the thermosphere and ionosphere is an important factor to consider, as the dynamics of the thermosphere strongly influence the structure of

the ionosphere (Tascione 1994; Kelley 2009). The two regions are constantly influenced by processes originating below the thermosphere, such as gravity waves and tides, and are also influenced by fluctuations in solar activity and geomagnetic conditions (Yiğit et al. 2018). Consequently the coupling between the ionosphere and thermosphere is highly variable (Yiğit et al. 2018). Both energy and momentum can be transferred to the ionosphere from the surrounding neutral atmosphere by processes including the movement of air particles and the progression of waves through the atmosphere (Kelley 2009). Thermospheric fluctuations influence a variety of ionospheric characteristics, including ion production and loss, ion distributions and movement, and electron distributions and density (Chartier et al. 2015; Rishbeth 1998; Makela et al. 2012).

The rate of ionisation is controlled by the availability of atomic oxygen (O) and molecular nitrogen (N_2), as shown in Section 2.4. An increase in atomic oxygen increases the availability of atoms to ionise, as can be seen in Equation 2.10. Increased levels of molecular nitrogen however can decrease electron densities, as the N_2 reacts with a positive oxygen ion to recombine, as in Equations 2.3 and 2.4 (Burns et al. 1995). So, using Equation 2.6 the ionisation rate q increases with the availability of O, whilst the loss rate L increases with availability of N2 (Rishbeth 1998). O_2 also contributes towards L but to a lesser extent (Rishbeth 1998). The ratio of O/N_2 therefore is very important for ionisation levels, and is an important mechanism by which the ionosphere and surrounding neutral atmosphere are coupled. Joule heating in the thermosphere can cause air with high nitrogen content to move upwards, and this air can then be moved horizontally affecting the O/N_2 ratio (Burns et al. 1995). The atmospheric composition with altitude is shown in Figure 2.8.

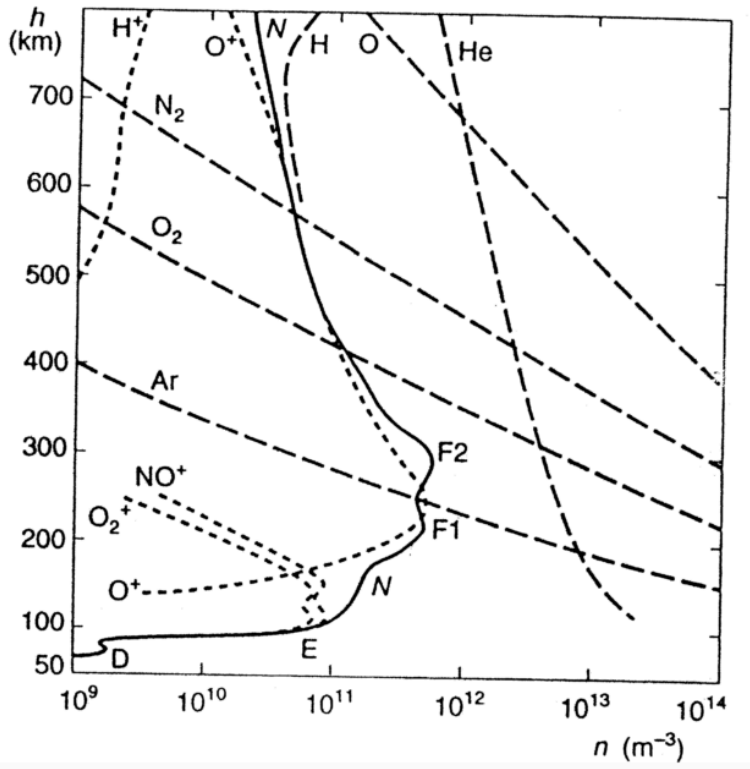

Figure 2.8: Atmospheric composition at ionospheric altitudes, from Dominici 1998.

The thermosphere can also alter the structure of the ionospheric regions via the influence of neutral winds on plasma motions (ion winds) (Chartier et al. 2015; Rishbeth 1998; Tascione 1994). The thermospheric circulation exists as the result of radiative heating arriving from the sun; the interaction between solar wind and the ionosphere; and vertical motions below the thermosphere in the form of tides and waves (Rishbeth 1998). Thermospheric winds can cause the entire ionosphere to be either lifted or lowered depending upon their direction of movement (Hargreaves 1992), with downwards movement of the ionosphere causing recombination rates to increase (due to increased N_2) and thus decreasing the electron density (Kelley 2009). Neutral winds also influence the dynamics of ion movement along magnetic field lines, but are at present poorly understood in their relation to ionospheric parameters such as electron densities (Dandenault & Richards 2015). The physics of travelling ionospheric disturbances (TIDs) is influenced by neutral particle activity (Rishbeth 1998; Luhmann 1983).

In turn, ionospheric activity can cause variations in chemistry and dynamical processes in the thermosphere (Hocke & Schlegel 1996). Particle motions and temperatures in the thermosphere can be influenced by the ionosphere via friction (Chartier et al. 2015). Momentum can be transferred from ions in the ionosphere to molecules in the thermosphere via a process known as ‘ion drag’, where collisions between plasma and neutral air transfer momentum and consequently influence the overall air movement (Kelley 2009; Ratcliffe 1972;

Hargreaves 1992). Neutral and ionised atmospheric activity, and therefore the coupling between the particles, is also influenced by time of day and year, altitude, geomagnetic conditions and geographic latitude (Luhmann 1983).

Understanding the thermosphere is essential for accurate ionospheric modelling. Chartier et al. (2013) showed in a model-based study that forecasts of electron density could be improved by more accurately representing thermospheric initial conditions. Their results showed that incorporating thermospheric data could improve forecasting of plasma density values by 10% if accurate thermospheric information was known, although the improvement was mostly lost after 4 hours. Even if the initial ionospheric conditions were accurate, inaccurate initial thermospheric conditions caused forecast skill to be lost after 30 minutes.

2.5.1 Atmospheric Tides

One of the key mechanisms behind coupling throughout the atmosphere is related to tides (Immel et al. 2006). Atmospheric tides are waves with global scales, and can be created by the release of latent heat on large scales, the sun's gravitational effects, the moon, or atmospheric absorption of radiation from the sun (Hagan & Forbes 2003; Hargreaves 1992; Laštovička 2006). The periods of tides in the ionosphere are typically either 12 or 24 hours, with an 8 hour tide also existing at the planet's high latitudes (Laštovička 2006). Tidal perturbations increase in amplitude as they move upwards through the atmosphere due to the decrease in atmospheric density with height. At thermospheric heights tidal perturbations can have grown to large amplitudes. At E region altitudes tides experience significant dampening due to molecular diffusion, and consequently once the perturbation reaches the ionospheric F region the amplitude remains unchanged (Hargreaves 1979; Kelley 2009; Immel et al. 2006). These oscillations influence the thermospheric winds which in turn affect the ionospheric height and electron density (Hargreaves 1992; Lu et al. 2012). The density of the ionosphere is influenced by atmospheric tides, the strength of which also influence fluctuations in the electric currents within the ionosphere on daily time scales (Immel et al. 2006).

Simulations have shown that tides are important for accurately identifying E region parameters as they are able to influence the E region dynamo electric fields (Immel et al. 2006). In this process the E region ionospheric winds initiated by tides redistribute positive ions perpendicularly to the magnetic field, whilst electrons are forced to move along magnetic field lines. This causes the induction of a current and generates a polarisation electric field (Immel et al. 2006; Forbes et al. 2008; Luhmann 1983).

Tides in the neutral atmosphere have been found to cause variations in pre and post noon electron densities across the E region, and caused ions located at high E region altitudes to move to lower altitudes. Tides have also been linked to the

generation of mid-latitude Es layers (Laštovička 2006). These tidally generated electric fields can then be moved along the planet's magnetic field lines as well as vertically to high altitudes and into the F region (Immel et al. 2006; Forbes et al. 2008).

Simulations have also demonstrated that tides influence the daytime upward movement of plasma within the F region. The E region electric fields determine F region dynamics (Immel et al. 2006). The effect of ionospheric tides on the composition and dynamics within the neutral atmosphere on the peak electron density and height of the peak (NmF2 and hmF2 respectively), have been modelled to cause variations of up to 20% in daytime hours, and of 40% close to the equator in nighttime hours (Laštovička 2006; Fesen 1997). Forbes et al. 1997 used a model to simulate latent heat initiated tidal activity and found that wind variations of 10 to 20 ms^{-1} were observed in the high-altitude mesosphere and the thermosphere, along with temperature changes of 5 - 10 K. These latent heat initiated tides are known to be capable of generating E region winds with strengths of tens of ms^{-1} (Hagan & Forbes 2003; Forbes et al. 2008).

One clear example of how changes in the lower atmosphere can affect the ionosphere is via sudden stratospheric warmings (SSWs), which are sudden changes in temperature and air circulations occurring in winter in the extratropical stratosphere. These warmings have been observed to cause semidiurnal ionospheric variations, observable as semidiurnal tides in observed TEC, as well as variations in the creation of electric fields via the dynamo effect and in the magnitude of the equatorial electrojet (Pedatella & Forbes 2010). It is thought that SSWs influence planetary waves, which in turn impact tidal variations and cause perturbations in the ionosphere (Pedatella & Forbes 2010; Liu et al. 2010). Simulations by Pedatella (Pedatella et al. 2014) indicated that the lunar tide is has a significant influence on electron density in the F region during a SSW.

2.5.2 Atmospheric gravity waves (AGWs) and travelling ionospheric disturbances (TIDs)

Atmospheric gravity waves (AGWs) are travelling disturbances found at all altitudes throughout the atmosphere, but with particular importance for the stratosphere, mesosphere and thermosphere (Ford et al. 2006; Hocke & Schlegel 1996; Tascione 1994). Both thermospheric AGWs and the consequent wave perturbations observed in the ionosphere, known as travelling ionospheric disturbances (TIDs), are of key importance for understanding the dynamics of the atmosphere (Hocke & Schlegel 1996; Hargreaves 1992).

AGWs are a significant contributor to the movement of energy and momentum both horizontally around the globe and upwards towards higher altitudes, and are an important mechanism by which energy and momentum are moved between

atmospheric regions (Makela et al. 2012; Wright et al. 2017; Panasenko et al. 2018). Gravity waves are an important method by which atmospheric regions are coupled, in particular the ionosphere and neutral atmosphere (Wright et al. 2017). GWs also strongly influence the dynamics of atmospheric tides (Hocke & Schlegel 1996;). Figure 2.9 shows a 3-D representation of a gravity wave.

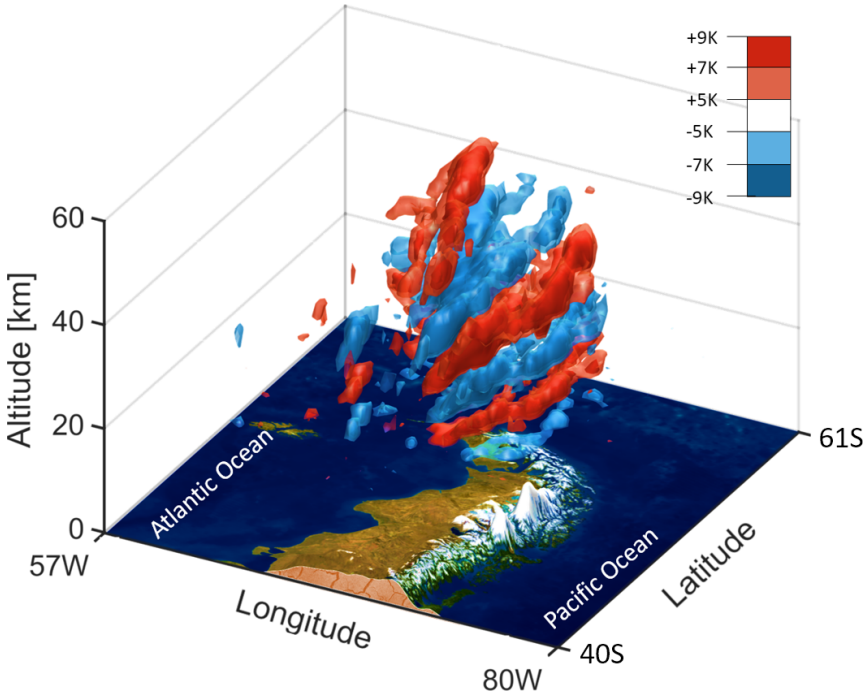

Figure 2.9: 3D plot of atmospheric temperatures showing gravity wave over South America, from Wright et al. 2017.

A study by Vadas & Fritts 2005 demonstrated that GWs generated in the troposphere by convective processes could propagate to thermospheric altitudes. However, gravity waves observed in the thermosphere usually originate locally, and the processes responsible for their creation are theorised to be related to magnetic storms, the planet's auroras and particle precipitation (Ford et al. 2008). It is also possible for medium scale GWs to be created at F region altitudes by convection (Vadas 2007). Immel et al. (2001) observed a large-scale gravity wave initiated by a geomagnetic storm. They also observed that this wave caused variations in hmF2 values of up to 150 km at low latitudes, as well as variations in the ratio of atomic oxygen to molecular nitrogen (Immel et al. 2001).

Gravity waves influence ionospheric dynamics as neutral gas fluctuations cause variations in ionospheric plasma characteristics, including ion velocities, temperatures of electrons and ions, and F region electron density (Hocke & Schlegel 1996; Tascione 1994; Kelley 2009). Gravity waves have been observed in both the ionospheric E and F regions, as well as at lower altitudes within the ionosphere (Laštovička 2006). In the E region gravity waves can contribute

towards the generation of Es layers by causing a strengthening in the neutral winds, and can also cause variations in the altitudes of Es layers (Laštovička 2006).

TIDs exist due to the coupling between the ionosphere and the neutral atmosphere (McNamara 1991). There are known to be several potential sources of TIDs, including geomagnetic and auroral processes as well as gravity waves. Vadas & Fritts 2005 showed that GWs that had propagated to thermospheric altitudes could generate neutral winds, and initiate both large (wavelength >1000 km) and medium (wavelength 100 – 1000 km) scale TIDs (Vadas & Fritts 2005). Evidence of TIDs that were not generated via gravity waves has also been found. It has been shown by Amin et al. 2014 and Amin 2015 that tropospheric lightning can cause variations in TEC and be a source of TID generation. Verhulst et al 2016 theorised that eclipses could also be responsible for the generation of TIDs due to the global movement of the shadow, and this has now been demonstrated by Zhang et al. 2017; Coster et al. 2017 and Mrak et al. 2018. Quiet-time TIDs however are mostly the ionospheric response of a gravity wave (Panasenko et al. 2018).

TIDs are of particular interest in ionospheric studies as they interfere with high frequency (HF) transmissions. TIDs with periods of between 12 and 25 minutes can cause variations in ionospheric electron densities, although these are usually less than 15% (McNamara 1991). Waves moving upwards through the atmosphere can cause noticeable ionospheric variability for time spans on scales of days to weeks (Pedatella & Forbes 2010; Laštovička 2006).

2.6 The Earth's magnetic field and the magnetosphere

The Earth's magnetic field can be thought of as a dipole with an axis tilt compared to the axis of rotation of approximately 11° (Kelley 2009). The alignment of the magnetic field lines varies with planetary latitude. To an observer looking upwards at the equator the field lines would have a horizontal alignment, whilst to an observer at the poles the field lines would appear vertical (Hargreaves 1979). A diagram of the Earth's magnetic field is shown in Figure 2.10.

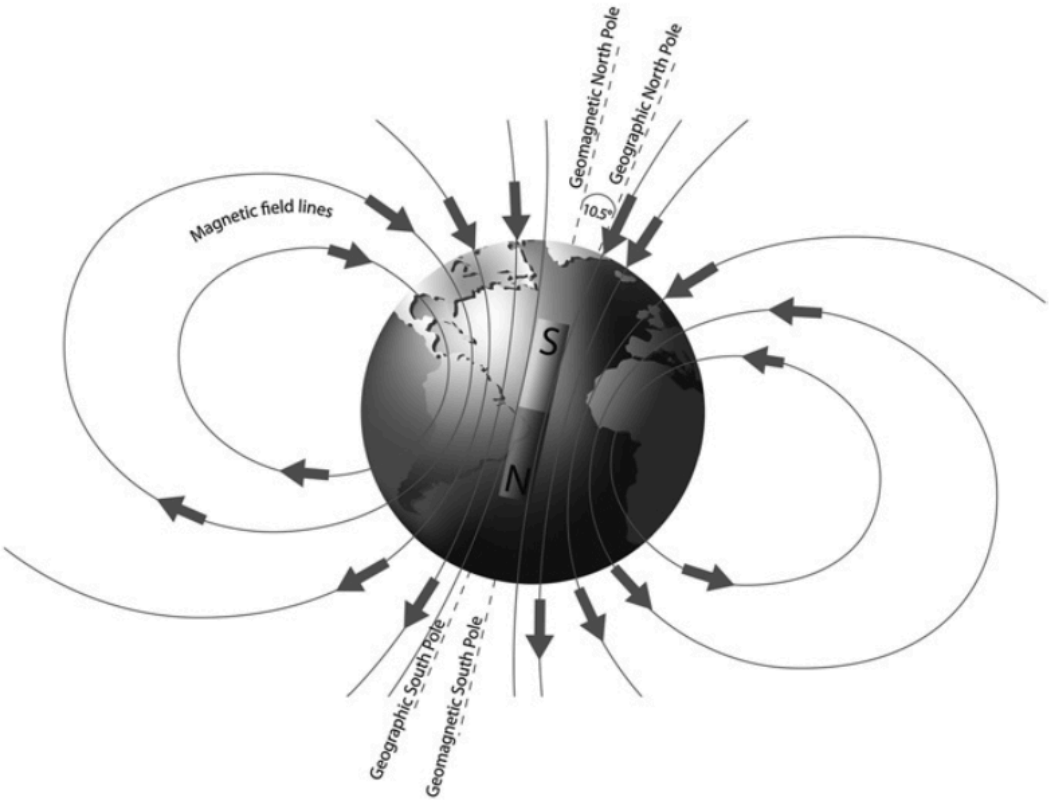

Figure 2.10: The Earth's magnetic field. Reprinted by permission from Springer: Ionospheric prediction and forecasting, Zolesi & Cander © 2014.

Activity and ion motion within the atmosphere is dictated and restricted by the planet's magnetic field, within which the ionosphere is located, as discussed in Bust & Mitchell 2008. The region of the Earth's atmosphere where particle behaviour is dictated by the planet's magnetic field is referred to as the magnetosphere, and energy and momentum from this region can be transferred to the ionosphere (Hargreaves 1992; Kelley 2009). These effects are felt most intensely in the high altitude ionosphere where the magnetic field influences the physics and dynamics of plasma particles and electric currents (Hargreaves 1979).

It is via the Earth's magnetic field that the solar wind interacts with the planet (Hargreaves 1992). The closed magnetic field lines surrounding the planet divert the solar wind along the lines towards the poles. Incoming solar wind can enter the Earth's magnetosphere via the open magnetic field lines at the planet's poles, and the solar wind's energy can enter the ionosphere and high altitude atmosphere (Kelley 2009). Once this energy is inside the Earth's atmosphere it can influence the neutral wind and plasma as well as impacting terrestrial communications (Kelley 2009).

2.7 Ionospheric and thermospheric impacts on daily life

Ionospheric variations have the potential to cause an array of disruptions to our planet and daily lives. Fluctuations in the ionosphere and thermosphere can cause problems for Global Navigation Satellite System (GNSS), for the tracking of satellite orbits and for communication systems, including HF (3-30 MHz) radio communication systems and HF broadcasting (Chartier et al. 2013; Makela et al. 2012; Chartier et al. 2015):

- Every radio signal that passes through the ionosphere will be subject to a group delay and phase advance, the magnitude of which are related proportionally to the total electron content (TEC) along the signal path when estimated to first order (Yin 2004; Hajj et al. 1994). This causes inaccuracies in data relayed by satellites as the size of the experienced delay is unknown (Mitchell & Spencer 2003). This can cause inaccuracies in navigation software (Mitchell & Spencer 2003; Makela et al. 2012), which can cause problems for those requiring high precision. Ionospheric variations can cause deterioration in any signals relayed between orbiting satellites and terrestrial receivers (Bernhardt et al. 1998; Mitchell & Spencer 2003).
- Variations in the ionosphere can also cause signal fading in HF communications, and increased D region absorption can cause radio communications to fail completely (Dellinger 1937). Figure 2.11 illustrates the reflection of radio waves by the ionosphere.

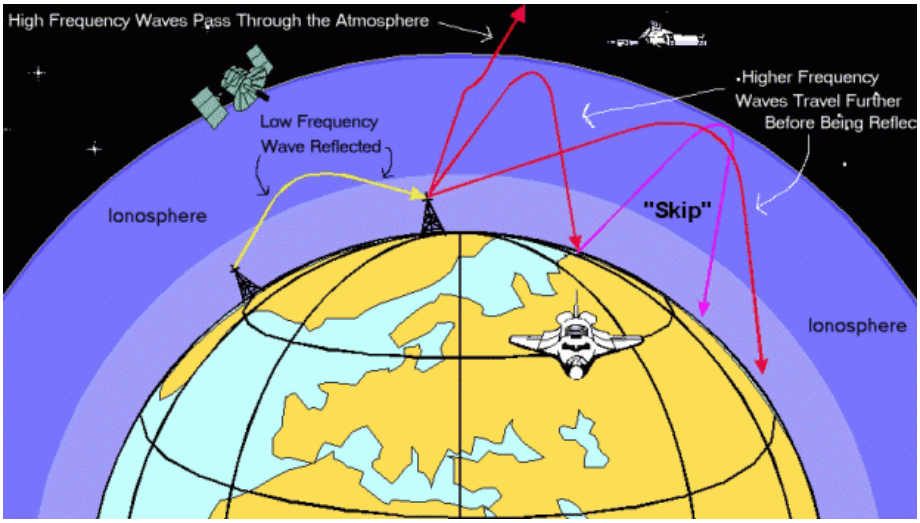

Figure 2.11: The ionosphere influences all signals which pass through it, from https://www.swpc.noaa.gov/phenomena/ionosphere

- Heating in the thermosphere leads to fluctuations in local thermospheric density, which changes the drag experienced by nearby satellites and can cause them to slow down and then drop into a lower orbit (Chartier et al. 2015; Ahrens 2009). If ionospheric fluctuations and delays can be accurately modelled then corrections can be made to the affected systems

to ensure they continue to perform accurately and protective measures can be implemented (McNamara 1991; Mitchell & Spencer 2003).

2.8 Summary

The thermosphere is located from approximately 90 to 750 km above the Earth's surface. Within this region is the ionosphere, a plasma created as solar EUV light splits electrons from neutral atoms and creates positive ions. Within the ionosphere 4 regions can be defined, the D (60 - 90 km), E (90 - 150 km) and F (150 - 500 km) regions and the topside (from the densest point of F region upwards). Ions are neutralised via the process of recombination, which can take the form of attachment (dominant in the D region), dissociative recombination (dominant in the E and F regions) and radiative recombination. The ionosphere is coupled with the surrounding neutral atmosphere, which has the ability to influence ionisation rates, air motions within the regions, electron densities and the overall altitude at which the ionosphere is located. The behaviour of the ionosphere varies on a range of scales, including diurnally, seasonally and with latitude, and also shows unusual activity during geomagnetic storms. Atmospheric gravity waves and associated travelling ionospheric disturbances, can influence both neutral and plasma characteristics. Variations in ionospheric and thermosphere activity can have consequences for terrestrial equipment, satellites and navigation systems.

Chapter 3

Observing the Ionosphere

This Chapter will give an overview of the techniques used to observe and measure the ionosphere. Ionosondes and GPS, which are the data sources used most extensively in this thesis, are discussed in sections 3.1 and 3.2 respectively. Section 3.3 discusses geostationary satellites, and single frequency receivers, both of which are utilised in Chapter 5. Section 3.4 provides a brief discussion of sources of ionospheric observations not used directly in this thesis for the sake of completeness. Section 3.5 explores ionospheric models, with a focus on IRI and MIDAS as both are used in this thesis. Section 3.6 provides a summary of the chapter.

3.1 Ionosondes

3.1.1 How ionosondes are used to observe the ionosphere

An ionosonde is a remote sensing appliance that determines vertical electron density profiles of the atmosphere by electromagnetic sounding (Kelley 2009). Ionosondes consist of a ground based transmitter and receiver. They take measurements by emitting a high frequency (HF) radio wave upwards into the ionosphere and measuring the time it takes to receive the signal reflected back from the ionosphere (Hargreaves 1979). As the frequency of the transmitted wave is increased the amount of refraction experienced decreases, allowing the wave to reach higher altitudes before reflection occurs (Davis 1998). Assuming that the radio signal travels at the speed of light (c) the virtual height (h') of the reflecting layer can be calculated by Equation 3.1

$$h' = \frac{c\,t}{2} \qquad \textit{Equation 3.1}$$

where t is the time delay been signal transmission and detection of the reflection (McNamara 1991). By varying the frequency of the transmitted radio wave between approximately 1 and 20 MHz the change in virtual height with frequency can be determined (Tascione 1994). Ionosondes can consequently produce plots of virtual height against transmitted signal frequency, known as ionograms (McNamara 1991), an example of which is shown in Figure 3.1.

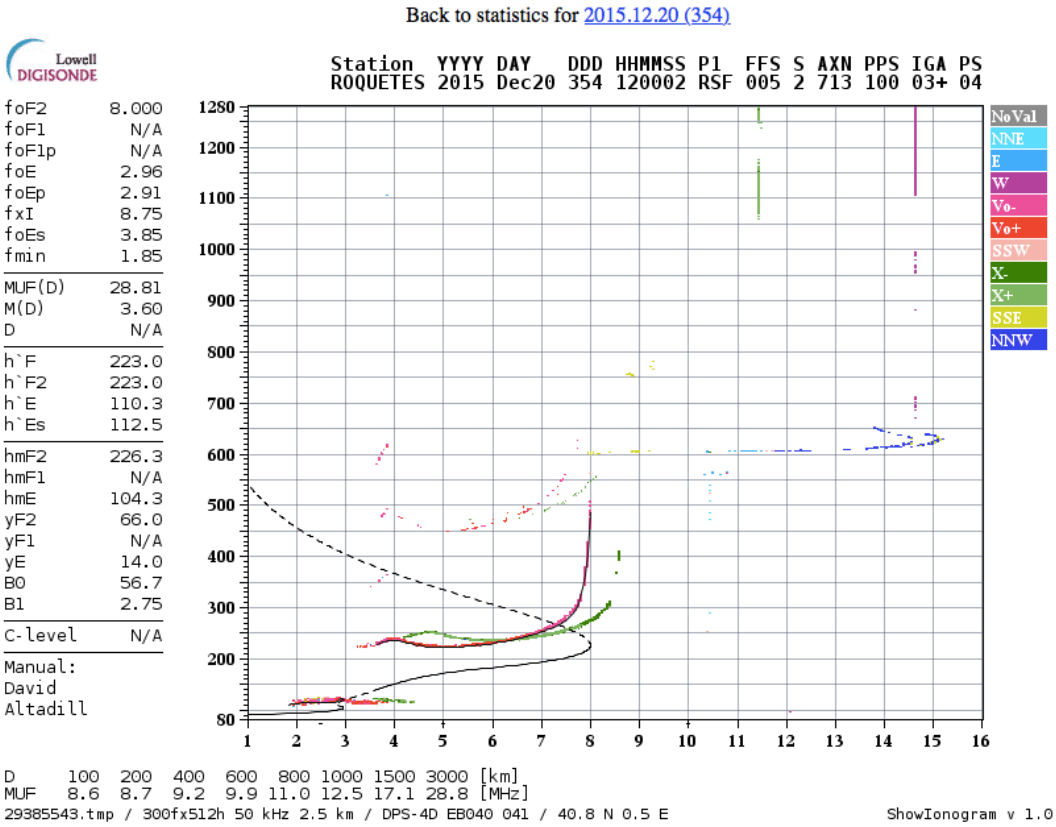

Figure 3.1: Example ionogram from the ionosonde in Roquetes, Spain, showing virtual vertical reflection height verses frequency. From DIDBase http://ulcar.uml.edu/DIDBase/

Ionograms can be analysed to determine several ionospheric characteristics, and the signatures present on the graph can be analysed either manually or automatically by scaling software. Manual scaling is the more accurate technique, however it is more time consuming.

The transmitted ionosonde signal does not actually travel at the speed of light within a vacuum as it slows down in the atmosphere's ionised regions (Tascione 1994). This means that the reflected height deduced by the ionosonde is slightly biased, and the real height is lower, as illustrated by Figure 3.2. A correction is consequently made using the frequencies of the transmitted and received signals, to obtain the true reflection height from the virtual height (Tascione 1994).

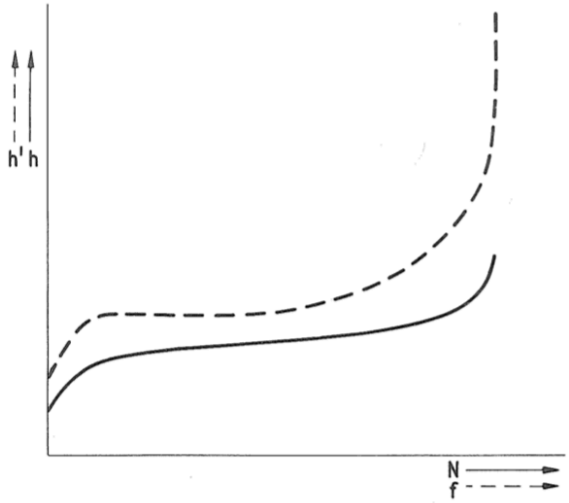

Figure 3.2: Difference between virtual height (dashed line) and true height (solid line), from (Piggott & Rawer 1978).

Radio waves are reflected at the height at which the plasma frequency (f_N) is equal to the frequency of the transmitted radio wave (Hargreaves 1992). The plasma frequency is related to the angular plasma frequency (ω_N) as shown in Equation 3.2.

$$\omega_N = 2\pi f_N \qquad \textit{Equation 3.2}$$

The value of the angular plasma frequency is related to the electron density of the medium by Equation 3.3 (Hargreaves 1992).

$$\omega_N = \left(\frac{N_e e^2}{\epsilon_0 m}\right)^{\frac{1}{2}} \qquad \textit{Equation 3.3}$$

Here, N_e represents the number density of electrons, e is the charge on an electron (1.602×10^{-19} C), ϵ_0 represents the permittivity of free space (8.854×10^{-12} F m^{-1}), and m represents the mass of an electron (9.109×10^{-31} kg) (Hargreaves 1979). Equation 3.3 shows that the square of the angular plasma frequency (ω_N^2) is proportionally related to the corresponding electron density (N_e) of the medium (Hargreaves 1979). Combining Equations 3.2 and 3.3 gives Equation 3.4

$$2\pi f_N = \left(\frac{N_e e^2}{\epsilon_0 m}\right)^{\frac{1}{2}} \qquad \textit{Equation 3.4}$$

Squaring both sides gives Equation 3.5:

$$4\pi^2 {f_N}^2 = \frac{N_e e^2}{\epsilon_0 m} \qquad \textit{Equation 3.5}$$

Rearranging gives Equation 3.6:

$$f_N^{\,2} = \frac{N_e e^2}{4\pi^2 \epsilon_0 m} \qquad \textit{Equation 3.6}$$

Taking the square root gives Equation 3.7:

$$f_N = \frac{(N_e^{\frac{1}{2}})\, e}{2\pi\, (\epsilon_0 m)^{\frac{1}{2}}} \qquad \textit{Equation 3.7}$$

Substituting values into Equation 3.7, an approximation linking the electron plasma frequency and electron density can be found and is shown in Equation 3.10:

$$f_N = \frac{N_e^{\frac{1}{2}} \times 1.602\times10^{-19}}{2\pi\, (8.854\times10^{-12} \times 9.109\times10^{-31})^{\frac{1}{2}}} \qquad \textit{Equation 3.8}$$

$$f_N = -8.9780\, N_e^{\frac{1}{2}} \qquad \textit{Equation 3.9}$$

$$f_N \approx (80.5 \times N_e)^{\frac{1}{2}} \qquad \textit{Equation 3.10}$$

Here, f_N represents the local electron plasma frequency in Hz, and N_e represents the local electron density in m^{-3} (Hargreaves 1992).

The maximum plasma frequency of any ionospheric region is referred to as the critical frequency (Hargreaves 1992). This is the highest frequency at which a wave is reflected by that region. Waves of higher frequency will pass through that region but may still be reflected by a higher region. For example waves with frequencies higher than the critical frequency of the E region may still be reflected in the F region. This is illustrated in Figure 3.1 where the E region reflects ordinary waves up to approximately 3.85 MHz (foEs), after which the F region reflects ordinary waves up to 8 MHz (foF2).

When a radio wave passes into the ionosphere it is split into two waves with complimentary elliptical polarisations, known as the ordinary and extraordinary wave components. These two waves have different velocities, and consequently appear as echoes of different virtual heights on an ionogram (Lowell Digisonde International, 2018). This can be seen in Figure 3.1, where the red lines indicate the ordinary waves and the green lines the extraordinary. The critical frequency of the extraordinary wave (fxF2) is slightly higher than that of the ordinary wave (foF2), so each region of the ionosphere has two critical frequencies.

The highest frequency at which a wave is reflected across the whole ionosphere is referred to as the penetration frequency (Hargreaves 1992). Waves above this frequency will pass through the whole ionosphere and into space. The point of peak electron density is located in the F2 region and as the critical frequency of

the extraordinary wave is higher than that of the ordinary wave, the penetration frequency (fxI) equals the critical frequency of the F2 region for the extraordinary wave, fxF2. Henceforth in this thesis will we deal only with ordinary waves.

Ionosondes are able to investigate the ionosphere up to the height at which the highest electron density occurs, which is associated with the ionospheric penetration frequency. Above this frequency radio waves are no longer reflected and are lost to space, therefore ionosondes cannot see anything beyond this height. This means the topside ionosphere cannot be observed by ground-based ionosondes (Kelley 2009). One technique for investigating the ionospheric topside is to mount an ionosonde onto a satellite to create a topside sounder, which is then able to transmit a signal vertically downwards instead of upwards (Hargreaves 1979). The Canadian Alouette 1 satellite was the first topside sounder, which was launched in 1962 (Hargreaves 1979; Thomas 1963). Although this instrument is again unable to sound past the F2 peak it can provide valuable information regarding the plasma of the topside (Hargreaves 1979). Topside sounders are advantageous as they can make observations in places where ionosonde measurements are sparse, however a disadvantage of topside so lies in the fact that the time and location of observations cannot be chosen (McNamara 1991). As the sounder is mounted upon a satellite, it can only make observations of the ionosphere on or near the nadir to the satellite's path.

3.1.2 Ionosonde parameters

Each region of the ionosphere has its own critical frequency. The critical frequency of the E region for ordinary waves is referred to as foE and the F region critical frequencies for ordinary waves are referred to as foF1 (for the F1 layer) and foF2 (for the F2 layer). The heights at which waves of these frequencies are reflected are found using Equation 3.1, and are referred to as the hmE, hmF1 and hmF2 values.

The critical frequency values of each region (foE, foF1 and foF2) are directly related to the peak electron densities of each region. The peak electron densities of the E, F1 and F2 region are referred to as the NmE, NmF1 and NmF2 values respectively. Adapting Equation 3.10 gives the following simple relationship between electron density and ionosonde radio wave frequency:

$$\mathrm{NmF2} = \frac{\mathrm{foF2}^2}{80.5} \qquad \textit{Equation 3.11}$$

Sporadic-E layers within the ionospheric E region (see Chapter 2 section 2.3.2) appear on an ionogram as a reflection at a higher frequency (foEs) than is typically observed for the E region (foE) (Hargreaves 1992). Sporadic-E layers can entirely obscure the F region from ionosondes and can also cause

scintillations (rapid fluctuations in signal characteristics) in signals passing through the ionosphere (McNamara 1991). Sometimes a 'spread' pattern can be observed on an ionogram, where the reflected signals appear to cover several ranges or frequencies (Kelley 2009). This occurs when plasma bubbles rise upwards through the ionosphere, mix with their surroundings and cause turbulence. This occurrence is mainly observed at low latitudes at F region altitudes and is known as Spread F. This feature is mainly observed at night but has also been observed during the day, and can sometimes be related to F region scintillations, which often occur in clusters with spatial extents of roughly 1000 km (Kelley 2009, Hargreaves 1992).

3.1.3 TEC estimation using ionosondes

Total Electron Content (TEC) is the electron density along a column through the ionosphere. TEC values can be estimated using ionosonde observations. A vertical electron density profile of the ionosphere is created by using values for electron density measured by the ionosonde up to the F2 peak and then approximating the electron density of the topside. Methods for estimating topside values include using a Chapman function (Chapman 1931; Huang & Reinisch 2001), or a model (McKinnell et al. 2007). The TEC value is then calculated as an integral through the entire observed and estimated profile, as represented by Equation 3.12 from (Huang & Reinisch 2001).

$$TEC = \int_0^{hmF2} N_B\,(h)dh + \int_{hmF2}^{\infty} N_T\,(h)dh \qquad \textit{Equation 3.12}$$

Here, N_B and N_T represent the vertical electron density profile of the bottomside (below the F2 peak) and topside (above the F2 peak) of the ionospheric profile respectively; and h represents height (Huang & Reinisch 2001). In simple terms, Equation 3.12 states that the ionosonde derived TEC is equal to the integral through the ionosonde measured electron density profile up to the F2 peak, added to the integral of the approximated electron density profile from the F2 peak up to a given height, for example 1000 km as used in McKinnell et al. 2007.

By combining measurements of ionosonde observed TEC (using a modelled topside) and GPS derived TEC (which will be introduced in the following section) McKinnell et al. 2007 was able to investigate the plasmaspheric contribution to TEC, as well as to demonstrate the viability of using ionosonde data as a validation for GPS measurements.

3.1.4 Ionosonde parameters in this thesis

In Chapter 4 the relationship between time series of ionosonde observations for the parameters foE, hmE, foF2 and hmF2 will be analysed. In Chapter 5 ionosonde TEC will be compared to TEC derived using a new technique involving geostationary satellites and GPS receivers. Chapter 6 will examine

time series of ionosonde observed foE, hmE, foF2 and hmF2 along with GPS derived TEC in geomagnetically disturbed conditions.

3.2 The Global Positioning System (GPS)

The Global Navigation Satellite System (GNSS) incorporates several satellite navigation systems, including the Global Positioning System (GPS), Galileo, the Global Navigation Satellite System (GLONASS), and Beidou. Here we focus on GPS as this is the system most widely used in ionospheric studies and within this project.

3.2.1 GPS derived TEC

The Global Positioning System (GPS) is a constellation of at least 24 satellites, with 8 to 12 satellites visible from any location at any given time (Bust & Mitchell 2008). These satellites are found at altitudes of approximately 20,000 km, have an orbital period of roughly 12 hours and transmit at frequencies of between roughly 1.2 and 1.6 GHz (Bust & Mitchell 2008; Mitchell & Spencer 2003; Kaplan & Hegarty 2006). The idea of using the GPS network to observe the ionosphere was first put forward by Hajj et al. 1994, and first experimental results were gained by Rius et al. 1997. Using GPS signals to measure the ionosphere is advantageous for many reasons: this method is capable of providing continuous observations across the entire planet, has a high sampling rate, and can operate to give near real-time measurements (Mannucci et al. 1999). These features are especially useful when investigating how ionospheric features develop and decay and for analysing storm conditions, with the changes in TEC allowing identification of storm phases (Mannucci et al. 1999; Yin 2004).

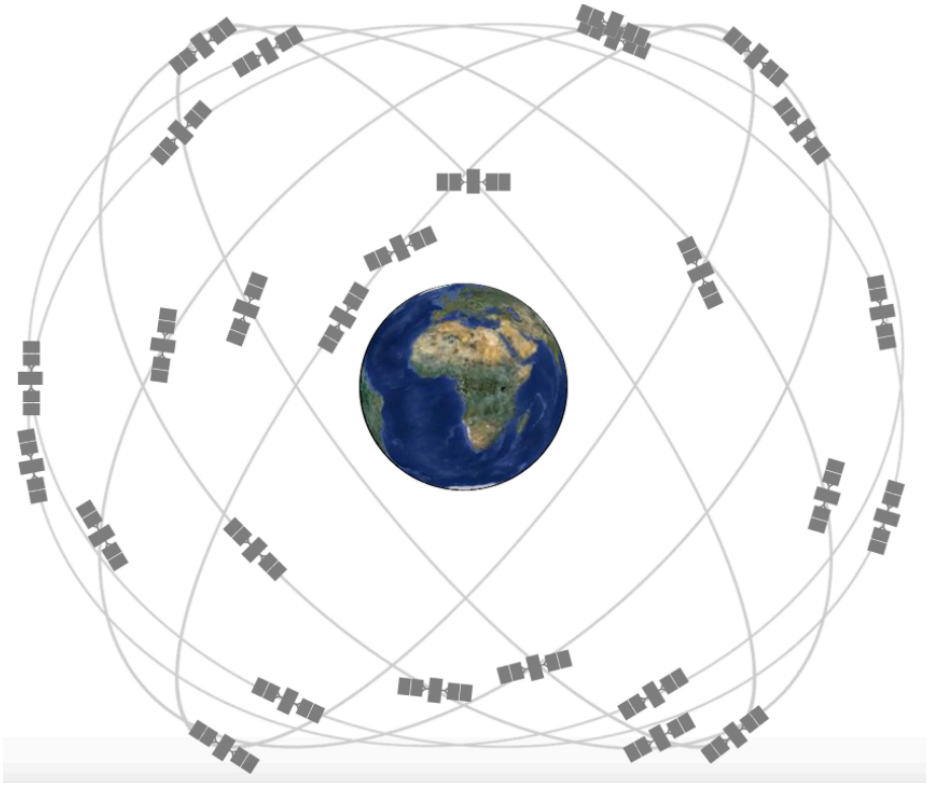

Figure 3.3: The constellation of GPS satellites, from https://www.nasa.gov/directorates/heo/scan/communications/policy/GPS.html

GPS dual-frequency receivers determine the total electron content (TEC) along a signal path by measuring the delay in signal propagation experienced by the signal as it travels from satellite to receiver (Mannucci et al. 1999). Every GPS signal transmitted through the ionosphere will experience both a phase advance and a time delay, the magnitude of which is related to the electron concentration along the signal path (Mitchell & Spencer 2003). Hundreds of dual-frequency receivers are located on the Earth's surface, and some are also on low earth orbit (LEO) satellites, giving a range of potential paths along which TEC can be calculated. As the satellites are rarely directly above the receiver the TEC is calculated along an angled path and is consequently referred to as slant TEC. Clock biases within the receiver mean that distance measurements calculated using range delays are referred to as pseudoranges. GPS TEC measurements are made at two frequencies: f_1 is at 1575.42 MHz and f_2 is at 1227.60 MHz. This allows the detection of range delays of between 3 and 300 TECU, where one TECU is equal to 10^{16} electrons m^{-2} (Mannucci et al. 1999; Kaplan & Hegarty 2006). The following equations, from (Mannucci et al. 1999) are used to derive TEC:

$$P_1 = \rho + \frac{I}{{f_1}^2} + \tau_1^r + \tau_1^s \qquad \textit{Equation 3.13}$$

$$P_2 = \rho + \frac{I}{{f_2}^2} + \tau_2^r + \tau_2^s \qquad \textit{Equation 3.14}$$

$$L_1 = \rho - \frac{I}{{f_1}^2} + \lambda_1 n_1 + \varepsilon_1^r + \varepsilon_1^s \qquad \textit{Equation 3.15}$$

$$L_2 = \rho - \frac{I}{{f_2}^2} + \lambda_2 n_2 + \varepsilon_2^r + \varepsilon_2^s \qquad \textit{Equation 3.16}$$

Here, P_1 and $P_2$are the pseudoranges and L_1 and L_2 are the signal carrier phases in distance units. ρ represents several delay terms and includes non-dispersive delays caused by hardware, errors in the clocks and errors originating in the troposphere. $\lambda_1 n_1$ and $\lambda_2 n_2$ are the cycle ambiguity in the carrier phase, where λ_1 and λ_2 are the carrier wavelengths. ε and τ represent the dispersive hardware delays for the two frequencies, with the subscripts s and r indicating the satellite and receiver between which the signal is being transmitted. The errors on the measured pseudorange and carrier-phase are the same (Kaplan & Hegarty 2006). By subtracting P_1 from P_2, and L_2 from L_1 the ionospheric contribution to the delay, *I,* can be determined, from (Mannucci et al. 1999):

$$P_I \equiv P_2 - P_1 = I\left(\frac{1}{{f_2}^2} - \frac{1}{{f_1}^2}\right) + b_r + b_s \qquad \textit{Equation 3.17}$$

$$L_I \equiv L_1 - L_2 = I\left(\frac{1}{{f_2}^2} - \frac{1}{{f_1}^2}\right) + (\lambda_1 n_1 - \lambda_2 n_2) + b'_r + b'_s \qquad \textit{Equation 3.18}$$

Here the dispersive biases for the satellite and receiver have been grouped into single terms b_r and b_s. Both equations can be rearranged to give values for *I*, indicating the amount of signal day caused by the ionosphere. Values calculated using the pseudoranges, P, are for absolute TEC whilst values calculated using the phase differences, L, are for relative TEC (Katamzi 2011). P measurements contain more noise than L measurements, but L measurements experience biases caused by integer cycle ambiguities (Mannucci et al. 1998). P measurements also experience delays caused by the hardware of both the satellite and receiver, however these can be considered to remain constant over time periods of days, and can be calibrated for during the mapping of TEC (Mannucci et al. 1998).

As TEC is an integrated parameter along the signal path, it can also be expressed by Equation 3.19, from (Mannucci et al. 1999):

$$TEC = \int_{x_r}^{x_s} \rho(\theta, \phi, h) ds \qquad \textit{Equation 3.19}$$

Here, ρ the electron density with x_r and x_s representing the positions of the receiver and the satellite. The GPS network is capable of providing continuous TEC measurements between multiple satellites and a single ground receiver, and by using multiple ground receivers a spatial map of TEC can be produced (Bust & Mitchell 2008). This is accomplished by mapping algorithms, which rearrange Equation 3.19 to find the electron density from TEC values, and combine these values with a background distribution (Mannucci et al. 1999). This background can be provided by models such as the International Reference Ionosphere (IRI)

(Bilitza 1990). Determining electron densities at multiple altitudes using only TEC observations is an under-constrained problem.

The vertical resolution of this technique is poor due to the lack of horizontal signal paths, so some models will only use this technique to estimate a horizontal distribution of electron density (Mannucci et al. 1999; Mitchell & Spencer 2003).

It is possible to detect the existence of Travelling Ionospheric Disturbances (TIDs) in GPS TEC data. Dual-Frequency measurements of the signals from the GPS network have been used to investigate TIDs, e.g. by Tsugawa et al. 2004, Kotake et al. 2011, and Nicolls et al. 2004. These investigations allowed characteristics of TIDs to be identified using GPS TEC measurements as well as TID occurrence rates with time of day and season. It is also possible to estimate foF2 values from TEC measurements, which is beneficial for filling data gaps in the sparse ionosonde observation network. Maltseva & Mozhaeva 2016 used satellite TEC measurements to find approximate values of foF2 by using a modelled value of the ionospheric slab thickness (the ratio between TEC and peak electron density). Adapted terrestrial GPS receivers can also be used to investigate scintillation (Mitchell et al. 2005). Scintillations appear over short time scales so the ionosphere must be sampled very rapidly to observe them, for example at 50 Hz (Smith et al. 2008).

3.2.2 GPS Occultation

To gain a three-dimensional picture of electron density, observations of TEC along a variety of angles (using both vertical and horizontal paths) must be combined (Bernhardt et al. 1998; Meggs & Mitchell 2006). Horizontal paths through the ionosphere can be provided by measuring signals transmitted from the GPS satellite constellation to a receiver located on a satellite in low Earth orbit (LEO) (Bernhardt et al. 1998; Hajj & Romans 1998). This process is known as GPS occultation, and is illustrated by Figure 3.4

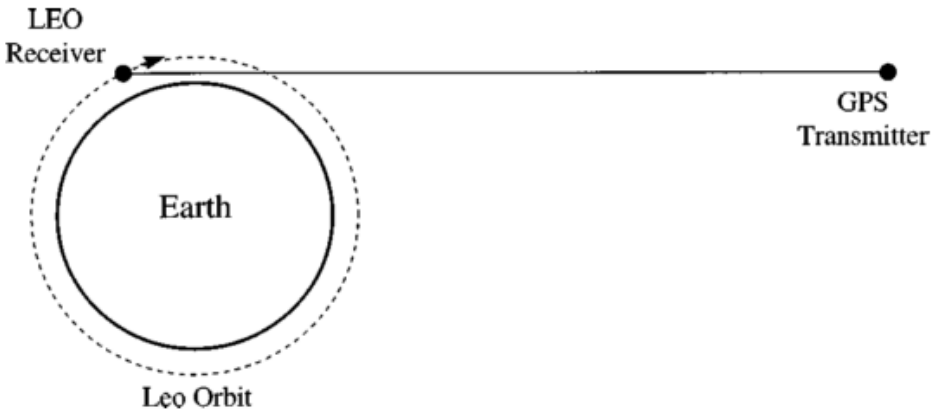

Figure 3.4: GPS occultation between pairs of satellites provides horizontal TEC measurements through the ionosphere, from Bernhardt et al. 1998.

The addition of horizontal observations allows an algebraic technique to solve for electron density values in three-dimensions, as the occulted rays cover large distances horizontally through the ionosphere (Spencer 2014). Examples of current, recent and future GPS occultation satellites include Cosmic (Rocken et al. 2000), CHAMP (Schmidt et al. 2004), GRACE (Beyerle et al. 2005) and COSMIC-2 (Yue et al. 2014).

3.2.3 GPS Tomography

The technique by which multiple TEC measurements taken along signal paths through the atmosphere are used to build two or three-dimensional maps of electron density is referred to as tomography. The technique of tomography was first proposed by Austen et al. 1988. In this process the ionosphere is divided into individual boxes, or volumetric pixels (called voxels), though which multiple line-of-sight observations are made, as illustrated by Figure 3.5. These measurements are of slant TEC, either relative or calibrated, along the signal path and are made using dual frequency GPS receivers (Giday et al. 2016). Algebraic techniques are then used to resolve electron density values for individual voxels in a process somewhat similar to Sudoku.

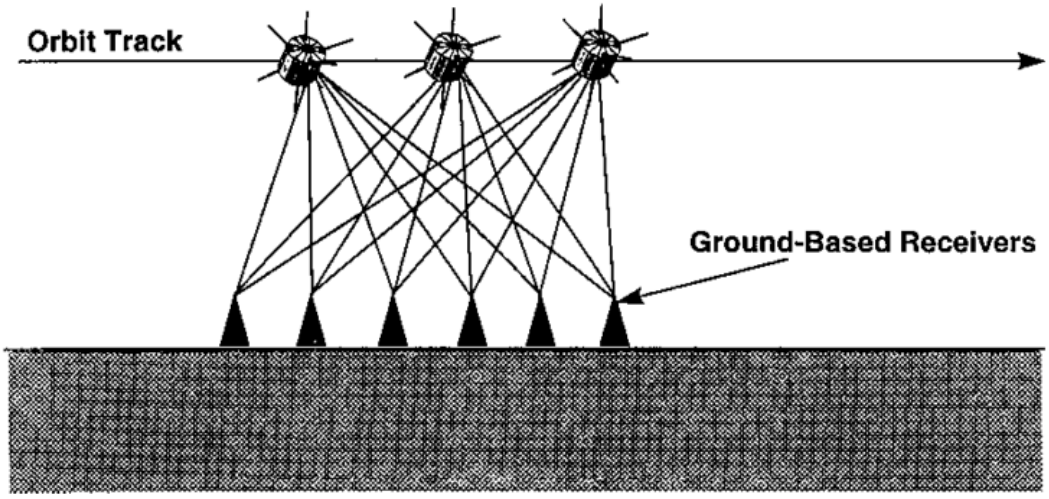

Figure 3.5: Multiple ray paths from satellite to ground receivers intersect each other and allow the determination of electron density via tomography, from Bernhardt et al. 1998.

The process of tomography allows for the generation of three-dimensional maps of TEC on both regional and global scales, as discussed in Giday et al. 2016. Tomography is an advantageous technique to implement as studies have shown that tomographic techniques yield higher quality results across large regions than techniques based solely around GPS derived TEC measurements (Bust et al. 2001). Tomographic techniques accurately represent the integrated vertical TEC

and are useful for showing large scale ionospheric features (Spencer 2014). The quality of tomographic products is dependent on the number of ray paths used, and the regularity (how evenly they are spaced) of the ray paths, as discussed in Giday et al. 2016.

Multiple receivers can be set up in arrays for tomography purposes. For example Tomoscand, a project by the Finnish Meteorological Institute is an array of multiple receivers located across Norway, Sweden, Finland and Estonia on two networks used for 3-D tomography (Vierinen et al. 2014).

3.3 Geostationary satellites

Recently geostationary satellites have also been investigated as a source of TEC measurements. The key advantage of using geostationary satellites is that the exact path (satellite to receiver) through the ionosphere will be fixed and known. This allows for the investigation of continuous changes in TEC along a fixed path over time. Without the use of a geostationary satellite continuous TEC data is only available for between 2 and 6 hours, after which the path is too different for the measurement to be considered to be for the same part of the ionosphere (Kunitsyn et al. 2015).

The process for deriving TEC using geostationary satellites demonstrated by Kunitsyn et al. 2015 is the same as for non-geostationary satellites, by comparing the phase measurements made at the two frequencies of the dual frequency receiver. This gives values of relative slant TEC. The authors noted that a disadvantage to the technique was a higher amount of noise in the data. By observing the movement of scintillation patterns in signals between satellites and receivers ionospheric wind motions can be approximated. Cerruti et al. 2006 used this technique to analyse ionospheric winds using signals from a geostationary satellite along with signals from GPS satellites.

A new method for deriving TEC using signals between geostationary satellites and ground based single-frequency receivers will also be introduced in this thesis in Chapter 5.

3.3.1 Single frequency receivers

Recently studies have started to investigate the possibility of using single frequency receivers from the GPS network. The main advantage of single-frequency receivers is that they are much cheaper than dual frequency receivers (Hein et al. 2016). Hein et al. 2016 used single frequency GPS data to create a TEC distribution map over Japan. The technique assumed a single order, two-dimensional model for TEC, but it was found that the technique was not suitable for all latitudes and did not accurately represent more complicated TEC patterns. A new technique for deriving TEC using single frequency receivers is introduced

in Chapter 5.

3.4 Observational techniques not directly used in this thesis

There exist other techniques of observing both the ionosphere and thermosphere that will not be explored thoroughly in this chapter as the data they provide are not directly used in this thesis. However, they are important observational tools contributing to the field of research so for the sake of completeness they deserve an honourable mention.

3.4.1 Faraday rotation derived TEC using satellites

Prior to the installation of the GPS network TEC was derived from satellite transmissions using the Faraday method. In this method, satellites emit a radio wave at a frequency higher than the surrounding plasma frequency (Ratcliffe 1972). This radio wave is linearly polarised and is divided into two circularly polarised waves of opposite rotation as it propagates through the ionosphere, and then recombines back into a single wave as it leaves the ionosphere (Ratcliffe 1972). As the two circularly polarised waves experience different delays, the recombined wave has a different polarisation, with the amount of rotation of the plane of polarisation indicating the TEC along the signal's path. This technique is advantageous as it is capable of catching rapid ionospheric variations, however the technique requires an estimation of the magnetic field at various ionospheric heights, the inaccuracy of which can cause inaccuracies in the final derived TEC (Hargreaves 1992).

3.4.2 Rockets

Rockets can be used to observe the ionosphere by observing the Doppler shift in waves they transmit. Two waves are transmitted, one at a frequency close to the ionospheric plasma frequency and the other with a distinctly different frequency so that the wave's velocity is close to what it would be if it were travelling through free space. The observed Doppler shifts of these two waves then indicate the speed of the wave within the ionosphere and the speed of the rocket itself. With knowledge of these two velocities the electron density of the region surrounding the rocket can be determined (Ratcliffe 1972).

3.4.3 Incoherent Scatter Radar

Incoherent scatter radars measure the ionosphere by observing the electromagnetic energy scattered backwards by free electrons (Gordon 1958). As the scattering caused by a single electron is known, the amount of scattering observed within a region can directly indicate the election density. Incoherent scatter radars operate at frequencies significantly higher than the penetration frequency of the ionosphere. The power of the reflected waves is very weak, so incoherent scatter radars have transmitters of much higher power than is required for an ionosonde and their receivers can detect much weaker reradiated waves.

They can provide information regarding several ionospheric parameters of the E and F layers, including the characteristics of ions (velocity and temperatures) and electrons (densities and temperatures) (Hocke & Schlegel 1996). They are also capable of observing above and below the point of peak density at the same time, unlike an ionosonde which cannot see anything above the peak (Hargreaves 1992). Electron density can be directly measured by an incoherent radar by three methods: observing the amount of power that is scattered by electrons, observing frequency offsets, or by observing polarisation changes via the aforementioned Faraday technique (Hargreaves 1992). Examples of incoherent scatter radars used in ionospheric studies include the European Incoherent Scatter Scientific Association (EISCAT) radars and the Poker Flat incoherent Scatter Radars.

3.4.5 Riometers

Relative ionospheric opacity meters, or riometers, can be used to investigate the ionospheric D region. Riometers have been used since the 1950s and consist of a highly sensitive radio receiver which is constantly observing the amount of naturally occurring cosmic noise arriving at the planet's surface (Browne et al. 1995). When some of this cosmic noise is absorbed by the ionospheric D region (the densest region of the ionosphere) the amount of noise detected by the receiver is affected. The amount of absorption is directly related to the D region electron density, so by comparing the amount of noise received on a given day to that on a control quiet day, the D region electron density can be determined (Browne et al. 1995).

3.4.6 Radio telescopes

Radio telescopes analyse Faraday rotation to determine variations in the ionosphere, and are also useful for identifying scintillation in the ionosphere. One example of a radio telescope is the Low Frequency Array (LOFAR) (Haarlem et al. 2013; Röttgering 2003). This is an array of antenna stations across Europe that looks through the ionosphere into space. It is necessary for LOFAR to account for the ionosphere impact on the signals received. Consequently LOFAR can observe ionospheric phase fluctuations, and consequently measure the structure of the ionosphere on several spatial scales in order to ensure accuracy to their systems (Röttgering 2003). The system is also capable of investigating the ionosphere by analysing signals received from ground transmitters, so has the capacity to be directly used for ionospheric research.

3.5 Modelling the Ionosphere

Models can be used to give a representation of multiple characteristics of the global ionosphere. There exist several models cable of representing the ionosphere, the thermosphere, or the entire atmosphere. Accurate imaging of the ionosphere is essential for maintaining effective, accurate methods of

communication, observation and navigation (Bust & Mitchell 2008). Ionospheric models perform well on climatological scales (months), but are much less precise at small scale fluctuations over 24-hour periods (Chartier et al. 2013). Model performance is also noticeably less accurate during geomagnetically disturbed conditions (Chartier et al. 2013). There are a range of storm-time processes which have a range of ionospheric consequences, some of which counteract each other, and consequently the ionospheric response is difficult to predict (Chartier et al. 2013). Some of the most well-known ionospheric, and whole atmosphere models are shown in Table 3.1. They are categorised as empirical models if they use a statistical representation of the ionosphere rather than a physics-based representation.

Table 3.1: Ionosphere, thermosphere and whole atmosphere models.

Ionosphere			**Whole Atmosphere**
Empirical Model	**Empirical Data Assimilation**	**Physics**	
International Reference Ionosphere (IRI) (Bilitza 1990)	Multi Instrument Data Analysis System (MIDAS) (Mitchell & Spencer 2003)	A New Ionospheric Model (ANIMo) (Da Dalt et al. 2014)	Whole Atmosphere Model (WAM) (Akmaev et al. 2008)
NeQuick (Nava et al. 2008)	Global Assimilation of Ionospheric Measurements (GAIM) (Schunk et al. 2004)	Thermosphere/Ionosphere general circulation model (TIEGCM) (Richmond et al. 1992)	Whole Atmosphere Community Climate Model (WACCM) (Marsh et al. 2013)
	Electron Density Assimilative Model (EDAM) (Angling 2008)	Coupled Middle Atmosphere – Thermosphere (CMAT2) (Dobbin 2005)	Whole Atmosphere Community Climate Model With Thermosphere and Ionosphere Extension (WACCM-X 2.0) (Liu et al. 2018)
	Ionospheric Data Assimilation Four-Dimensional (Bust et al. 2004)	Coupled Thermosphere-Ionosphere-Plasmasphere-	Ground-to-Topside Model of Atmosphere and Ionosphere for

		Electrodynamics (CTIPe) (Fuller-Rowell et al. 2002)	Aeronomy (GAIA) (Jin et al. 2011)
		Global Ionosphere and Thermosphere Model (GITM) (Ridley et al. 2006)	

Ionospheric and whole atmosphere models are discussed as they are most relevant to the study, however examples of thermospheric models include the Drag Temperature Model (DTM) (Barlier et al. 1978; Bruinsma 2015), and NRLMSISE-00 (Picone 2002), as well as those models in Table 3.1 which include the thermosphere (TIEGCM, CMAT2, CTIPe and GITM). The latter two columns in Table 3.1 couple the ionosphere to the thermosphere, with whole atmosphere models coupling to the entire neutral atmosphere from the Earth's surface. This should lead to an improved representation of the ionosphere, particularly for time periods of 0 to 2 hours. Data from the models IRI and MIDAS are used directly in this thesis, and so these are discussed in more detail in the following sections.

3.5.1 IRI

IRI is an empirical model that makes use of a variety of data sources including ionosondes, incoherent scatter radars and satellites (Bilitza et al. 2011; Bilitza et al. 2017). The model is periodically updated, the latest version being IRI-2016 (Bilitza et al. 2017). IRI is used in a wide variety of ionospheric research, and is recognised as the official standard for the ionosphere (Bilitza et al. 2017). The model makes use of values derived by averaging observations over monthly time periods, and is capable of modelling time series of a range of parameters including electron and ion densities, critical frequencies of the D, E, F1 and F2 regions, their corresponding heights, and TEC (Bilitza et al. 2017). Figure 3.6 shows the 24-hour time series of foF2 as observed by an ionosonde, with the IRI modelled profile for the same date, latitude and longitude.

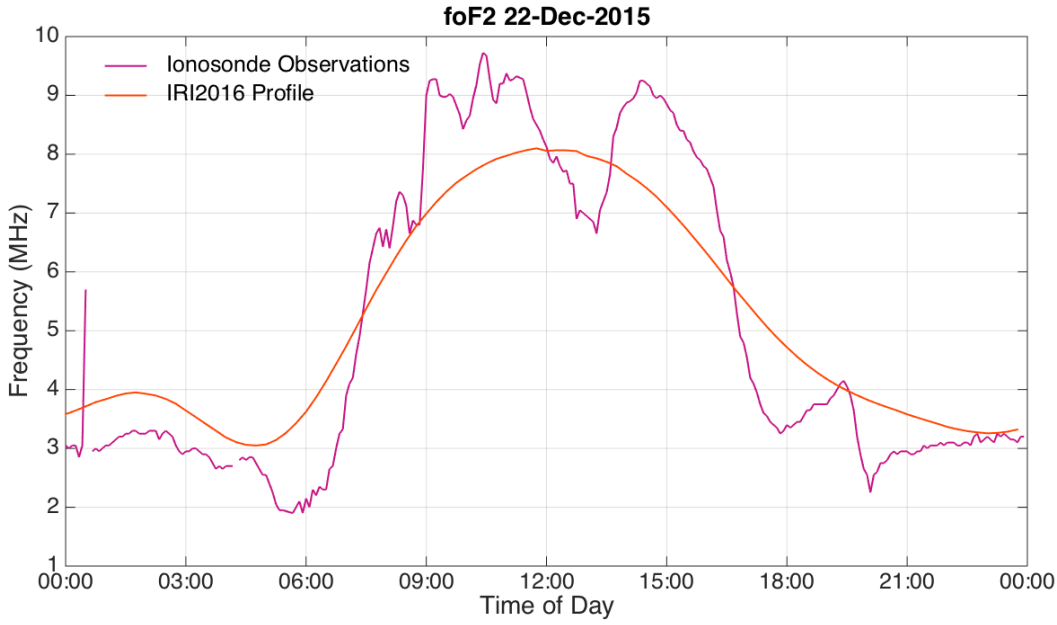

Figure 3.6: foF2 time series measured by the Roquetes ionosonde, and IRI-2016 time series for the same date, latitude and longitude.

A disadvantage of the empirical nature of IRI is that as the model is data based it performs less well in data sparse regions, in particular over the oceans (Bilitza et al. 2011). Additionally as the model is based around monthly averages some small scale features can be smoothed out (Bilitza et al. 2011). However, the advantage of IRI being an empirical model is that a lack of understanding of the underlying ionospheric physics does not prevent the evolution of the model. For example, a four maxima structure has been observed in the variation in electron content and foF2 with longitude (first identified by Immel et al. 2006 and also observed in data from the CHAMP satellite (Lühr et al. 2007)). This feature is thought to be related to atmospheric tides (Bilitza et al. 2011; Lühr et al. 2007) but is not fully understood in terms of processes (Bilitza et al. 2011). It is therefore difficult to accurately represent in a physics model, however it is produced by IRI (Bilitza et al. 2011).

3.5.2 MIDAS

The Multi Instrument Data Analysis System (MIDAS) was first developed by Mitchell and Spencer 2003 (Mitchell & Spencer 2003). MIDAS images the ionosphere via the technique of tomography, building upon the work by Fremouw & Secan 1992. MIDAS uses a computerised tomography technique to combine multiple measurements of TEC made at different angles through the ionosphere to determine the electron density field (Meggs & Mitchell 2006; Da Dalt et al. 2014). These measurements include observations from 80 ground-based GPS receivers from around the world (Spencer 2014). MIDAS maps the tomographically resolved voxel values onto Chapman profiles through which an integration is then performed to give vertical TEC values at any location

(Mitchell & Spencer 2003; Meggs & Mitchell 2006). These TEC values are then used to create a three-dimensional map.

MIDAS images the ionosphere in three spatial and one temporal dimension, using IRI as a background. The model has a spatial resolution of roughly 5 degrees in both latitude and longitude, and a temporal resolution of roughly 20 minutes (Spencer 2014). An example MIDAS image of electron density over the northern hemisphere is shown in Figure 3.7.

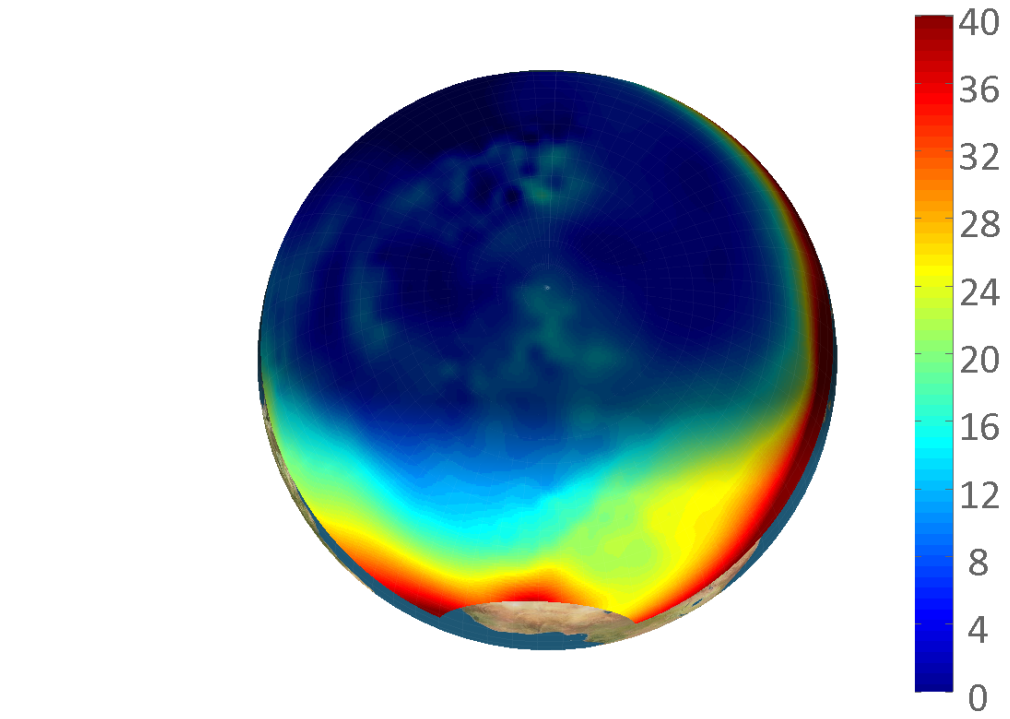

Figure 3.7: Electron density in TECU over the northern hemisphere modelled by MIDAS.

MIDAS is a model frequently used in a variety of ionospheric research, e.g. by Muella et al. 2011 to model the ionosphere around the equator and at low latitudes; Kinrade et al. 2012 to investigate scintillation over Antarctica; Jayawardena et al. 2015 to investigate the topside ionosphere and plasmasphere, Van De Kamp 2013 to investigate the ionosphere over Scandinavia, Spencer 2014 to investigate the drift vortex of plasma, and Bust et al. 2007 to investigate geomagnetic storms. Additionally, there are continual studies into the performance of the model itself and potential future development, e.g. Giday & Katamzi-Joseph 2018; Yin et al. 2017.

3.6 Summary

A variety of techniques and equipment are available to observe and measure the ionosphere. Ionosondes transmit radio waves vertically and then calculate the height of the ionosphere by detecting the wave after it is reflected by the ionosphere. The critical frequency of a region is the highest frequency at which a wave is reflected by an ionospheric region and is directly related to the region's peak electron density. The GPS satellite constellation can be used to provide observations of TEC along signal paths through the ionosphere both from satellite to ground receiver and from GPS satellites to LEO satellites. GPS can provide high resolution, continuous, global TEC observations at near real-time. New research is beginning to investigate the possibility of using geostationary satellites to derive values of TEC. There exist also other techniques for observing the ionosphere and thermosphere, including the Faraday rotation of satellite signals, the Doppler shift of rocket transmissions, riometers and incoherent scatter radar. Models of the ionosphere are useful for the investigation of multiple characteristics of the global ionosphere. IRI is an empirical model that uses monthly averages to create time series of a range of ionospheric profiles, whilst MIDAS uses tomographic techniques and GPS derived TEC to create four dimensional maps of electron density.

Chapter 4

Investigation into correlations between ionospheric parameters measured by ionosondes and GPS receivers

Abstract

The aim for this chapter is to investigate the extent to which ionospheric parameters measured by both ionosondes and the Global Positioning System (GPS) are correlated. The parameters investigated are the ionosonde observed E region critical frequency (foE) and the corresponding height (hmE), F region critical frequency (foF2) and corresponding height (hmF2), and the GPS derived total electron content (TEC). Twenty-four-hour ionosonde time series observations are investigated over the month of December using 6 years of data. GPS TEC, which required more interactive analysis, is investigated over all 12 months of a single year. A correlation analysis was completed between pairs of variables both for the raw observations and for 24-hour time series from which the diurnal cycle had been removed. No significant correlation was seen between pairs of parameters involving the E region except between foE and foF2, where a peak correlation of 0.5 was observed from lags of 0 to -20 minutes. Correlations between foF2 and hmF2 peaked at -0.8 and remained strongly anti correlated for approximately 100 minutes. Attempts to remove the diurnal cycle using IRI-2012 or IRI-2016 revealed large discrepancies between IRI time series and observational data, particularly at sunrise and sunset and when a double diurnal maximum is seen in measurements. Correlations of most parameter pairs without the influence of the diurnal cycle were very low. However, an unusual and as yet unexplained relationship is seen between the perturbations time series of foE and hmE. Correlations between ionosondes in Europe were high for foF2 and hmF2, peaked high for foE but were not sustained for long, and were consistently below 0.4 for hmE. Correlations between GPS derived TEC and ionosonde parameters showed a peak of 0.5 for foE, no significant correlations for hmE, strong correlation (above 0.9) for foF2 and a strong anticorrelation (-0.8) for hmF2.

4.1 Introduction

4.1.1 Chapter aims

In this chapter the following questions are addressed:

1. How well correlated are time series of the E region and F2 region parameters?
2. How well are ionospheric parameters correlated outside of the diurnal cycle?
3. How well are ionospheric parameters correlated between ionosondes at different locations?
4. How well correlated are ionosonde parameters and Global Positioning System (GPS) derived total electron content (TEC)?

The aim of this study is to improve our understanding of the relationship between ionospheric regions and between ionospheric parameters. In this chapter correlation analysis is completed between pairs of parameters from the same ionosonde, between parameters from two different ionosondes, and between an ionosonde and a geostationary GPS receiver. The correlation coefficients were found for each variable pair for which sufficient data were available, for both the raw data time series and the time series for which the diurnal cycle has been removed (perturbation series). It was of interest to include time lag in the correlation analysis, to investigate whether signatures in one data set from one time point correlate with the second data set at a subsequent (or preceding) time.

In Section 4.1.2 the parameters investigated in this chapter are introduced. In Section 4.2 the data sources are discussed along with the new technique for deriving TEC using single frequency GPS receivers. Section 4.3 explains the process for determining the time period over which the correlation analysis was conducted. Section 4.4 explains the process for the correlation analysis. Section 4.5 shows the results of correlating parameters observed by a single ionosonde, and Section 4.6 repeats the correlation process with the diurnal cycle removed from the ionosonde time series. Section 4.7 investigates how ionosonde parameters are correlated between pairs of ionosondes in Europe. Section 4.8 correlates ionosonde parameters with TEC derived from single frequency GPS receivers using a new technique, and Section 4.9 repeats this analysis with the diurnal cycle removed. Section 4.10 provides a discussion on the conclusions of the chapter.

4.1.2 Ionospheric parameters

The region of the ionosphere below the point of maximum electron density (the F2 peak) is divided into layers surrounding local electron density peaks (Ratcliffe 1972). Three of these layers are known as the F2, F1, and E regions and are centred at heights of approximately 250, 170 and 100 km respectively (Ratcliffe 1972; Hargreaves 1979). The ionospheric E region exists between heights of 90 and 150 km (Kelley 2009) and is formed as N_2, O_2 and O are ionised by solar radiation (Ratcliffe 1972; Hargreaves 1979). As the E region is created by solar radiation the electron density increases towards noon and decreases afterwards,

and the entire region is significantly depleted at night (Hargreaves 1992), see Chapter 2 Section 2.3 for more information.

The two E region parameters investigated in this chapter are foE and hmE. The foE value refers to the highest frequency of an emitted radio wave which is reflected by the E region rather than passing through, and is a direct indication of the peak electron density of the E region (Ratcliffe 1972). The hmE value is the altitude at which this peak E region density is located. Example daily time series of these two E region parameters are shown in Figure 4.1. Measurements for night-time hours are absent as the E region is so weak at these times as to be unobservable.

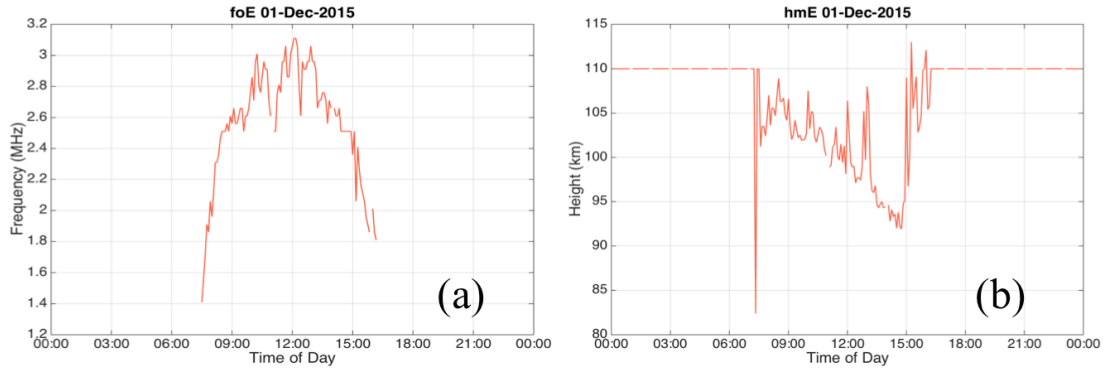

Figure 4.1: Example daily time series of E region ionospheric parameters, (a) foE, (b) hmE as observed by the Roquetes ionosonde.

The F region is the layer of the ionosphere with the highest electron density (Hargreaves 1992). It extends from around 150 to 500 km (Kelley 2009) and is created as solar EUV rays ionise N_2 and O (Hargreaves 1979; Ratcliffe 1972). Unlike the E region, the F region persists through the night due to diffusive transport processes. The presence of neutral winds in the F region are also important, as they are capable of influencing and altering the height of the entire layer (Hargreaves 1992).

The part of the F2 region with the highest electron density is referred to as the F2 peak, and the height at which this peak is located is referred to as the hmF2 value. The highest frequency at which a radio wave is reflected by the ionosphere rather than penetrating through (which occurs at the F2 peak) is referred to as the foF2 value. This value is directly related to the peak electron density of the F2 region, which is known as the NmF2 value. Examples of typical 24-hour time series of foF2 and hmF2, which are the two F region parameters investigated in this chapter, are shown Figure 4.2. Note the strong anticorrelation between foF2 and hmF2, and the large changes in foF2 and hmF2 seen at dawn and dusk.

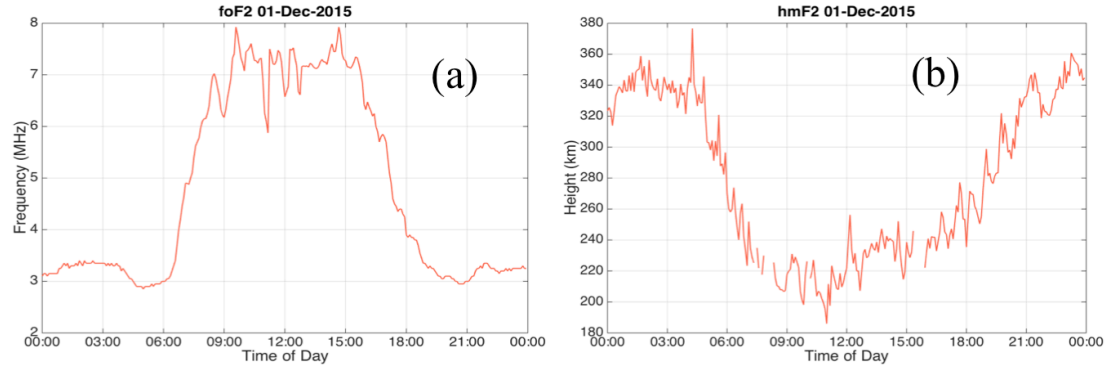

Figure 4.2: Typical 24-hour time series of F region ionospheric parameters, (a) foF2, (b) hmF2 as observed by the Roquetes Ionosonde.

The time of day at which peak values of F2 are reached changes with season, with the peak located close to midday in the winter months, and further from local noon (in either direction) in the summer months for mid-latitudes (Hargreaves 1992). The peak values of electron density (and therefore frequency) are also observed to be lower in summer than in winter (Hargreaves 1992).

Another ionospheric parameter investigated in this chapter is the total electron content (TEC). This is defined as the integrated total electron density along a column through the atmosphere. Here we use the slant TEC, which is the electron density along a line-of-sight satellite to ground receiver signal path (Bust & Mitchell 2008; Kelley 2009). Henceforth these slant TEC measurements will be referred to as 'TEC'. TEC is dominated by the F region electron density so the TEC time series is similar to the foF2 time series shown in Figure 4.2 panel (a). An example of a typical 24-hour TEC profile is shown in Figure 4.3.

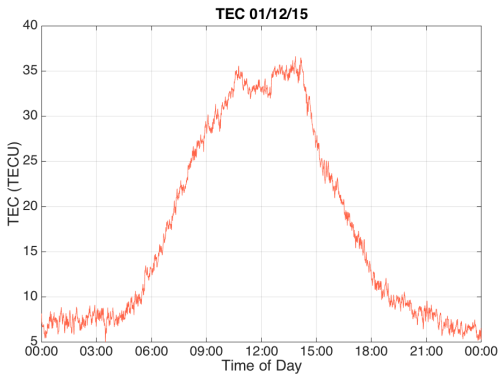

Figure 4.3: Typical 24-hour time series of total electron content (TEC) derived at a single frequency ground based receiver.

4.1.3 Correlation analysis studies

This Chapter makes use of cross-correlation analysis to investigate the relationship between ionosonde parameters. The correlation technique used is a

Pearson linear correlation. Correlation analysis has been used in ionospheric investigations before. Elemo (2015) found correlation analysis between ionosonde stations was useful for separating signatures in foF2 data caused by geomagnetic storms from signatures caused by earthquakes. This allowed the determination of seismological-ionospheric coupling in the data. The technique was useful as it allowed the identification of variations present in both data sets as well as variations only present in one location (Elemo 2015). A correlation analysis was also used in ionosphere earthquake studies by Pulinets et al. 2004, who correlated TEC observations from pairs of GPS stations to detect seismic signatures. High correlations (above 0.9) were often seen but were interrupted in the days before the occurrence of a strong seismic shock.

Liu et al. 2001 showed that the parameters NmF2 and vertical TEC are highly correlated, peaking at a value of 0.953. Kouris et al. 2004 used correlation analysis to investigate the relationship between TEC and $(\mathrm{foF2})^2$ and found that the two parameters were highly correlated, usually attaining a value above 0.8 when monthly and daily medians were correlated. The lowest correlations were observed during the summer. This relationship was true for both GPS and Faraday rotation derived TEC. Correlations between TEC and $(\mathrm{foF2})^2$ on different days of the month and year were lower, suggesting hourly variations in the parameters were more similar than those on different days. McKinnell et al. 2007 analysed 4 months data and found a high correlation between NmF2 and ionosonde TEC, and also between ionosonde TEC and GPS derived TEC.

McNamara & Wilkinson 2009 found the correlation coefficients between the deviations in foF2 from the monthly median, using data from pairs of ionosondes. A decrease in solar activity was observed to result in a decrease in correlations, which was linked to the solar wind influence on neutral winds and composition. The study also found that correlation fell roughly linearly with the distance between stations. Linear spatial correlations have also been used by Shim et al. 2008, to investigate correlations between variations in TEC observations over 30 day periods, between pairs of receivers.

Ionospheric correlation analysis usually focuses on investigating foF2 or TEC. This chapter is more comprehensive and includes correlation analysis of E region parameters, investigations linking the E and F regions, investigations between hmF2 and foF2, a study of time-lagged correlations and a correlation study with the diurnal cycle removed.

4.2 Data sources and GPS technique

Ionosondes observe the ionosphere by transmitting radio waves upwards at a range of frequencies and measuring the reflected signal (Tascione 1994). Ionosondes are normally angled vertically and are particularly useful for

ionospheric investigations as they are capable of observing multiple layers of the ionosphere and of detecting travelling ionospheric disturbances (TIDs) (Kelley 2009).

The ionosonde observed parameters investigated in this chapter are foE, hmE, foF2, and hmF2. Analysis using parameters from the F1 region of the ionosphere (F1 region critical frequency (foF1) and corresponding height (hmF1)) was attempted but was not possible as sufficient data were not available.

Correlation analysis is also performed on relative TEC values derived using receivers that are part of the Global Positioning System (GPS) network. These values are acquired using a new technique that allows the approximation of relative TEC between a geostationary satellite and a single frequency ground-based receiver, fully described in Chapter 6. Here, we refer to relative TEC as an uncalibrated approximation of absolute TEC. By subtracting the phase range of the satellite to receiver signal from the pseudorange of the same signal, and assuming that the hardware biases for all equipment remain constant, a relationship can be found such that:

$$I_{rel} = \frac{(P_1 - L_1) \times f_1^2}{2 \times 40.3} \qquad \textit{Equation 1}$$

Here, I_{rel} refers to the relative TEC, P_1 is the GPS pseudorange (in m), L_1 is the signal carrier phase range (in m) and f_1 is the frequency of the signal (in Hz). The constant 40.3 has units of m^3s^{-2} and is described in Chapter 6. Here the measurements of relative TEC are in TECU, with 1 TECU being equivalent to 10^6 electrons m^{-2} (Mannucci et al. 1998). As the positions of both the receiver and satellite are fixed and known, positioning errors do not need to be considered. This is a new technique which will be fully derived and validated for the first time in Chapter 6 with the use of correlation analysis. Preliminary validation using correlation statistics has shown that this technique creates geophysically-plausible 24-hour time series of relative TEC over a year, which show good agreement between receivers and with independent ionosonde observations. In this chapter the TEC derived via this technique are treated purely as a data source.

We identify the ionosondes used in this chapter with the codes EB040 (Roquetes, Spain 40.80°N, 0.50°E), AT138 (Athens 38.00°N, 23.50°E), EA036 (El Arenosillo 37.10°N, 6.70°W) and RL052 (Chilton 51.50°N, 0.60°W). Data from a single-frequency GPS receiver are also used in this chapter. The receiver is located at Huegelheim (47.50°N, 7.35°E) and we will refer to it as Hueg. The geostationary satellite used in the TEC approximations is the Sirius-5 (SES-5) satellite, also known as PRN 136, and is located at 5° East. The path from satellite to ground receiver is slanted which means that the TEC is derived along

a slanted path. Locations of all ionosondes and the single frequency GPS receiver used in this chapter are shown in Figure 4.4.

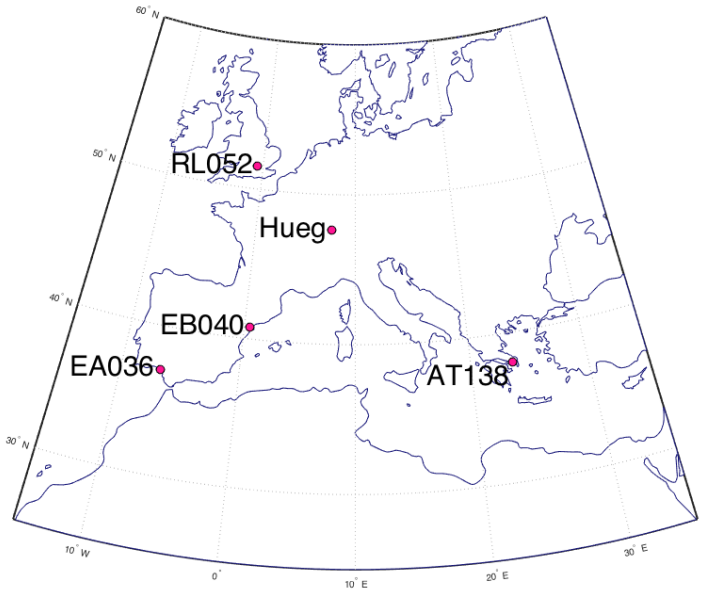

Figure 4.4: Locations of Ionosondes (RL052, EB040, EA036 and AT138) and single frequency GPS receiver (Hueg).

4.3 Selecting lag length

To investigate how well correlated a time series of one parameter was with another parameter in times preceding and following time zero (where both time series are overlayed), a time limit over which to investigate must be selected. The length of time investigated on either side of time zero will be referred to as the 'lag length'. A sensible lag length also needs to be determined. A travelling ionospheric disturbance (TID) moves through the ionosphere with a speed in the order of hundreds of metres per second and a period of between 30 minutes and 3 hours (Hocke 1995). This suggests that to track ionospheric features both at a single station and between stations up to 1000 km apart, assuming a velocity of 100 ms^{-1}, a lag length of up to three hours would be sensible (note that, at 100 ms^{-1} a signal will take nearly three hours to travel 1000 km).

It was decided that the lag length would also be roughly equal to the time taken for a parameter to no longer be correlated with itself with lost correlation defined as a value below of 0.5. The first step was to correlate a daily parameter time series with itself over a variety of lags. During this process two identical daily time series were overlaid, and the correlation calculated, giving a value of one. Next, one time series was fixed and the other was shifted multiple times by time steps equivalent to the data resolution of the selected ionosonde (5 minutes for EB040). Any data gaps were filled via a linear interpolation. The shifting process

is illustrated in Figure 4.5 panel (a), with the original time series in black and shifted time series of 5, 10 and 20 shifts (i.e. 25, 50 and 100 minutes) in pink. Each shift moves the profile by 5 minutes. A correlation value was calculated between the black time series and each pink time series (to give three values in this example), for shifts extending up to 300 minutes (60 shifts).

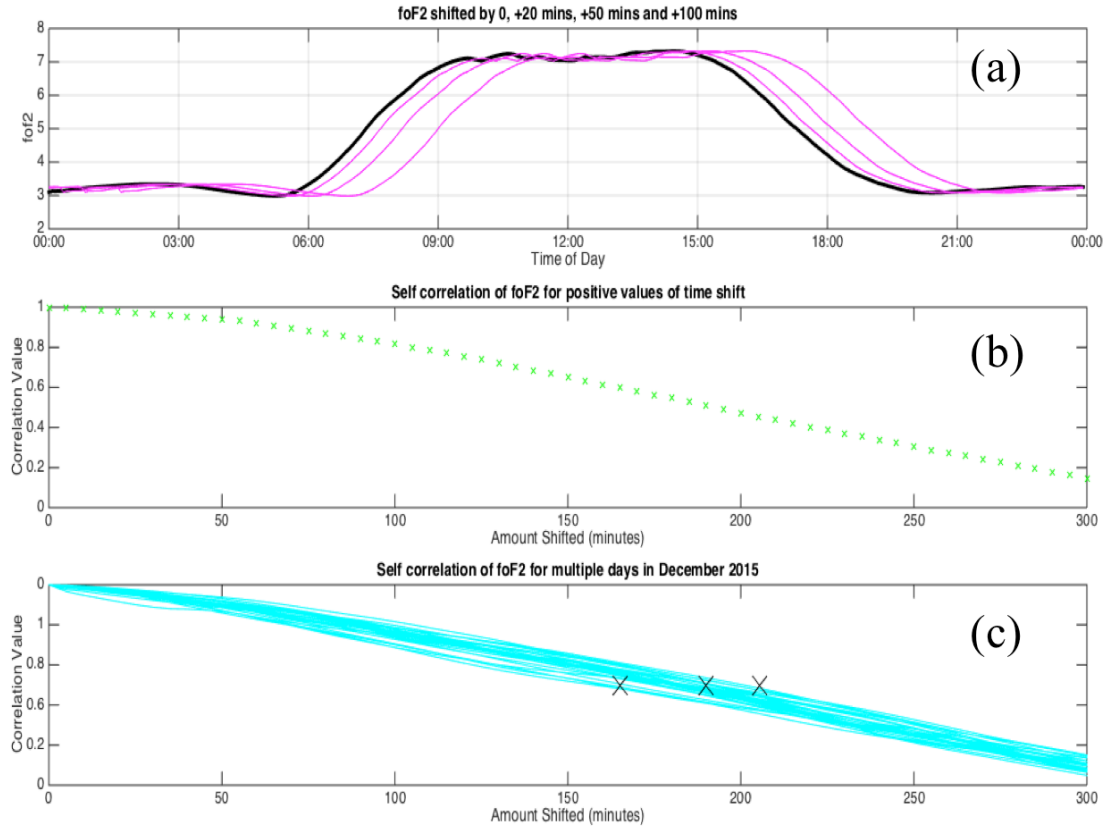

Figure 4.5: Demonstration of lag length determination process showing (a) how profiles are shifted, (b) fall in parameter autocorrelation value with time, and (c) fall in parameter autocorrelation over a month with crosses representing the 5th percentile, median and 95th percentile for a correlation of 0.5.

The next step was to determine the number of shifts required to attain each correlation value. Panel (b) in Figure 4.5 shows the correlation value attained between the original and each shifted time series. It can be seen that it takes roughly 180 minutes (or 36 shifts) to fall from a correlation of 1 to a correlation of 0.5. This process was repeated for each day in 2015 to create multiple daily correlation sequences like the example in panel (b). Panel (c) of Figure 4.5 shows daily time series from a month's data. For each correlation value on the y-axis, the median x-axis value was found across all 365 days, along with the 5th and 95th percentiles. For example, the 5th percentile, median and 95th percentile for a correlation of 0.5 using data from days in December 2015 are depicted by crosses in Figure 4.5 panel (c).

The statistics from this analysis over a year (2015) for all days where at least 85% of data were available are shown in Figure 4.6, using foF2 data from the EB040 ionosonde. In this plot the y-axis shows correlation thresholds and the x-axis shows time in minutes. The red line depicts the median values for 2015, and the red shaded region shows the range between the 5th and 95th percentiles. In this plot it can be seen that the median time taken for the correlation to fall to 0.5 over the year was approximately 200 minutes.

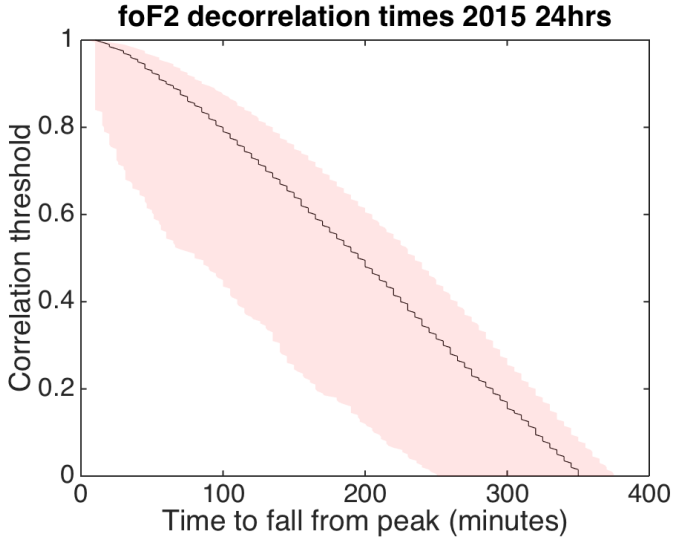

Figure 4.6: Autocorrelation statistics for foF2 observations at the EB040 ionosonde over the year 2015, with red line representing median values and red shaded region showing the range between the 5th and 95th percentiles.

This process was repeated for all four ionosonde parameters using 6 years of data, 2010-2015, with the statistics from each year calculated separately to give 6 separate data sets. The six datasets for each parameter were overlaid to give 6 years of data on a single plot for each parameter. Each black line depicts the median values for a year, and each red patch indicates the 5th and 95th percentiles for a single year. These plots are shown in Figure 4.7. F region parameters (foF2 and hmF2) were analysed over 24 hours, whereas parameters for the E region (foE and hmE) were analysed between the hours of 9am and 3pm as the E region largely dissipates outside sunshine hours.

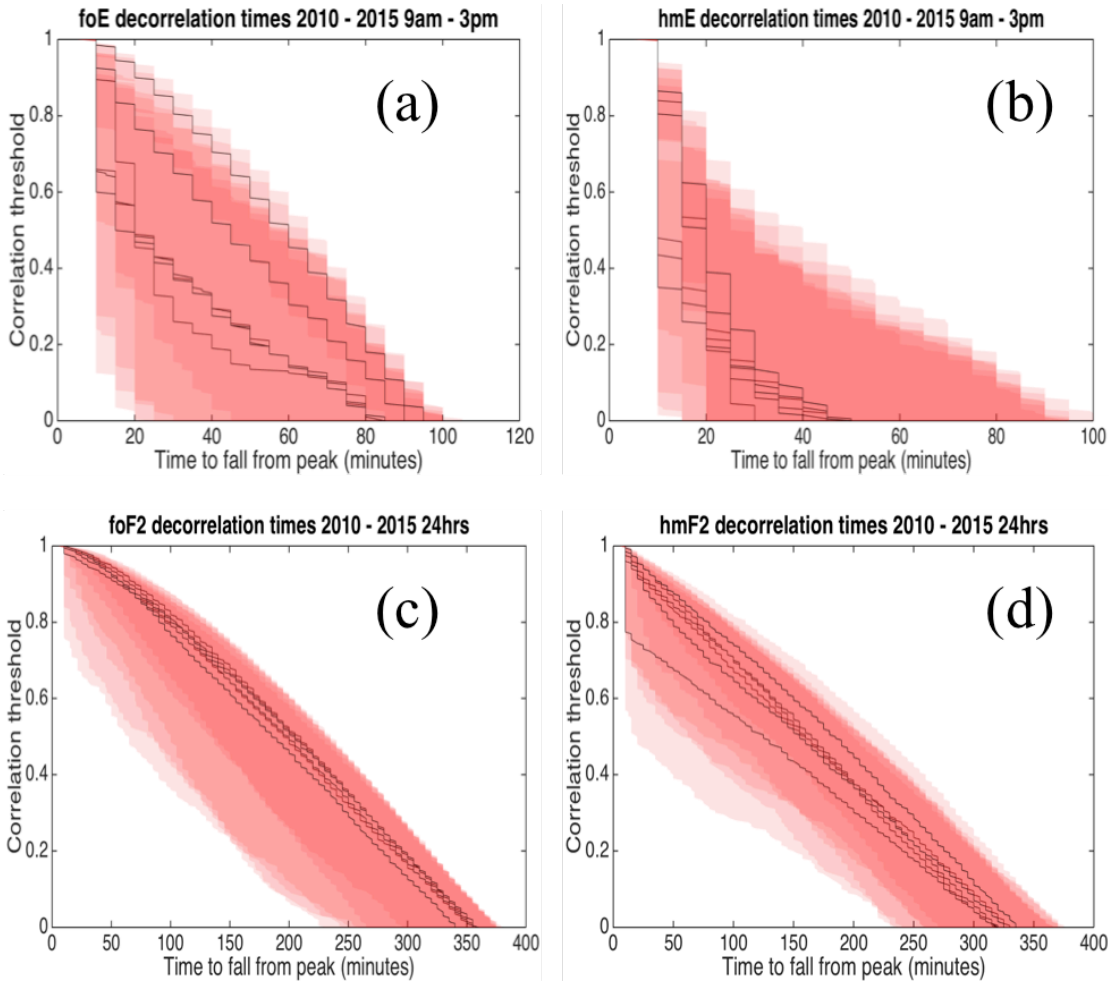

Figure 4.7: Autocorrelations for ionosonde parameters observed at the EB040 ionosonde (a) foE (b) hmE (c) foF2 (d) hmF2, with black lines representing median values for each year.

From these figures we see that the E region parameters lose correlation noticeably faster than the F2 region parameters. The analysis suggests that correlation analysis after 180 minutes was not sensible as the autocorrelation of both E region parameters had fallen to zero and hmF2 had fallen below 0.5 by this time. 180 minutes was thus applied as the lag limit for subsequent correlation analysis.

4.4 Cross-correlation analysis

To assess the agreement between pairs of different ionosonde parameters a cross-correlation analysis was completed. The results are displayed as coloured contour plots. In these plots the colour of each pixel represents the percentage of data at the lag value displayed on the x-axis that had the correlation value displayed on the y-axis. To accomplish this, the daily time series of both variables were overlaid and the correlation between them was calculated. After this, the second parameter time series was held stationary and the entire time series of the first

variable was shifted by 5-minute time steps until the decorrelation lag limit (180 minutes) was reached. A new correlation value was calculated between the fixed and shifted time series after each shift. The correlation analysis required the two data sets to have an equal number of data points so where there were gaps in the data a linear interpolation was performed. Where parameters with sampling rates below 5 minutes were correlated, data were interpolated onto a 5-minute time scale. The data from each 24-hour profile was also looped around with each shift to ensure the length of data sets remained equal.

4.5 Cross-correlations between ionosonde parameters – EB040 (Roquetes)

For these plots data were used from 6 years' worth of Decembers from 2010 to 2015. F region analysis was computed over 24 hours with lags of 180 minutes and E region analysis between 9am and 3pm with lags of 60 minutes to ensure data availability.

4.5.1 Cross-correlations involving ionosonde E region parameters

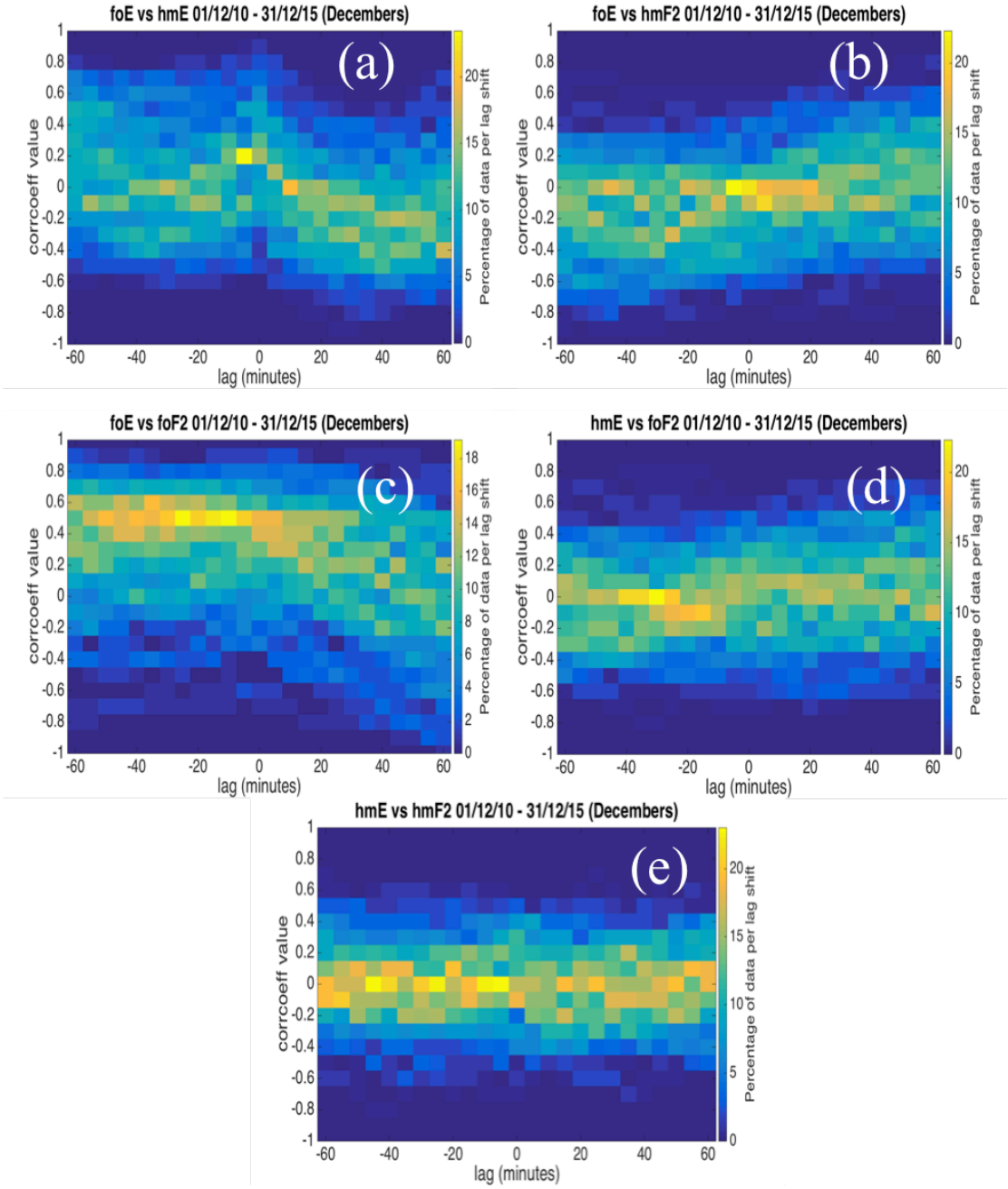

Figure 4.8: Correlations between parameters observed at the EB040 ionosonde (a) foE vs. hmE, (b) foE vs. hmF2, (c) foE vs. foF2, (d) hmE vs. foF2 and (e) hmE vs. hmF2. Negative lag indicates that the first parameter leads and second parameter lags.

Figure 4.8 shows the correlations between parameters involving the E region. Panels (a), (b), (d), and (e) show little correlation. The percentage bars suggest that a correlation of ±0.5 is not attained more than 15% of the time for panels (a), (b), (d) or (e) at any given lag. The correlation pattern is centred around a correlation of zero for each of these panels. Panels (a), (b) and (d) also show a

large range of correlation values at each lag. This is indicated by the broad width of the stripe and also by the low maximum percentage values across the plot. This suggests that a variety of correlation values were attained for each lag and implies that the amount of correlation between time series at given lags is not consistent. There is neither a consistent level of correlation or consistently no correlation. This suggests that there is no meaningful correlation between foE and hmE (panel a), foE and hmF2 (panel b) and hmE and foF2 (panel d) at all lags up to 60 minutes. The correlation rarely exceeds ±0.5 for these parameter pairs. Panel (e) shows a pattern strongly centred around a correlation of zero, with approximately 20% of the data showing a correlation between zero and ±0.2. This suggests that there is consistently no correlation between hmF2 and hmE at any lag.

A more interesting relationship is suggested by Figure 4.8 panel (c), comparing foE and foF2. The panel shows 18% of the data at correlations of approximately 0.5 at lags from approximately -5 to -25 minutes. This means that the time series of foF2 is correlating well with the time series of foE shifted backwards in time by 5 to 25 minutes. This pattern occurs as a result of the different times at which the two parameters reach their peak value. Figure 4.9 shows daily time series for both foE (panel a) and foF2 (panel b) for the month of December 2010.

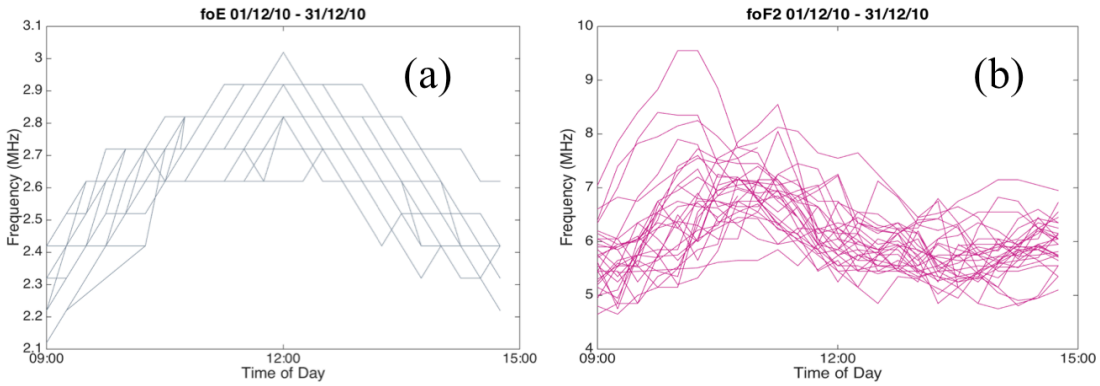

Figure 4.9: Daily time series of (a) foE and (b) foF2 between 9am and 3pm for December 2010.

Figure 4.9 panel (a) shows that peak foE is reached around noon, whilst panel (b) shows a local peak in foF2 before noon, followed by a slight dip in the hours following noon. During the correlation analysis the first time-series is fixed and the second is shifted. This results in a stronger correlation in negative lags, when the foE time series will be shifted to the left, meaning the peaks of foE and foF2 will move closer into alignment. This suggests that peak correlations between foE and foF2 are observed when foE values are aligned with foF2 values from approximately 20 minutes earlier. The lag time for this relationship may only be valid for the month of December as the local time at which the F2 peak occurs is known to change throughout the year (Hargreaves 1992).

4.5.2 Cross-correlations between ionosonde F region parameters

Unlike the E region, the F region persists overnight, making it possible to calculate cross-correlations between foF2 and hmF2 over a 24-hour period, as well as between 9am and 3pm to enable comparisons with those from the E region analysis. In order to demonstrate the impact of these different periods, Figure 4.10 shows correlations over the two time periods for 6 years of Decembers.

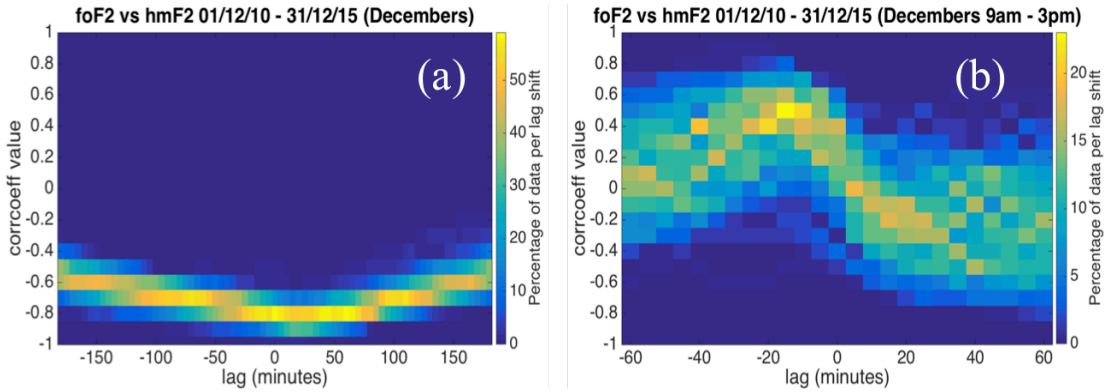

Figure 4.10: Cross-correlations between foF2 and hmF2 for the Roquetes ionosonde over (a) 24 hours and (b) between 9am and 3pm. Negative lag indicates that the first parameter leads and second parameter lags.

A strong anti-correlation reaching values of -0.8 and sustained for approximately 100 minutes is seen in Figure 4.10 panel (a) between foF2 and hmF2 over a 24-hour period. This suggests that consistently as foF2 increases hmF2 decreases. This result was expected as foF2 values increase towards noon and decrease afterwards as the electron density of the ionosphere (which is proportional to foF2) is solar radiation driven (see Figure 4.2). As solar irradiance increases, more energy is available to ionise the neutral particles, and the number of electrons increases. Consequently the electron density increases towards noon and decreases afterwards, as solar irradiance decreases. foF2 values follow the same pattern as they relate to the square root of the ionospheric electron density.

Contrastingly, hmF2 values are high in the morning and evening and lower through the middle of the day, as depicted in Figure 4.2. This pattern occurs due to the contribution of upwards dispersion (diffusion) of ions to the overall ionisation profile when the solar influence is lower. During the day the location of peak ionisation is at a point closer to where neutral particle availability for ionisation is in equilibrium with availability of solar ionising radiation (which is increasingly absorbed as it penetrates deeper through the atmosphere). Once neutral particles have been ionised they diffuse upwards as they have a higher temperature than their surroundings (Hargreaves 1979). This upwards diffusion continues at night when the absence of incoming solar radiation means

ionisation levels are significantly lower. As ions move upwards there are fewer neutral particles available and therefore less recombination, allowing the ions to persist for longer. This results in a point of peak electron density at a higher altitude than the point of peak daytime production. This results in the diurnal shape seen in Figure 4.2, where hmF2 values are higher at night than in the day. As the consequent time series of foF2 and hmF2 are opposites, an anticorrelation is observed between the two parameters.

Figure 4.10 panel (b) shows an interesting correlation pattern between foF2 and hmF2 between 9am and 3pm. The physical activity that occurs over 24hours is not present in the daytime analysis, so the anticorrelation seen in panel (a) is not noticeable. Correlation values in panel (b) are mostly centred around 0 with a peak of approximately 0.5 for over 20% of the data at lags of approximately -15 minutes, and a dip of roughly -0.5 from lags of 20 to 60 minutes for less than 20% of the data. To demonstrate these features, Figure 4.11 shows example time series of the two parameters between 9am and 3pm, and the consequent cross-correlation values acquired with the lag shift.

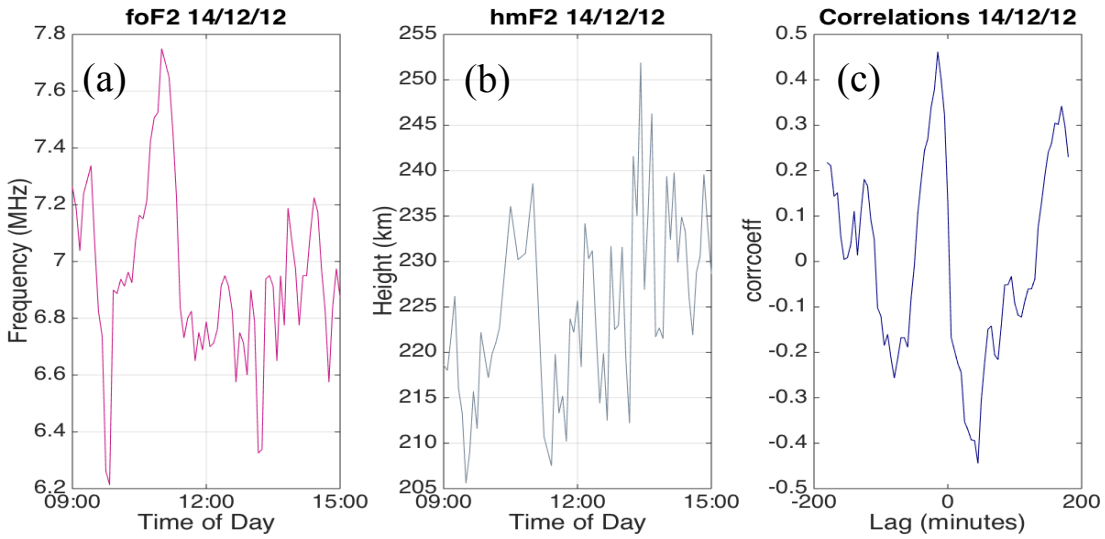

Figure 4.11: Investigation into 14/12/12 (a) foF2 time series (b) hmF2 time series (c) correlations between foF2 and hmF2. Negative lag (panel c) indicates that foF2 leads and hmF2 lags.

It can be seen in Figure 4.11 that there is a peak in both panels (a) and (b) before noon, and that panel (b) has dips on either side of this peak. This results in the pattern of anticorrelation, correlation and then anticorrelation peaks seen in panel (c). The 9am – 3pm foF2 time series frequently contained a peak just before noon. The hmF2 time series is usually erratic with local peaks and troughs that are minor in the 24-hour time series (see Figure 4.2 panel (b)), but which become more noticeable when the time series is shrunk to just 6 hours. This erratic hmF2 pattern reduces consistency in the 9am – 3pm correlations

between the two parameters. This is indicated by the maximum percentage in Figure 4.10 panel (b) which only exceeds 20% for one box. As the time series is only shifted by 60 minutes in each direction, and the hmF2 dips and peaks typically last for roughly an hour, there is only opportunity for a single peak and dip in correlation values. If the lag length was extended it is expected that more peaks and dips would be seen in the correlation results, as the peak in foF2 was shifted to align with hmF2 dips and peaks. This implies that the peak-trough correlation pattern seen in Figure 4.10 panel (b) is not scientifically meaningful, and also that there is not a short-term consistent correlation relationship between foF2 and hmF2 between 9am and 3pm.

4.6 Perturbations cross-correlations

To investigate how much of the correlation was driven by the ionospheric diurnal cycle; the diurnal cycle was removed from the 24-hour time series. The first method attempted to achieve this was to subtract the daily time series of each parameter as modelled by IRI-2012 (Bilitza et al. 2014) from the raw data. This proved to be unsuitable as comparisons between time series showed significant discrepancies between the sunrise and sunset times in the observational data and those modelled by IRI. Subtracting one from the other therefore introduced spurious correlations. Figure 4.12 shows 24-hour foF2 observations for the Roquetes ionosonde, with the IRI-2012 time series for the same dates, latitudes and longitudes. IRI-2012 and IRI-2016 (Bilitza et al. 2017) time series for these dates, latitudes and longitudes were identical.

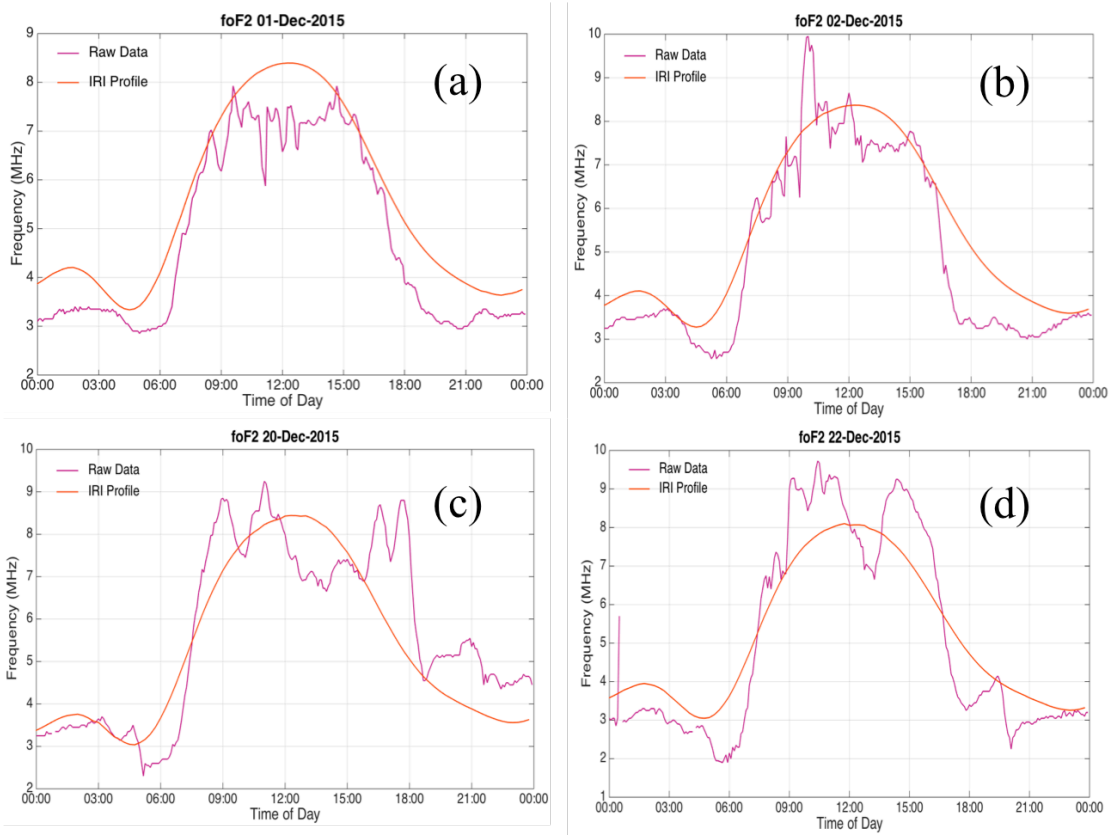

Figure 4.12: Time series for days in December 2015 of foF2 observations at the Roquetes ionosonde (pink) and IRI time series for the same latitude and longitude (orange).

Figure 4.12 panels (a) and (b) show the discrepancy between sunrise and sunset speeds between the raw data and IRI time series. The raw observations (pink lines) begin to rise after the IRI time series (orange lines) and fall faster than the IRI time series. The daytime hours are shorter for the observational data than for IRI. Panels (c) and (d) show a double diurnal maximum in the foF2 raw observations which is not present in the IRI time series. In both these scenarios the IRI profile begins to fall approximately 3 hours before the observation data. In all 4 panels sunrise occurs in the IRI time series approximately an hour before it is seen in the observational data.

The second technique attempted for removing the diurnal cycle was to create an averaged time series to subtract from raw data. In this method the time series from 15 days before and after a given day were averaged to create the time series. This approach was also unsuitable due to the frequent appearance of a dual peaked time series in the foF2 time series. Examples of this shape can be seen in Figure 4.12 panels (c) and (d). This shape is referred to as a 'diurnal double maxima' (Pi et al. 1993), and has previously been recognised in time series of foF2, hmF2 and TEC measurements (Katamzi 2011). The feature is observed as a trough between two peaks and can be referred to as a 'bite-out' when the trough is around noon (Pi et al. 1993; Katamzi 2011). It is thought that

at mid-latitudes the cause of the bite-out feature relates to the motion of meridional winds. If these winds are moving polewards around midday plasma can be moved to lower altitudes, where a higher availability of neutral particles available for recombination increases the ion loss rate (Pi et al. 1993).

When time series containing a diurnal double maxima were included in the attempt to create an average 30-day time series the resulting time series was unrealistic, and when subtracted from raw data this introduced spurious waves. The third idea was to combine the strengths of each of the previous techniques, and to scale the daily IRI time series using a monthly average. This technique also proved unsuitable as the averaged time series was drastically different from the given time series of each day.

The most suitable technique identified was to take a smoothed version of each day's time series and subtract this from the raw data. This left the perturbations around the diurnal cycle for each day. Figure 4.13 illustrates this process. Panel (a) shows the smoothed profile and the original data profile it was subtracted from to create the perturbations profile, which is shown in panel (b).

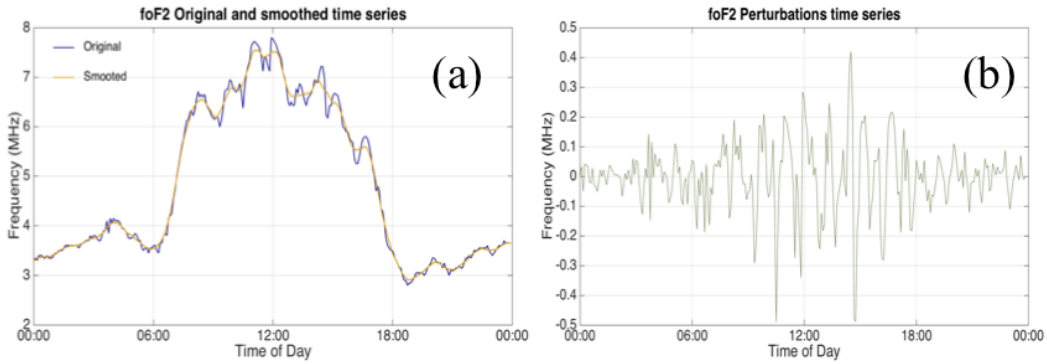

Figure 4.13: Creating perturbations profile (a) Original (blue) and smoothed (orange) time series, (b) resulting perturbations profile.

The correlation analysis was then completed again for each pair of parameters (foF2 vs hmF2, foF2 vs TEC, etc.) using only the perturbations outside of the diurnal cycle.

4.6.1 Perturbations cross-correlations of E region parameters

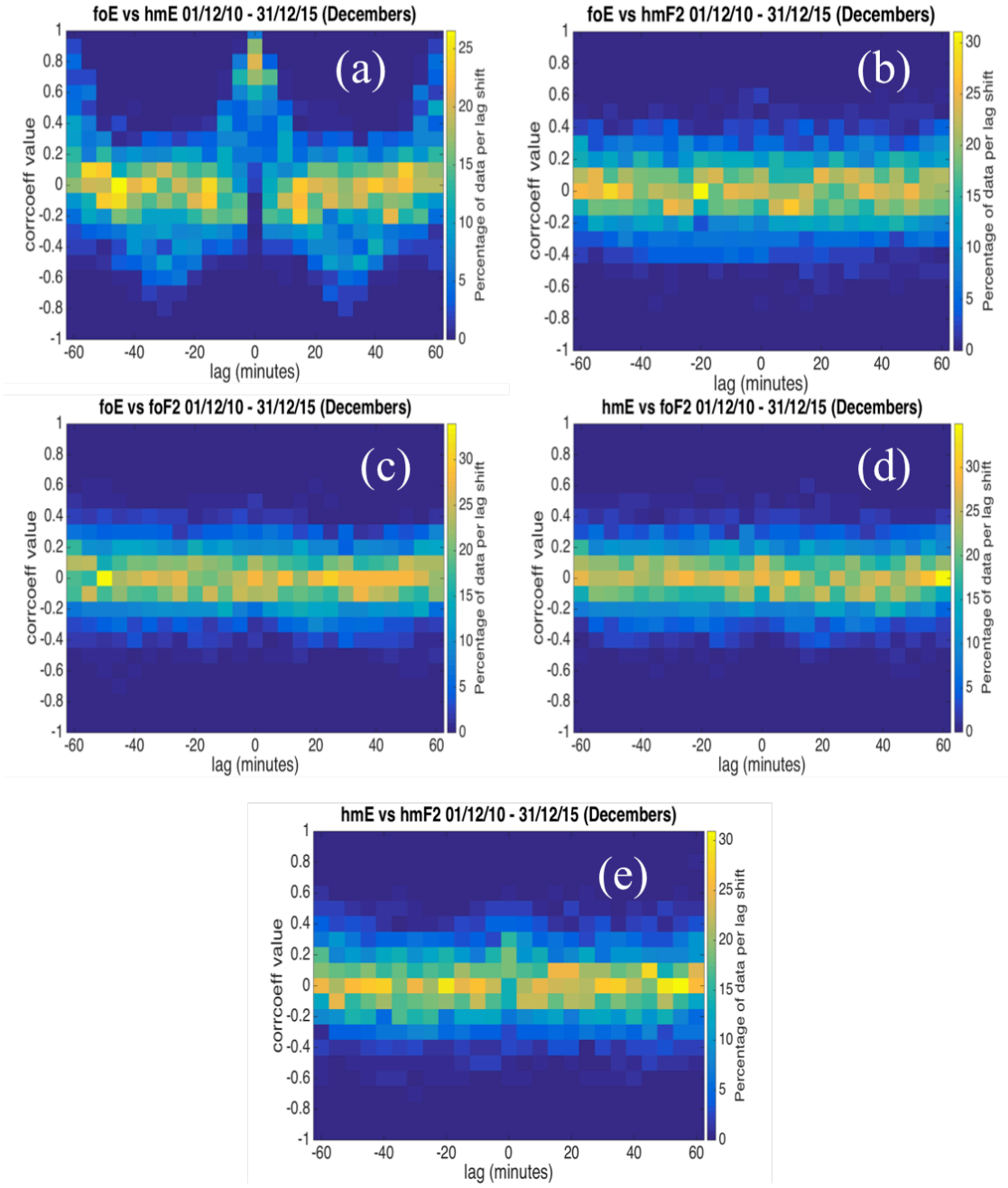

Figure 4.14: Perturbation cross-correlations for E region parameters (a) foE vs. hmE, (b) foE vs. hmF2, (c) foE vs. foF2, (d) hmE vs. foF2 and (e) hmE vs. hmF2. Negative lag indicates that the first parameter leads and second parameter lags.

Figure 4.14 panels (b), (c), (d) and (e) show that with the diurnal cycle removed there is rarely any significant correlations (above 0.5) between any pairs of ionosonde parameters. This is not surprising, as a significant amount of activity in the ionosphere is solar driven, and so with the impact of the sun removed there will be little connecting the two ionospheric regions.

It can be seen that there is an unusual pattern in Figure 4.14 panel (a), showing the correlations between foE and hmE. Further investigation showed that this spiky pattern was the result of the difference between manual and automatic scaling at the EB040 ionosonde. Automatic scaling recorded the foE values as those resulting from radio waves reflected by sporadic E, rather than from the actual E region maximum. This resulted in recorded foE and hmE observations being lower than the true values. Manual scaling corrected this to the value reflected by the actual E region, however this correction was only applied to hourly measurements. This resulted in hourly values being higher than the surrounding values, causing spikes in both the foE and hmE time series. Daily time series for foE and hmE for the months December 2012, where the spikes are absent, and December 2013, where the spikes are present, are shown in Figure 4.15.

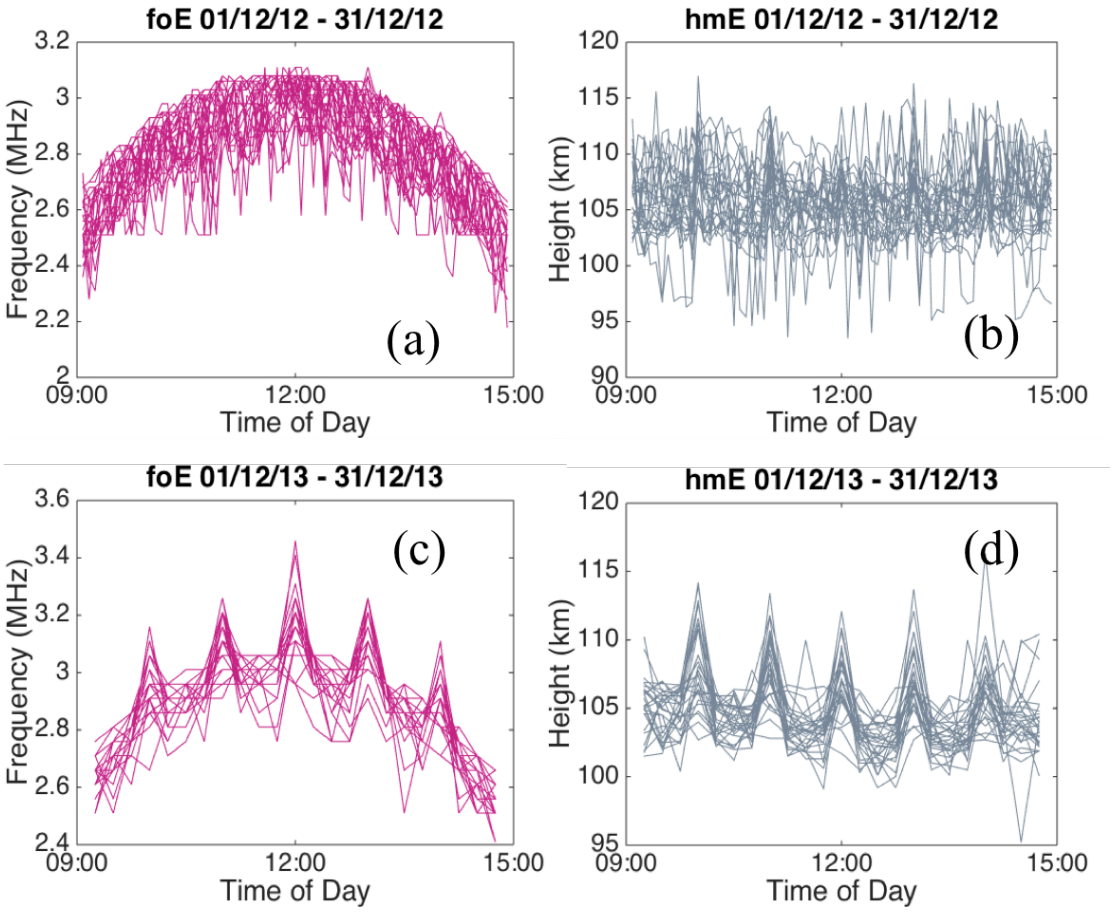

Figure 4.15: Daily time series from the EB040 ionosonde of (a) foE for December 2012, (b) hmE for December 2012, (c) foE for December 2013 and (d) hmE for December 2013.

As the method of removing the diurnal cycle was subtracting a smoothed time series, which didn't contain the spikes, the spikes remained in the perturbations time series. As the data are shifted during the lag correlation process the spikes correlate and anticorrelate. This causes the spiky pattern seen in the final

correlations and does not reflect any physical correlation relationship between the parameters. This spiky pattern was seen in the correlations results for December 2013 and December 2014 and was thus noticeable through into the final 6-year correlation results. A new dataset was created with the manual overrides removed from 2013 and 2014 (and therefore the spikes removed) and E region correlations were recalculated.

4.6.2 Cross-correlations of E region parameters repeated with spikes removed

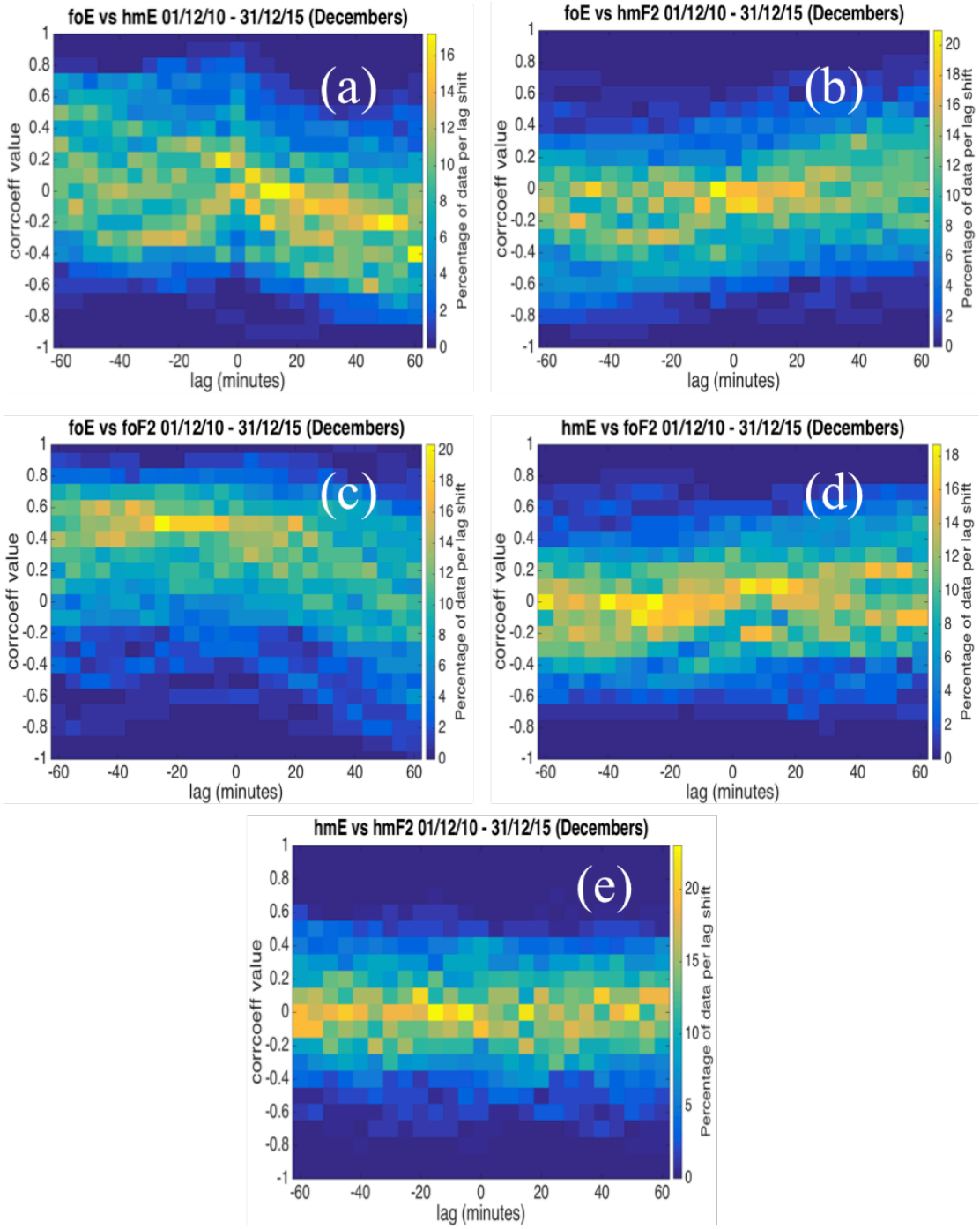

Figure 4.16: Cross-correlations between E region parameters observed at the EB040 ionosonde with spikes caused by manual scaling removed (a) foE vs.

hmE, (b) foE vs. hmF2, (c) foE vs. foF2, (d) hmE vs. foF2 and (e) hmE vs. hmF2. Negative lag indicates that the first parameter leads and second parameter lags.

Figure 4.16 shows that repeating the cross-correlation analysis after the removal of the E region spikes has made little difference to the overall correlation relationships. Figure 4.16 panels (a), (b), (d) and (e) show correlations between most variable pairs are centred around zero, and rarely surpass values of ±0.5 for more than 10% of the data. This suggests that there is no consistent correlation between time series of foE and hmE, foE and hmF2, hmE and foF2 or hmE and hmF2. Figure 4.16 panel (c) shows that the relationship between foE and foF2 also remains unchanged, with a peak correlation at a lag of -20 minutes for approximately 20% of the data, caused by the local peak of foF2 occurring earlier in the day than the foE peak.

4.6.3 Perturbations cross-correlations of E region parameters repeated with spikes removed

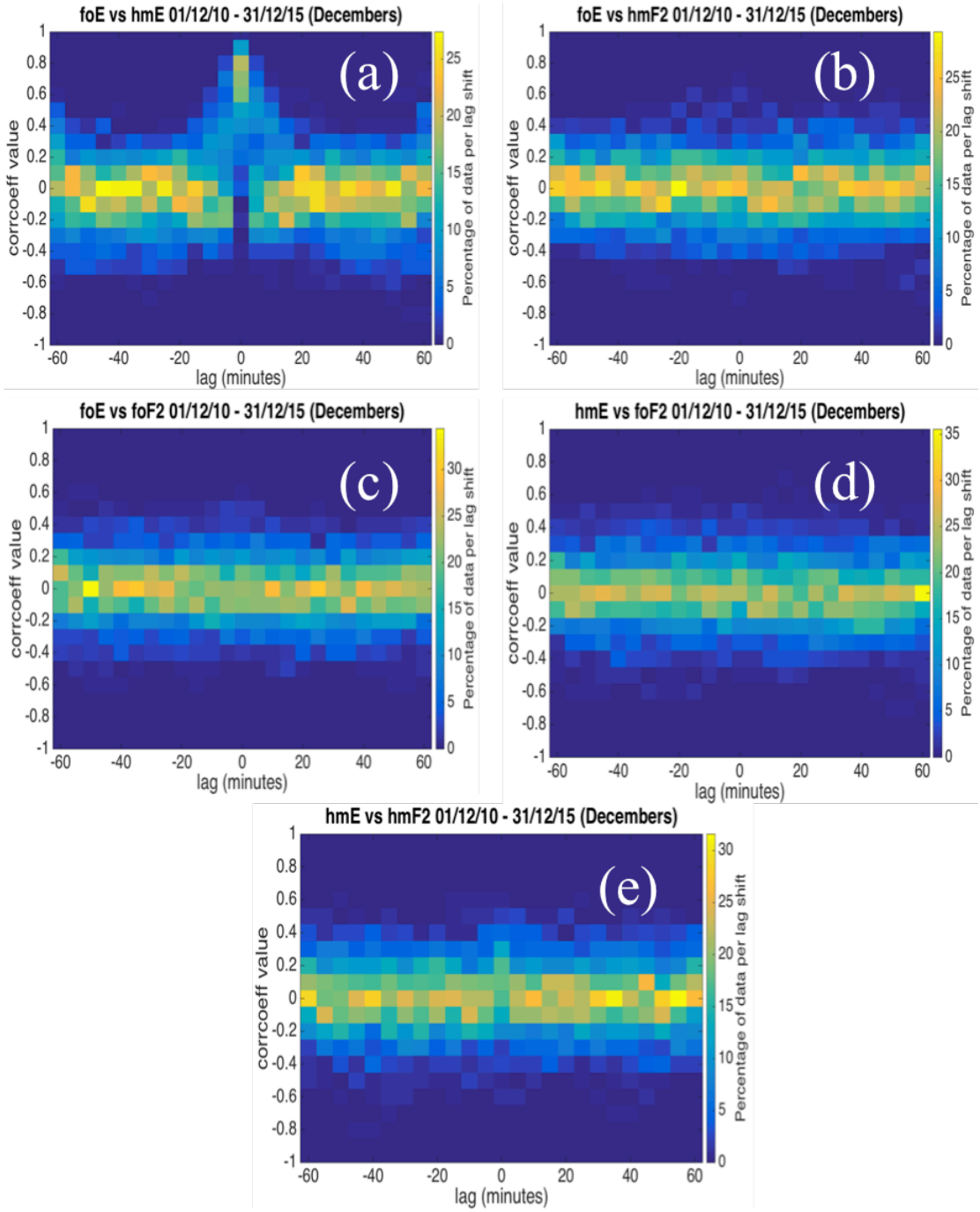

Figure 4.17: Perturbation correlations for E region parameters with spikes caused by manual scaling removed (a) foE vs. hmE, (b) foE vs. hmF2, (c) foE vs. foF2, (d) hmE vs. foF2 and (e) hmE vs. hmF2. Negative lag indicates that the first parameter leads and second parameter lags.

Figure 4.17 shows that there is no correlation between most perturbation time series pairs. Note: although Figure 4.17 looks very similar to Figure 4.14, there

are subtle differences. In Figure 4.17 over 25% of the data has a correlation close to 0 at all lags with little data surpassing correlations of 0.4 or -0.4 for (b) foE vs. hmF2, (c) foE vs. foF2, (d) hmE vs. foF2 and (e) hmE vs. hmF2, suggesting that there is no correlation between these parameter pairs when the diurnal cycle is removed.

A different relationship is seen in panel (a), which depicts the cross-correlations of the perturbation time series of foE and hmE. Removing the spikes from the raw data has removed the anti-correlation peaks at ±30 minutes and the peaks at ±60 minutes, however a peak correlation of around 0.8 is seen at zero lag for approximately 20% of the data. The cause of this has not yet been identified, however when the process was repeated using other ionosondes a similar relationship was seen. This is shown in Figure 4.18.

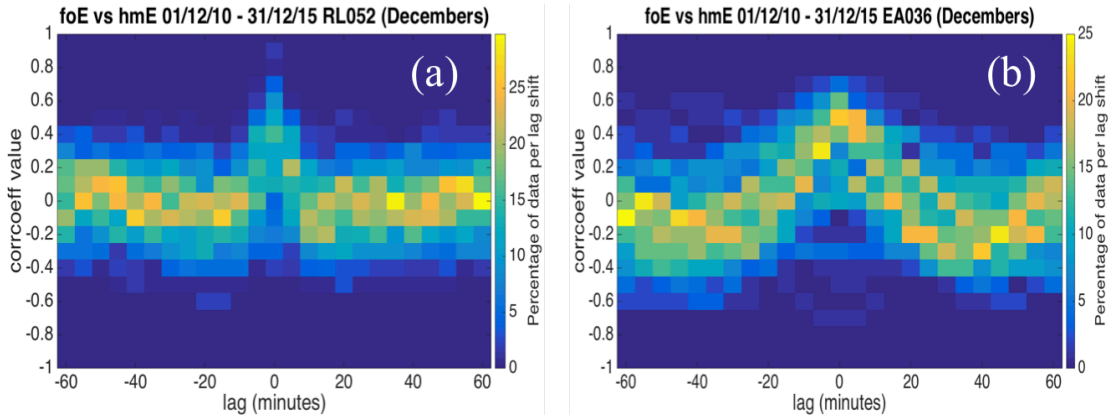

Figure 4.18: Perturbation correlations foE and hmE time series at ionosondes (a) RL052 and (b) EA036. Negative lag indicates that the first parameter leads and second parameter lags.

Figure 4.18 shows the results of the cross-correlation analysis between the perturbation time series of foE and hmE at the RL052 (panel (a)) and EA036 (panel (b)) ionosondes. Panel (a) shows little correlation between the parameters at most lags, with correlations centred around 0. A peak is noticeable at zero lag, where approximately 15% of the data reach a correlation of 0.4. A peak at zero lag is also seen in panel (b) for over 20% of the data at a cross-correlation of 0.5. The cause of this peak has not yet been identified.

4.6.4 Perturbations cross-correlations of foF2 and hmF2

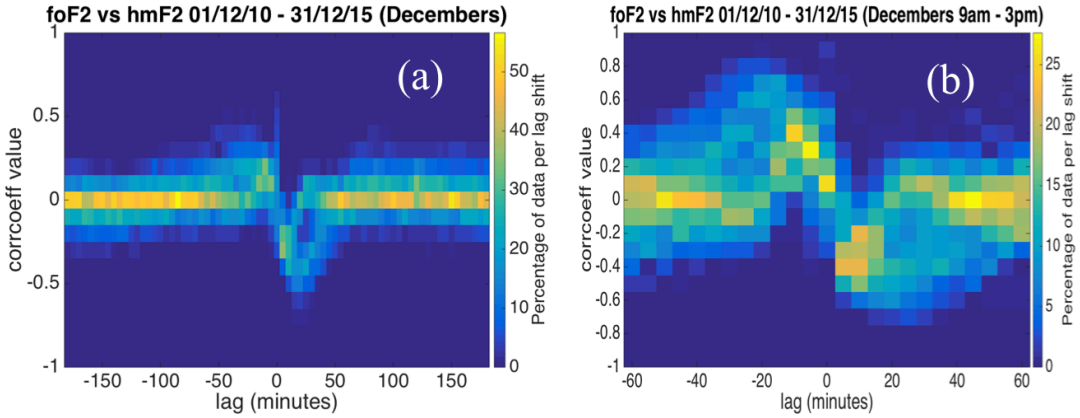

Figure 4.19: Perturbation correlations between foF2 and hmF2 over (a) 24-hours and (b) between 9am and 3pm. Negative lag indicates that the first parameter leads and second parameter lags.

Figure 4.19 Panel (a) shows correlations are centred around zero. There is a dip in correlations reaching a minimum value of -0.5 for roughly 30% of the data. Panel (b) also shows little correlation. Correlations are centred around zero for over 20% of the data over most lags. A similar peak trough pattern to that seen in Figure 4.10 panel (b) is observed. This pattern again appears to result from the erratic behaviour observed when the profiles are limited to six hours, which is still present when the diurnal cycle has been removed. The deviations from 0 in both panels are therefore not thought to be meaningful, and the perturbations time series of foF2 and hmF2 can be considered to have only spurious correlations.

Figures 4.17 and 4.19 show that the correlation between ionosonde parameters drops significantly when the diurnal cycle is removed from the 24-hour data, but that there is less of a difference for the 9am – 3pm data. This is logical as the dawn and dusk transitions (which are responsible for the strong anticorrelation seen in the 24-hour raw data cross-correlations) are excluded from the 9am – 3pm plots.

Analysis shows no correlation between E region and F region parameters and no significant correlation between most parameter pairs in the same region. This suggests that the majority of the correlations seen before the diurnal cycle was removed were the result of solar driving. This suggests that without the diurnal cycle it is not possible to discern information indicating the behaviour of one parameter in relation to another.

4.7 Cross-correlation between ionosondes

To assess ionospheric correlations spatially, ionosonde parameters were also correlated between different ionosondes. In this analysis a variable from one ionosonde was correlated with the same variable from a different ionosonde, using December data from 6 years, (2010 – 2015). E region parameters were correlated with lags of 60 minutes on either side of time 0 between the hours of 9am and 6pm, F region parameters for lags of 180 minutes before and after time 0 for 24-hour time series. The ionosondes investigated are Roquetes (EB040), Athens (AT138), El Arenosillo (EA036) and Chilton (RL052), the locations of which are shown in Figure 4.4. E region data for the EB040 ionosonde had the spikes caused by manual scaling removed. Table 4.1 shows approximate local time differences between the locations of the four ionosondes.

Table 4.1: Time differences between ionosonde pairs used in cross-correlation analysis.

Ionosonde Pair	Time Difference
EB040 to AT138	90 minutes
EB040 to EA036	30 minutes
EB040 to RL052	10 minutes
RL052 to EA036	20 minutes

Panels (a), (b), (c), and (d) of Figure 4.20 show cross-correlations between foF2 time series for 4 pairs of ionosondes.

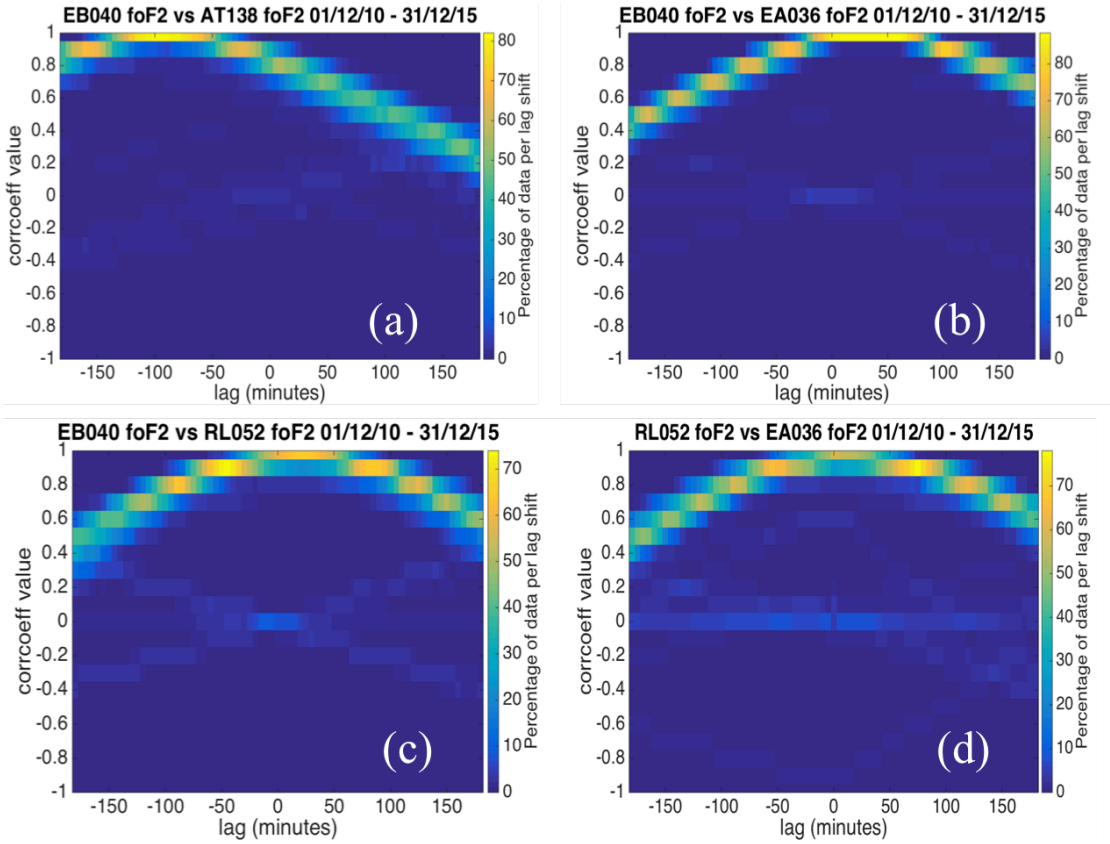

Figure 4.20: Cross-correlation analysis between pairs of foF2 time series (a) Eb040 and AT138, (b) EB040 and EA036, (c) EB040 and RL052 and (d) RL052 and EA036. Negative lag indicates that the first parameter leads and second parameter lags.

Correlations in Figure 4.20 are high, peaking above 0.9 for all 4 ionosonde pairs for over 70% of the data. The lag at which peak correlations are attained show a slight shift from zero. This is logical, as foF2 is solar driven and peak values will be related to local time. The lag shift of the peak is therefore probably the result of local solar time difference between observations, which can be seen in Table 1. The time difference for example between EB040 (Roquetes) and AT138 (Athens) is approximately 90 minutes, which is also the offset of the maximum peak seen in panel (a). Correlations remain above a value 0.5 for approximately 150 minutes from the peak. This suggests foF2 values are strongly correlated between locations in Europe and remain so for roughly 150 minutes.

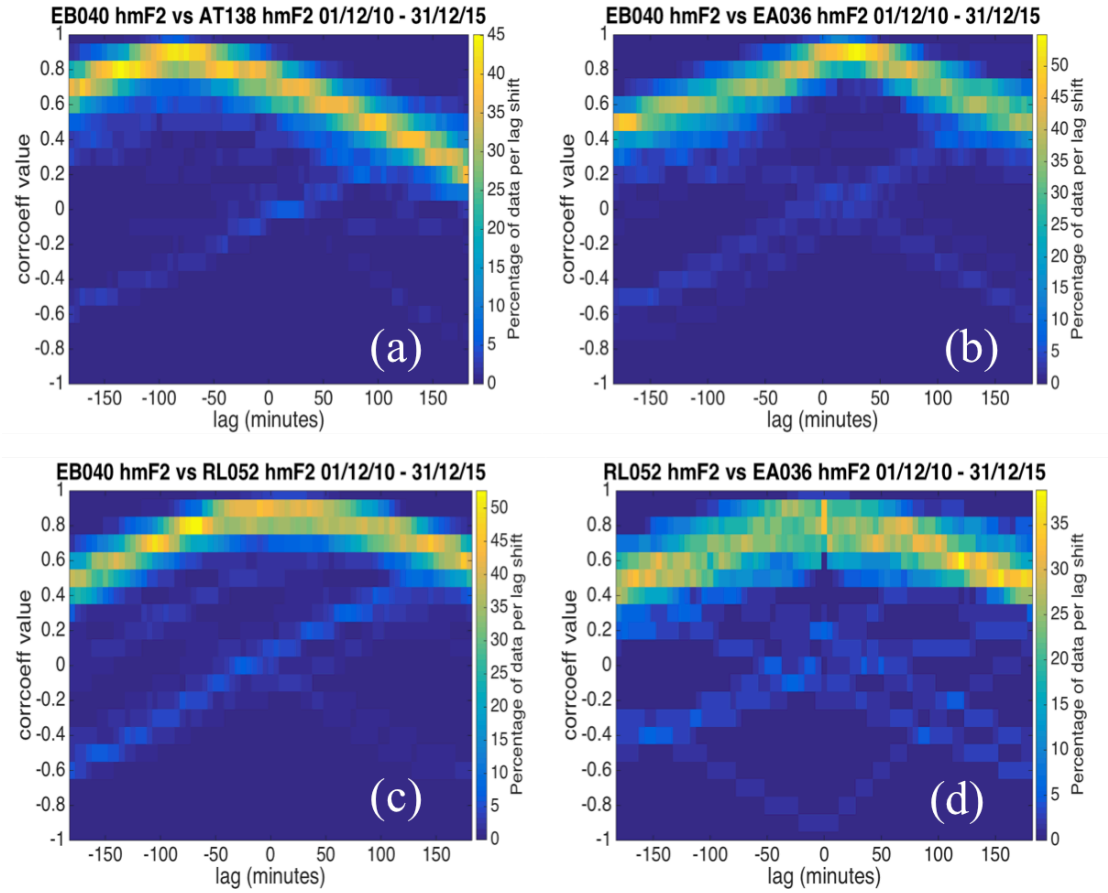

Figure 4.21: Cross-correlation analysis between pairs of hmF2 time series (a) EB040 and AT138, (b) EB040 and EA036, (c) EB040 and RL052 and (d) RL052 and EA036. Negative lag indicates that the first parameter leads and second parameter lags.

Figure 4.21 shows cross-correlations between hmF2 values from pairs of ionosondes. Correlations are slightly lower than for foF2 pairs but are still high, with peak values reaching above 0.8, with a lag shift at which the peak is located again due to time difference between stations. For panels (a) and (b) the peak is sustained over approximately 50 minutes, with over 45% of the correlations surpassing 0.8. However, for panel (c) the peak is sustained for noticeably longer, with roughly 50% of the data having correlations over 0.8 from lags of -50 to +50 minutes. Figure 4.4 shows that the two ionosondes compared in panel (c), EB040 and RL052, are much closer together longitudinally. It should also be noted that their similar longitudes cause the centre of the peak to be less shifted in panel (c) than in panels (a) and (b). Panel (d) shows a less pronounced peak than the other three panels, however peak correlations are above 0.8 for over 35% of the data. Correlations remain above 0.5 for at least 100 minutes from the centre of the peak in every hmF2 comparison panel. Figure 4.21 suggests that hmF2 time series are well correlated across Europe and may remain correlated for a larger amount of time for ionosondes at similar longitudes than for those at more different longitudes.

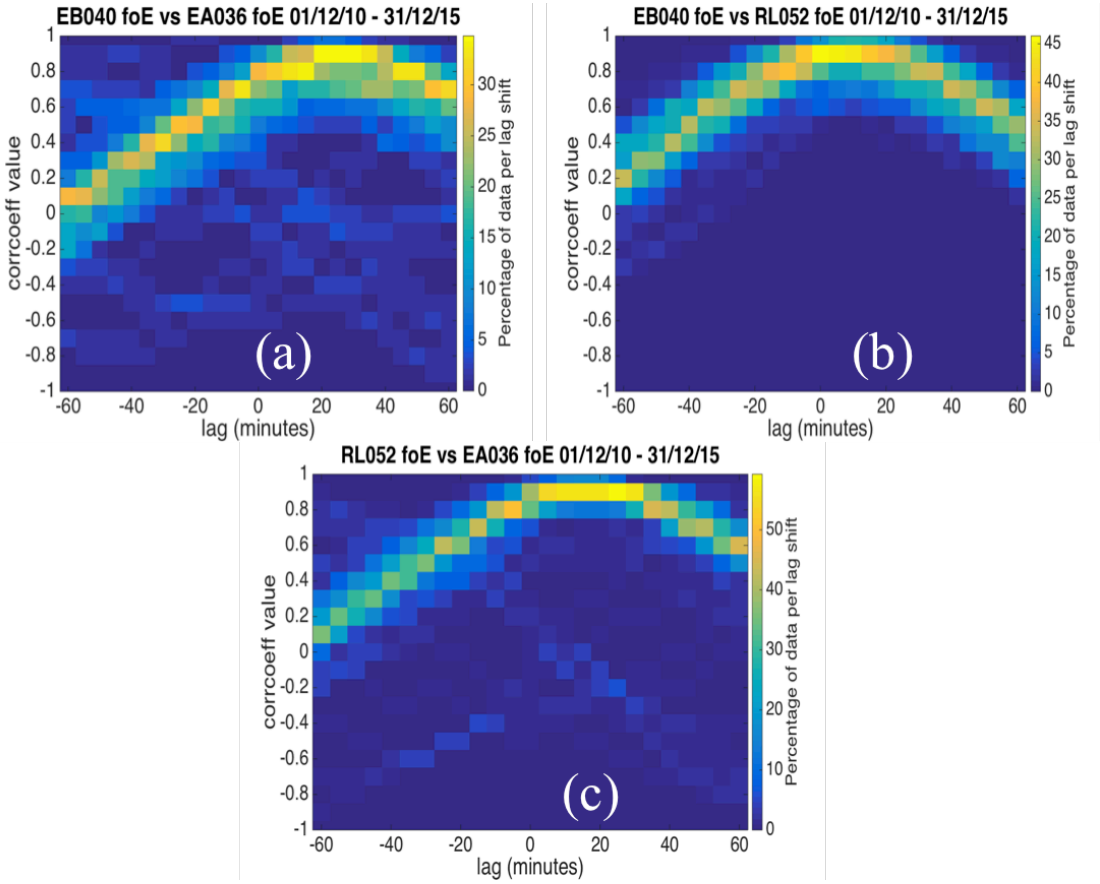

Figure 4.22: Cross-correlation analysis between pairs of foE time series (a) EB040 and EA036, (b) EB040 and RL052 and (c) RL052 and EA036. Negative lag indicates that the first parameter leads and second parameter lags.

Analysis of E region parameters between ionosondes showed a different correlation pattern than between parameters in the F region. Figure 4.22 shows cross-correlations between foE time series at different ionosonde station pairs. AT138 had insufficient data to complete the analysis. Peak values are high in all panels with correlations above 0.8 for over 30% of the data. Peak correlations are sustained for less time for foE, over lag shifts of between approximately 20 and 40 minutes, than for either of the F region parameters. The correlations decrease from the peak faster for foE than for foF2 or hmF2, falling below a value of 0.5 after ±50 minutes.

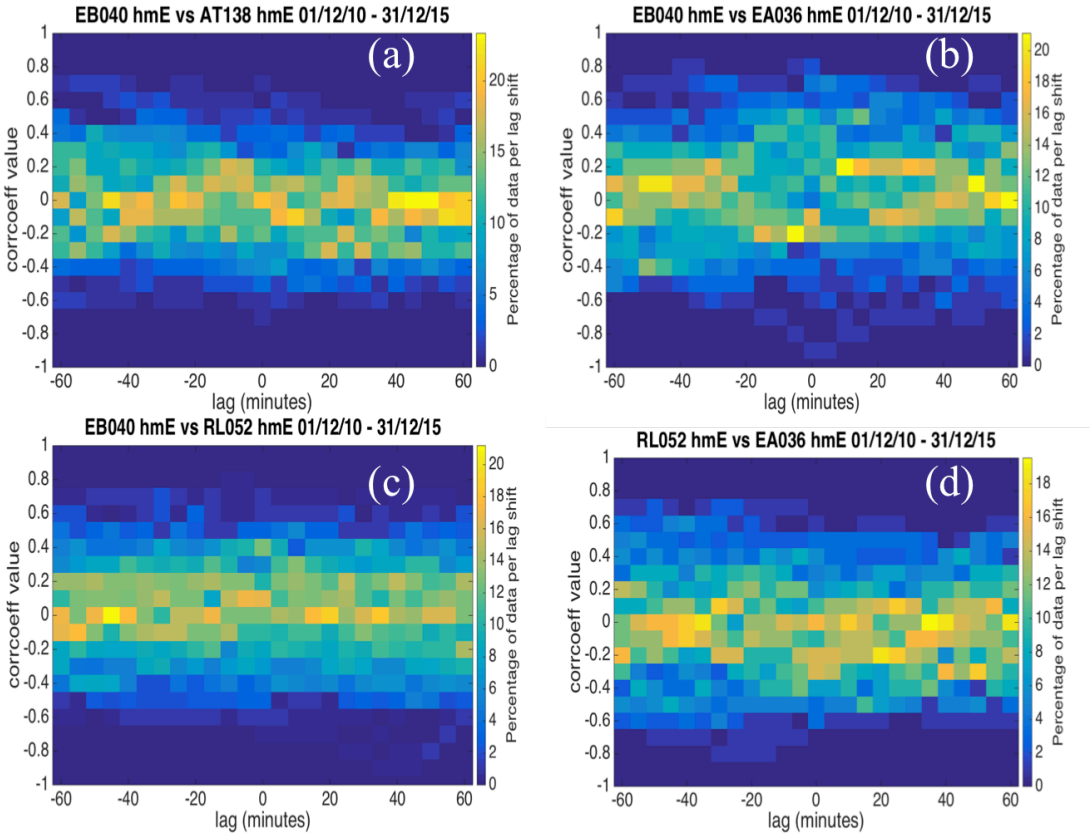

Figure 4.23: Correlation analysis between pairs of ionosondes in Europe hmE observations (a) EB040 and AT138, (b) EB040 and EA036, (c) EB040 and RL052 and (d) RL052 and EA036.

Figure 4.23 shows correlations between hmE observations between ionosonde pairs. These panels show there is very little correlation between hmE time series between ionosondes. The correlation band is centred around zero and rarely exceeds a correlation of ±0.4 in all panels.

4.8 Cross-correlations between ionosonde and GPS measurements

Data from the EB040 (Roquetes) ionosonde has been cross-correlated with TEC data obtained using the GPS receiver Hueg for every day in 2015. The locations of EB040 and the Hueg receiver are shown in Figure 4.4. GPS 24-hour time series were discarded if the data was assessed to show an unrealistic time series, or if more than 15% of the time series was missing. Full details on how GPS days were discarded is discussed in Section 5.5.2 of Chapter 5: 'Preliminary inspection of relative TEC time series'.

Figure 4.24 shows cross-correlations between the Hueg GPS receiver and the Roquetes ionosonde parameters. E region parameters were cross-correlated between 9am and 3pm for 60 minutes on either side of time zero, F region parameters for 24 hours with lags of ±180 minutes.

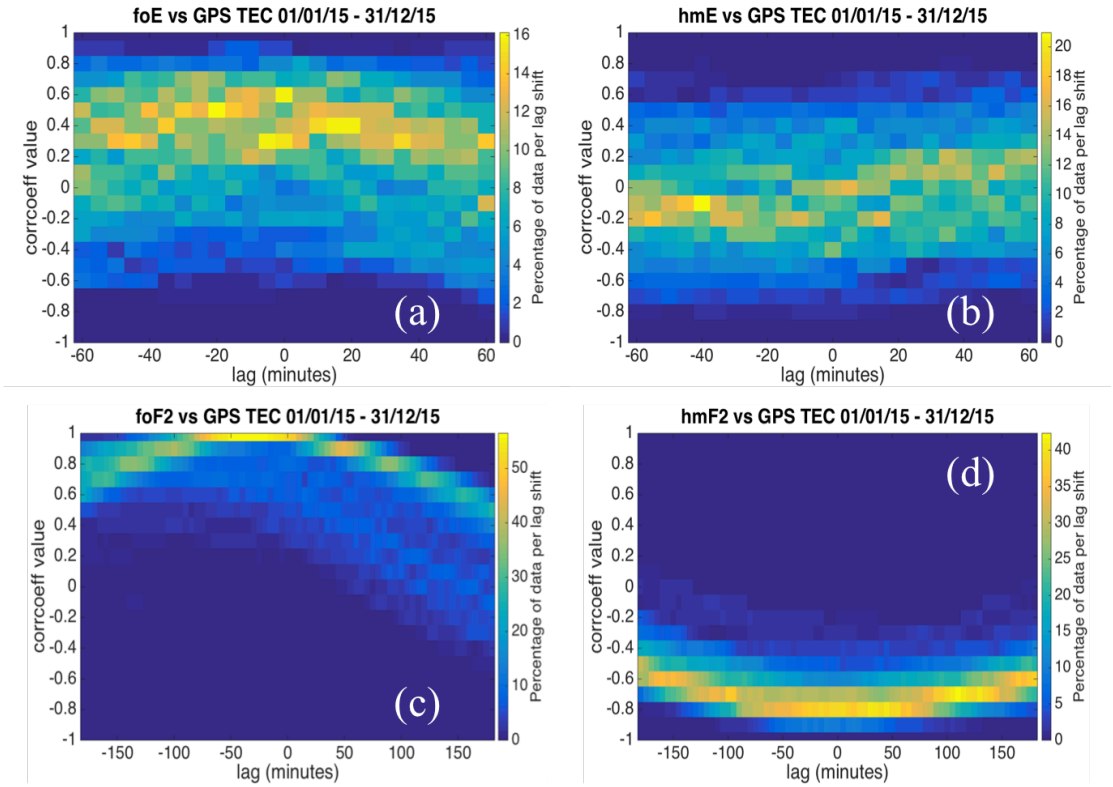

Figure 4.24: Cross-correlations between ionosonde parameters observed at EB040 and GPS derived TEC at Hueg (a) foE and TEC, (b) hmE and TEC, (c) foF2 and TEC, and (d) hmF2 and TEC. Negative lag indicates that the first parameter leads and second parameter lags.

Figure 4.24 panel (a) shows that cross-correlations between foE and GPS TEC peak at a value of around 0.5, with approximately 16% of the data, at a time zero. Peak correlation values then fall to approximately 0.3 as the number of time shifts increases. The thickness of the band through the plot shows a wide range of correlation values were obtained over the year for each time shift and suggests a lack of consistency of correlation. No single correlation value was attained for more than 16% of the data at any lag. Panel (b) shows the correlation between hmE and GPS TEC, and shows that there is no significant correlation between the two variables.

Panel (c) shows a strong correlation between ionosonde foF2 and GPS TEC, with over 50% of the data having a correlation close to 1 for approximately 50 minutes. A correlation between these two parameters is logical as the two are directly related; both are solar driven and related to the electron content of the ionosphere. The F region of the ionosphere is the most dense, and it is the F2 layer that provides the biggest contribution towards TEC (Mosert et al. 2002). This is illustrated in Chapter 2 section 2.2, which shows electron density as a function of altitude and demonstrates the dominant contribution of the F2 region to TEC. Consequently, foF2 and TEC should correlate well. This plot implies that as the electron density of the peak point in the F2 region increases, the

electron density of a column though the ionosphere also increases, which is logical. There is an offset from time zero at which peak correlation values are centred. This offset is roughly equal to local solar time difference, which between EB040 and Hueg is approximately 30 minutes. Peak values for both foF2 and TEC will occur at local noon, as both parameters are solar driven. Consequently the highest correlation values will be attained at the shift where local noons align.

Panel (d) shows a strong anticorrelation between hmF2 and GPS TEC, with cross-correlations of -0.8 seen for over 35% of the data for time shifts extending over approximately 100 minutes. An anticorrelation between these two parameters was expected. As shown and discussed in Section 4.5, hmF2 and foF2 are strongly anticorrelated for lags of at least 100 minutes. As TEC and foF2 are directly related and highly correlated, as illustrated in panel (c), logical inference suggests an anticorrelation between hmF2 and TEC. This implies that whilst the electron density of a column through the ionosphere increases towards local noon and then decreases towards local sunset, the height of the point of peak electron density in the ionosphere does the opposite.

4.9 Perturbations cross-correlations between ionosonde parameters and GPS derived TEC

As Section 4.6 demonstrated that there was no significant correlation between ionosonde parameters once the effects of solar driving had been removed, it seems likely that there will be little correlation between perturbations around the diurnal cycle of ionosonde parameters and GPS derived TEC. However, for the sake of completeness, correlations were calculated with the diurnal cycle removed nonetheless. The diurnal cycle was again removed from a time series by subtracting a smoothed version of the time series from the raw data.

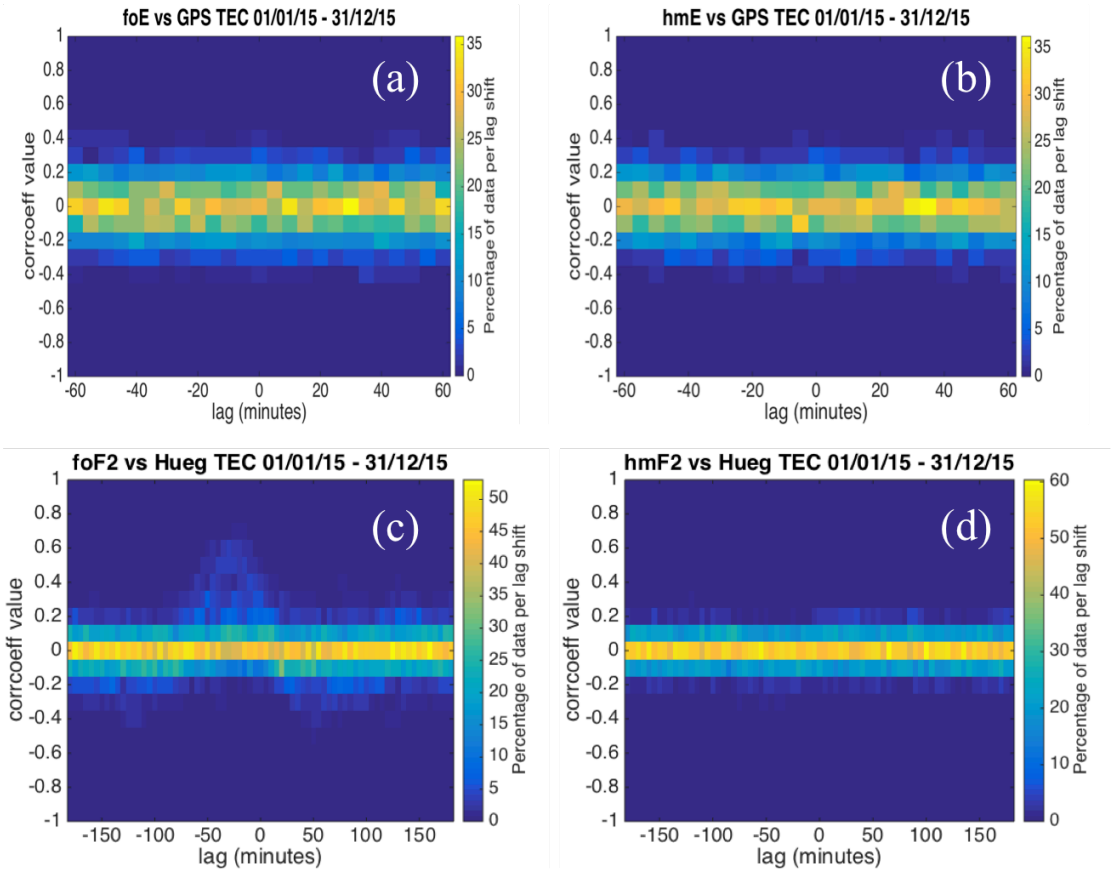

Figure 4.25: Cross-correlations between perturbations time series of parameters observed by the Roquetes ionosonde and TEC derived at the Hueg receiver (a) foE and TEC, (b) hmE and TEC, (c) foF2 and TEC, and (d) hmF2 and TEC.

Across all four panels of Figure 4.25 it can be seen that there are no, or very small, correlations outside of the diurnal cycle, with correlations rarely exceeding a value of 0.3 This suggests that outside of the diurnal variation there is no clear statistical correlation between ionosonde parameters and GPS derived TEC.

4.10 Chapter 4 conclusions

This chapter investigates the relationships between several ionospheric parameters using a cross-correlation statistical analysis. Correlations between 24-hour time series of ionosonde observed foE, hmE, foF2 and hmF2 were analysed using December data for 6 years. Cross-correlations involving GPS TEC were investigated using data from all 12 months of the year 2015. Correlations were found between 24-hour time series of the raw data and 24-hour time series data with the diurnal cycle removed, over 180 minutes surrounding time zero for the F region, and ±60 minutes for the E region.

The analysis showed there was little correlation between pairs involving E region parameters, the only exception being between foE and foF2, which show a peak

correlation of approximately 0.5 from lags of 0 to -20 minutes for over 15% of the data. The shift at which this peak occurs is due to the different times at which these variables attain their peak, with peak foE occurring close to noon and peak foF2 slightly before. The lag time at which this correlation has been observed may only be observed in December, as the F2 peak is known to occur at a different time through the year. Cross-correlating foF2 with hmF2 over 24 hours resulted in a strong anticorrelation peaking at a cross-correlation of -0.8 and sustained for approximately 100 minutes.

When attempting to identify a technique suitable for removing the diurnal cycle from ionosonde observations it was found that time series of foF2 generated by IRI-2012 and IRI-2016 show large discrepancies with observational data. The discrepancies were largest at sunset and sunrise, and were more significant if a double diurnal maximum was present in observational data. The diurnal cycle was thus removed using a smoothing technique. Cross-correlation analysis of time series without the diurnal cycle showed that there was little correlation outside of solar driving for most ionosonde parameter pairs. An interesting relationship was observed between the perturbation profiles of foE and hmE, which peaked at a cross-correlation of 0.8 at zero lag for roughly 20% of the data. A peak between the perturbation profiles of these parameters was also observed at the EA036 ionosonde, where at time 0 over 20% of the data had a correlation of 0.5. The cause of this peak has yet to be identified.

Correlations between pairs of ionosondes in Europe were also conducted. Correlations were high for foF2, peaking at above 0.9 and sustaining this peak for roughly 150 minutes. Correlations remained above 0.5 for the full 180 minutes of lag shifts. hmF2 time series were also well correlated, peaking above 0.8. hmF2 correlations showed a greater variation in the time peak correlation was sustained, ranging from approximately 50 minutes for 2 pairs and closer to 100 for the other 2. Peak foE correlations were again high at above 0.8 and sustained for 20 to 30 minutes. foE correlations fell from peak rapidly and only remained above a value of 0.5 for 20 to 40 minutes from the peak. Comparisons for hmE time series showed almost no significant (above 0.4) correlation for this parameter between ionosondes. A shift in the lag location of the peak in all ionosonde to ionosonde correlations for foE, foF2 and hmF2 was observed due to the time difference between ionosondes.

Cross-correlations were also found between ionosonde parameters and GPS derived TEC. Correlations peaked at 0.5 between TEC and foE, and no correlation was observed between TEC and hmE. TEC and foF2 were strongly correlated, peaking above 0.9 and sustaining this value for roughly 50 minutes. A strong anticorrelation was seen between hmF2 and GPS TEC peaking at -0.8 and being sustained for roughly 100 minutes. Any significant correlation between any ionosonde parameter and GPS TEC was absent when the diurnal cycle had

been removed from both parameters.

The results from this Chapter suggest that the strongest correlated pairs of parameters are foF2 and hmF2; foF2 and GPS TEC and hmF2 and GPS TEC. Strong correlations were seen between foF2 and GPS TEC, and strong anticorrelations between hmF2 and GPS TEC. In Chapter 5 we will use a correlation analysis to show the value of new single frequency observations of the ionosphere.

Chapter 5

Measurement of ionospheric total electron content using single frequency geostationary satellite observations

Abstract
In this chapter we demonstrate a technique which enables TEC to be derived using single frequency signals passing between geostationary satellites and terrestrial Global Positioning System (GPS) receivers. As the signals come from geostationary satellites this offers the key advantage that the ray-paths are not moving and hence are easier to interpret than standard GPS TEC. To demonstrate the technique, daily TEC time series are derived for three ground receivers from Europe over the year 2015. The technique is validated by correlation analysis described in Chapter 4 both between pairs of ground receiver observations and between ground receivers and independent ionosonde observations. The correlation between pairs of receivers over a year shows good agreement. Good agreement was also seen between the TEC time series and ionosonde data, suggesting the technique is reliable and produces realistic ionospheric information on a routine basis. The technique is not suitable for use on every GPS receiver type because drift in derived TEC values was observed for profiles calculated using receivers without links to highly stable clocks. The technique has the potential to become a routine method to derive TEC, helping to map the ionosphere in real time and to mitigate ionospheric effects on radio systems.

The results of this chapter were accepted by Radio Science in *Cooper et al 2018*

5.1 Introduction

5.1.1 Chapter aims

In the previous Chapter it was determined that time series of Global Positioning System (GPS) derived total electron content (TEC) were well correlated with ionosonde time series of both foF2 and hmF2. Correlations between GPS derived TEC and ionosonde observed foF2 peaked above a value of 0.9 and remained at this value for 50 minutes of shifts. GPS is a useful data source as it is less susceptible to interruptions, so in situations where ionosonde measurements are absent GPS measurements may remain uninterrupted. However, the technique must first be validated and the limitations assessed.

The aims of this chapter are as follows:

1. Does the technique for TEC derivation produce realistic results?
2. Does the technique produce realistic results consistently?

3. Are TEC time series derived via the technique well correlated between GPS receivers and with independent ionosonde observations?

The motivation behind this is to validate the single frequency GPS TEC derivation technique to investigate its performance, and to explore the relationship between GPS and ionosonde TEC.

5.1.2 Background

Understanding the state of the ionosphere is important for maintaining accuracy of earth-satellite communications and navigation systems. One such system that is significantly affected by the ionosphere is the Global Positioning System (GPS), which operates at frequencies between 1.1 and 1.6 GHz. To ensure accuracy, ionosphere dependent corrections must be made to GPS systems. The delay experienced by a signal travelling through the ionosphere is proportional to the total electron content (TEC) along the signal path. TEC is the line integral of the electron density of a column through the ionosphere, and is calculated along a signal path between a satellite and a ground-based receiver (Bust & Mitchell 2008). Consequently, if the signal path from satellite to ground is known, the differential delay experienced by two frequencies of the signal can be used to derive the TEC along the signal path.

Scientific investigations of TEC began with the emergence of artificial satellites as a tool for providing ionospheric measurements, as described in the review paper by Mendillo 2006. Using artificial satellites to investigate the ionosphere was first proposed as a method separately by Daniels (Daniels 1956) and Pfister (Pfister 1956) in 1956. First measurements were made by Daniels in 1959 (Daniels & Bauer 1959) by analysing the Faraday rotation of satellite signals. Observations of TEC have been taken for many decades using Faraday rotation from geostationary satellites, where the change in the angle of polarisation of a signal travelling from a satellite to the ground is related to the TEC along the path through the ionosphere (Hargreaves 1979; Ratcliffe 1972). This technique is less than ideal however, as changes in ionisation height can mean approximations made about the state of the local magnetic field become inaccurate and can cause inaccuracies of up to 20% in TEC estimations (Hargreaves 1992). This occurs as Faraday rotation relates to both the magnetic field strength and the ionisation, so the distribution of the ionisation along the path can cause an inaccuracy in the TEC estimation.

Since 1992 dual-frequency radio observations have been available as a method for deriving TEC using the GPS network (Mannucci et al. 1999). Dual frequency observations use the differential temporal delays of phase coherent radio signals to infer values of TEC, or the differential phase advance. Dual frequency receivers can use signals of two different frequencies to remove positioning errors from calculations. The majority of TEC values today are derived using

receivers from GPS networks, which need to account for the ionospheric delay to their signals for optimal accuracy (Bust & Mitchell 2008). The large global distribution of GPS receivers provides a higher network density for TEC observations than is possible for other ionospheric measurements (such as ionosonde or incoherent scatter radar observations), which combined with high sampling rates results in worldwide coverage of continuous, near-real time TEC observations (Mendillo 2006; Mannucci et al. 1999). TEC measurements have been frequently used to analyse the ionospheric storm response, due to the reduced vulnerability of GPS TEC measurements to storm effects when compared to other ionospheric measuring technologies such as ionosondes (Mendillo 2006).

Geostationary satellite dual-frequency signals have been used recently to derive TEC with dual frequency receivers, such as by Kunitsyn et al, 2015 (Kunitsyn et al. 2015). Geostationary satellite signals have also been used to investigate ionospheric scintillation by Cerruti et al. 2006. Observations made using geostationary satellites and ground receivers are particularly useful, as the point at which the signal intersects the ionosphere (ionospheric pierce point) does not change as it does for non-geostationary satellites (Kunitsyn et al. 2015; Mannucci et al. 1998). By using a geostationary satellite (as opposed to non-geostationary), variations in ionospheric observations can be more accurately attributed to fluctuations of the ionosphere rather than to movement of the satellite. This potentially enables a detailed analysis of the temporal variation of a section of the ionosphere (Kunitsyn et al. 2015).

Here, we demonstrate a technique which allows a TEC time series to be derived using the single frequency signals sent through the satellite-based augmentation system (SBAS) from geostationary satellites to ground-based receivers. Recently, studies such as Hein et al, 2016 (Hein et al. 2016) have begun to investigate the use of single frequency signal delays from non-geostationary satellites to estimate TEC. Single frequency receivers are less expensive than dual frequency receivers, and are thus a preferable data source (Hein et al. 2016). Our approach to TEC derivation uses single frequency signals from geostationary satellites, but for the first time this uses the propagation characteristics of the carrier phase advance, and the code delay of signals from the Global Navigation Satellite System (GNSS). Several geostationary satellites transmit GNSS signals for SBAS, including the European Geostationary Overlay System (EGNOS) and the Wide Area Augmentation System (WAAS). These signals are received by several ground-based GNSS receivers on a fixed global network.

This chapter demonstrates the technique. Validation is performed via correlation analysis with ionosonde TEC and by direct comparison with both ionosonde measurements of foF2, the peak plasma frequency in the F region, and ionosonde

estimates of TEC over a year. In section 5.2 the technique is explained. Section 5.3 describes the sources of GPS receiver and ionosonde data used in this chapter. In section 5.4 the existence of clock drift is discussed. Section 5.5 contains an initial evaluation of the technique, comparing daily profiles from three receivers and daily profiles from a nearby ionosonde. The initial data checks performed prior to more thorough validation are also discussed. The method is further validated using a cross-correlation analysis in sections 5.5 and 5.6, using pairs of GPS receivers in section 5.6, and GPS receivers to ionosonde TEC in section 5.7. Section 5.8 provides a brief discussion and concluding statements.

5.2 Introduction of the technique

5.2.1 Method

Geostationary satellites are used to relay information for the GNSS satellite-based augmentation system (SBAS). These signals transmit on the same frequencies as the standard GPS L1 signal, with the geostationary satellites relaying a signal uplinked from a ground location. These signals will experience a phase advance and an excess group delay that is dependent upon the state of the ionosphere. The pseudorange (or perceived range) of a GPS signal is related to the ionospheric delay as shown in Equation 5.1 (Mannucci et al. 1999; Davies 1990; Hargreaves 1992; Sardon et al. 1994).

$$P_1 = \rho + d_{tropo} + \frac{40.3 \times I}{f_1^2} + c(\tau_1^r - \tau_1^s) \qquad \textit{Equation 5.1}$$

Here, P_1 represents the GPS pseudorange (in m), ρ is the real satellite to ground distance (in m), d_{tropo} is the distance bias caused by the signal delay originating in the troposphere (in m), I is the TEC along the signal path (in electrons per m^2), f_l is the signal frequency (in Hz), c is the speed of light in a vacuum, and τ_1^r and τ_1^s represent dispersive delays caused by the hardware of the receiver and satellite respectively (in s) of the receiver and satellite respectively. These component biases for the pseudorange delay include satellite and receiver clock errors, satellite and receiver hardware delays, multipath and measurement noise. The units of the constant 40.3 are m^3s^{-2}.

The carrier phase range, L_1, (in m) can be expressed as shown in Equation 5.2 (Mannucci et al. 1999; Davies 1990; Sardon et al. 1994).

$$L_1 = \rho + d_{tropo} - \frac{40.3 \times I}{f_1^2} - \lambda_1 n_1 + c(\varepsilon_1^r - \varepsilon_1^s) \qquad \textit{Equation 5.2}$$

Here, λ_1 is the carrier wavelength (in m), n_1 represents the associated biases of the receiver and satellite (Sardon et al. 1994), ε_1^r and ε_1^s are dispersive hardware

delays from the receiver and satellite respectively, and other variables are as defined previously. These component biases for the carrier phases include an integer ambiguity term that represents number of phase cycle, satellite and receiver clock errors, satellite and receiver hardware delays, multipath and measurement noise. In Leick (2004) the clock biases are independent for each component, but here they have been combined to follow Mannucci et al. (1999). The pseudorange and phase range can be differenced to reveal the excess ionospheric path. This ionospheric path relates directly to the relative TEC:

$$P_1 - L_1 = 2\frac{40.3 \times I}{f_1^2} + \lambda_1 n_1 + c(\tau_1^r - \tau_1^s) - c(\varepsilon_1^r - \varepsilon_1^s)\,. \quad \textit{Equation 5.3}$$

Rearranging Equation 5.3 gives Equation 5.4.

$$I = \frac{f_1^2}{2 \times 40.3} \times (P_1 - L_1 - \lambda_1 n_1 - c(\tau_1^r - \tau_1^s) + c(\varepsilon_1^r - \varepsilon_1^s)) \quad \textit{Equation 5.4}$$

The terms $\tau_1^r, \tau_1^s, \varepsilon_1^r, \varepsilon_1^s$ and n_1 in Equation 5.4 cause a constant offset in TEC that does not vary with time. As geostationary satellites used here are at a fixed height multipath effects will remain constant. Therefore,

$$I_{rel} = \frac{(P_1 - L_1) \times f_1^2}{2 \times 40.3}\,. \quad \textit{Equation 5.5}$$

I_{rel} is an uncalibrated measurement of the absolute TEC, known as the relative TEC (in electrons m^{-2}), where 1 TECU is equivalent to 10^{16} electrons m^{-2} (Mannucci et al. 1998).

5.2.2 Demonstration of the technique

Figure 5.1 shows a 24-hour time series of relative TEC created using the method with a terrestrial receiver located in San Fernando, Spain. The time series created by the technique resembles the expected diurnal TEC time series. Sunrise and sunset at ground level are marked with orange lines. Values rise after local sunrise, remain elevated through the day and then fall after local sunset. As the ionosphere is at an altitude of 80 – 1000 km, the times at which solar driven ionisation will start and end will be slightly offset from the sunset and sunrise times at the surface.

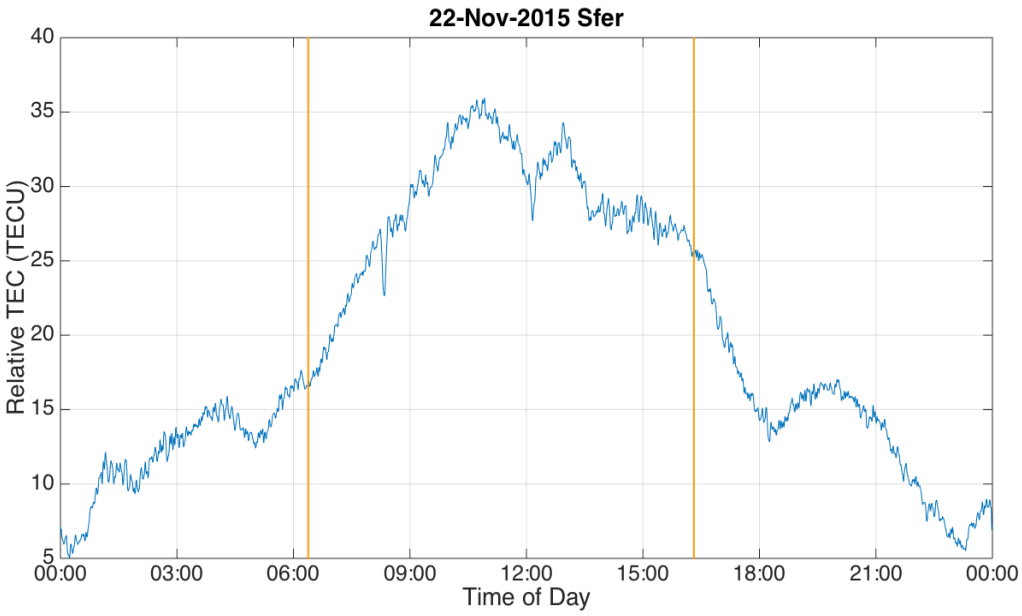

Figure 5.1: Time series of relative TEC derived using the single frequency technique at the receiver in San Fernando, Spain. Orange lines represent sunrise and sunset at ground level.

To assess whether the time series generated by the technique are plausible, a visual comparison is made with independent observations of the F2 region critical frequency (foF2) made by the Roquetes ionosonde (station code EB040) in northeast Spain. The time series for the same day can be seen in Figure 5.2.

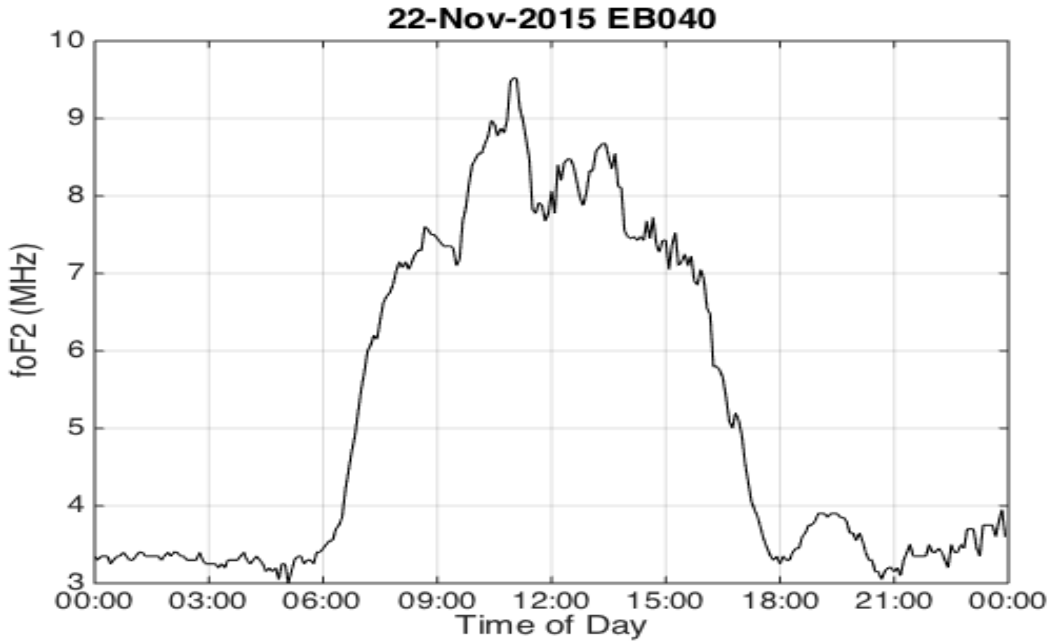

Figure 5.2: Time series of foF2 measurements from the ionosonde in Roquetes, Spain.

Figure 5.2 shows good agreement with the GPS time series in Figure 5.1. The plots show a similar shape, with a dual peak arguably present in both and a third peak noticeable after sunset. This suggests that the technique is producing sensible results that reflect reality. The foF2 value is related to the peak ionospheric electron density rather than the total electron content, and therefore the shape of the two time series will not be completely identical. A more thorough validation of the technique will follow in subsequent sections.

5.3 Validation data sources

5.3.1 GPS receiver data

To validate the technique data from three ground-based receivers capable of receiving geostationary signals are used. Two of these receivers are located in Germany, one in Heligoland (54.10°N, 7.53°E) and the other in Huegelheim (47.50°N, 7.35°E). The third receiver is located in San Fernando in Spain (36.28°N, 6.12°W). These receivers will be referred to as Helg, Hueg and Sfer respectively throughout the study. One of the GPS receivers (Helg) is part of the EUREF Permanent GNSS Network, whilst the other two (Hueg and Sfer) are part of the International GNSS Service (IGS). The sampling rate of the GPS TEC data is 30 seconds, and the data were evaluated using the equations in Section 5.2. GPS data were provided by the EUREF Permanent GNSS Network (Bruyninx et al. 2012) and The International GNSS Service (IGS) (Dow et al. 2009).

The satellite from which signals were sent to the ground receivers in this research is the SES-5 (or Sirius 5) geostationary satellite (PRN 136), positioned at 5° East.

5.3.2 Ionosonde data

Ionosonde data were identified as a source of ionospheric observations that were independent from the satellite derived TEC and could thus be used for validation. Ionosondes are active instruments that transmit and receive HF radio signals. By repeatedly reflecting radio waves off the ionosphere and analysing the return signal, ionosondes can obtain vertical time series of the plasma frequency and hence derive values of electron density. Ionosonde TEC is a combination of measured and modelled values. The electron density up to the height of peak plasma frequency is measured by the ionosonde, and from this point up to a height of 1000 km the values are modelled using the observed values (Huang & Reinisch 2001; McKinnell et al. 2007; Reinisch & Huang 2001). The TEC value of a column through the whole ionosphere is then found by adding the integral of electron density through the measured section to the integral of electron density through the modelled section (Huang & Reinisch 2001; McKinnell et al. 2007). For the ionosonde data used here the ionosphere above the peak is modelled using a Chapman profile with a constant scale height.

The three GPS receivers were selected from a network of receivers across Europe. The geometrical configuration of the satellite to receiver paths are such that they can be compared to the ionosonde in Roquetes, Spain (40.80°N, 0.50°E) for validation. Ionosonde data used in this chapter were obtained from the Digital Ionogram Data Base (DIDbase) (Reinisch & Galkin 2011). The Roquetes ionosonde is also referred to by the station code, EB040. The locations of the receivers and ionosondes are shown on the map in Figure 5.3, along with the satellite and corresponding measurement paths between the receiver and the geostationary satellite. The sections of the measurement paths that intersect the ionosphere between 80 and 400 km altitude are indicated by the green lines in Figure 5.3 by a solid green line, and the black dashed line indicates the ionospheric intersect between 80 and 1000km.

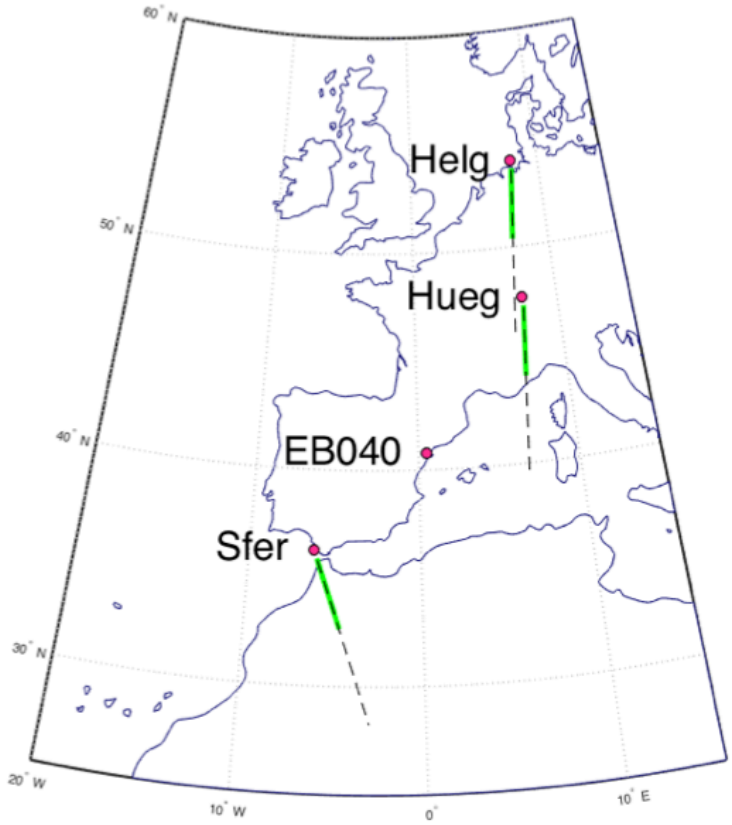

Figure 5.3: Locations of GPS receivers (Helg, Hueg and Sfer) and Roquetes ionosonde (EB04). The section of the paths between the satellite (SES-5) and 80 and 400 km altitude are indicated with green lines and the section path from 80 to 1000 km with black dashed lines.

5.4 The impact of clock drift

Errors in single frequency GPS TEC derivation can arise from 'clock drift', which is the drift in the inbuilt clock of the terrestrial receiver (Mannucci et al. 1999). Of the three receivers used in this study, one has an oscillator which is

linked to an atomic clock and thus should be minimally vulnerable to this issue, but clock drift must be accounted for with the other two. The Helg and Hueg receivers both have oscillators which do not have an atomic clock, whilst the Sfer receiver has an oscillator which does have an atomic clock. Noticeable clock drift was observed in the 24-hour time series plots derived from the Helg and Hueg receivers, but was far less noticeable in profiles derived from Sfer.

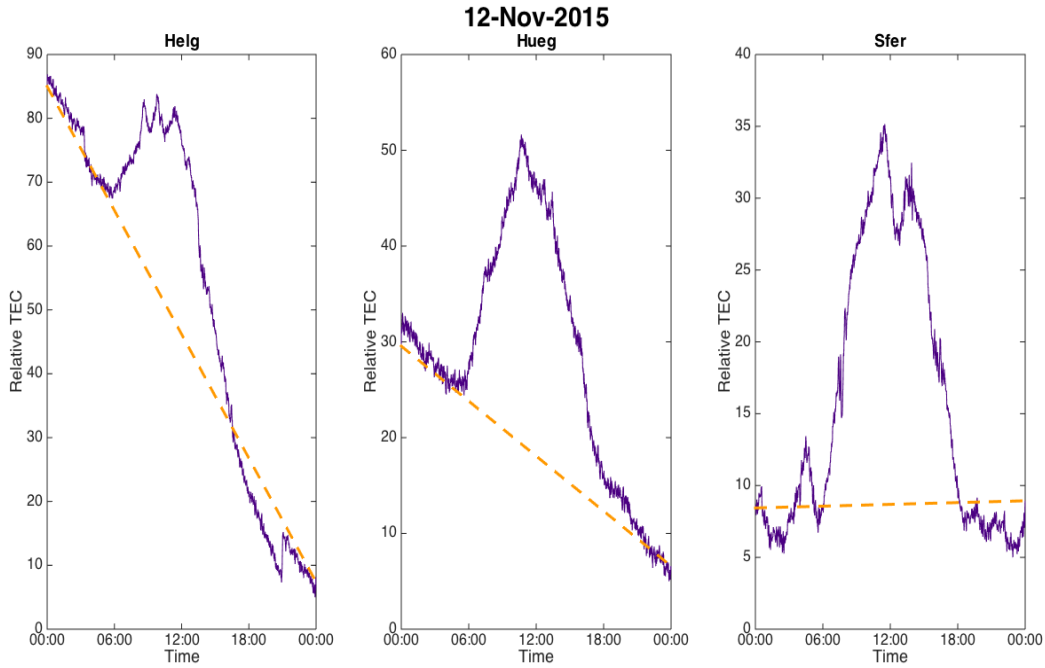

Figure 5.4: Pre-detrended derived daily relative TEC profiles from the Sfer, Helg and Hueg receivers.

Figure 5.4 shows the clock drift observed in the GPS derived daily TEC time series for each of the three receivers before detrending. This results in a noticeable diagonal tilt over a 24-hour time series for two of the receivers. This was corrected for using a linear detrend. It can be seen that there is little noticeable drift in the profile from the Sfer receiver, which is linked to an atomic clock. However, the profiles from both Helg and Hueg, which are not linked to atomic clocks, show noticeable clock drift. Investigation into this drift suggested that a drift of approximately 43 ns and 15 ns was observed over a 24-hour period for these two receivers, assuming that the TEC is not changing significantly day-to-day. Hein et al (Hein et al. 2016) also experienced issues with clock drift in their study into single frequency delay TEC derivations from GPS satellites.

5.5 Initial evaluation of the technique

5.5.1 Technique demonstration

For each of the three receivers diurnal TEC time series were calculated for each day in 2015 using the technique. Figure 5.5 shows the daily TEC time series for example days generated by the technique, for all three GPS receivers and additionally foF2 from the Roquetes ionosonde. foF2 is a directly measured

value that corresponds to the maximum electron density in the ionosphere. Ionosondes are also capable of producing TEC values, as shown, but these contain a modelled component as the region of the ionosphere above the peak electron density cannot be observed by an ionosonde. The Helg and Hueg receivers are located to the north east of the ionosonde, whilst the Sfer receiver is located south west of the ionosonde.

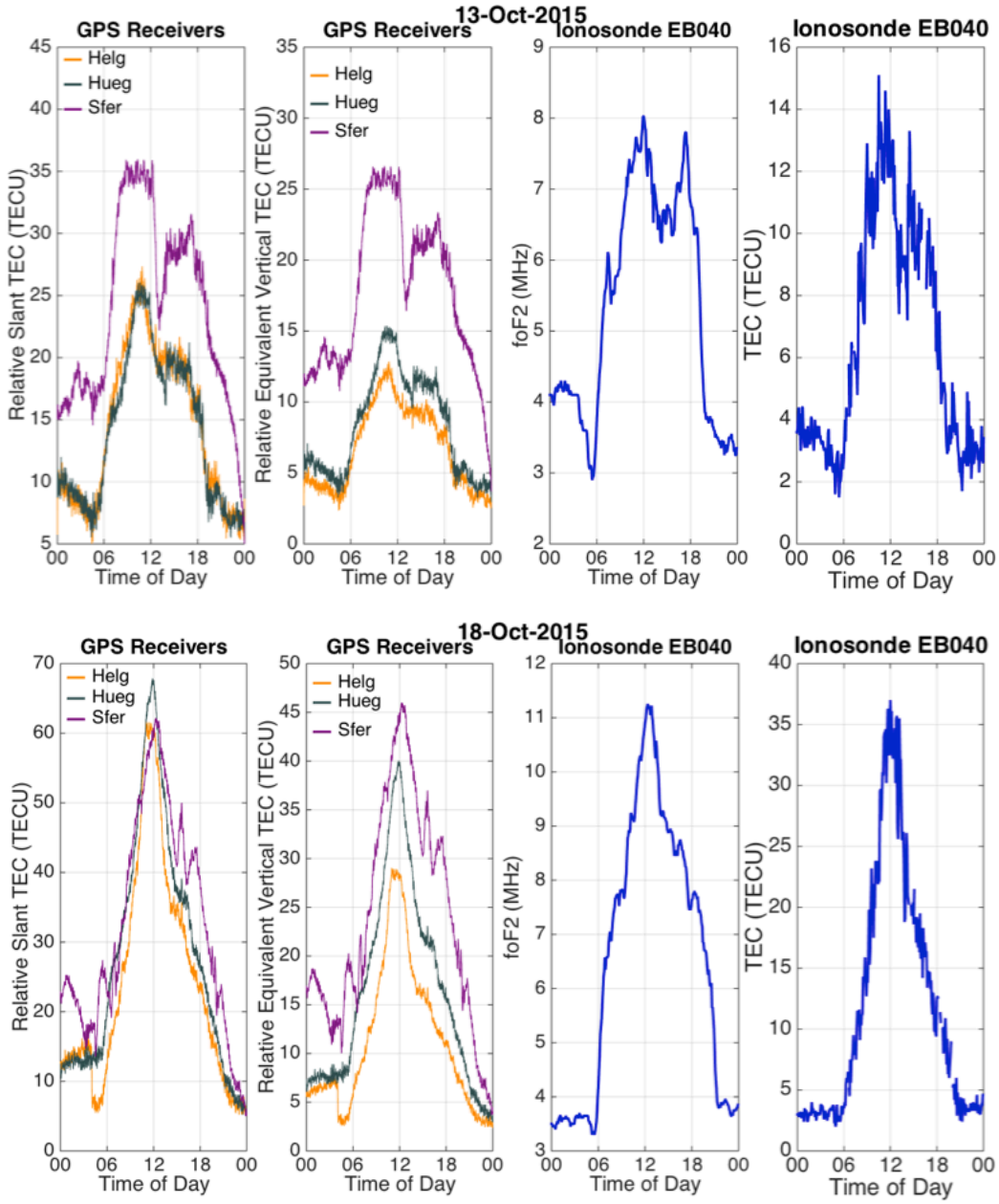

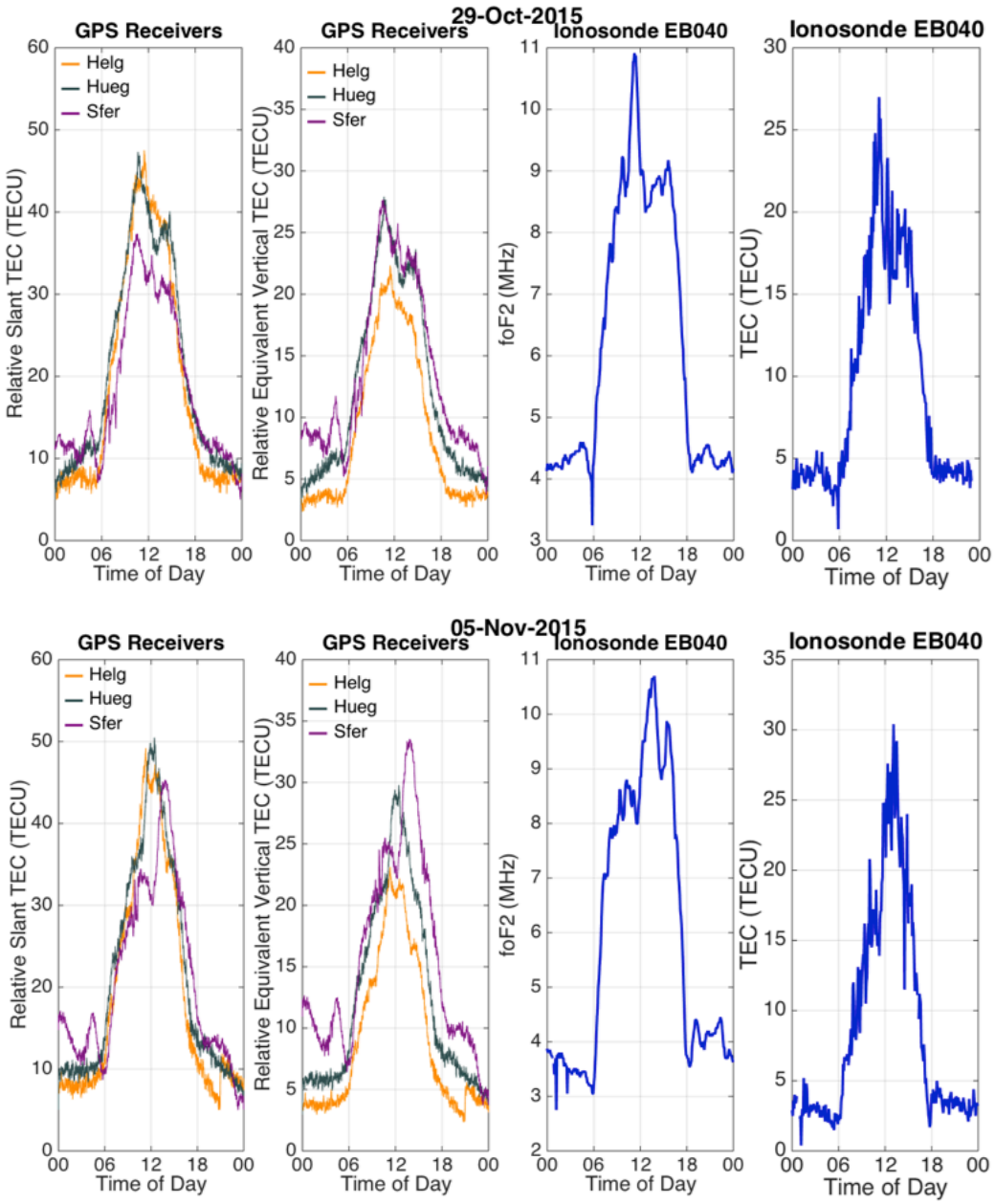

Figure 5.5: Relative TEC time series derived using the single frequency technique at the Helg, Hueg and Sfer ground receivers and observed foF2 time series and derived TEC from the Roquetes ionosonde from 13, 18, 29 October and 5 November 2015.

These plots indicate a good level of agreement in the diurnal variations and in some shorter-term variations between the three ground receivers and between the receivers and the ionosonde. Note that the ionosonde produces an estimate of vertical TEC in the ionosphere, whereas the GPS GEO produces slant TEC through the ionosphere and the plasmasphere. The plasmasphere should account for a few TECu. Using a geometrical correction the slant to equivalent vertical TEC correction factor (Leitinger et al. 1975) for the ionosphere is 0.47 (Helg),

0.59 (Heug) and 0.74 (Sfer) for the satellite elevations. Taking these into account the magnitude of the diurnal TEC variations observed with the GPS GEO method are comparable to those from the ionosonde. It should also be noted that the conversion factor from slant to equivalent vertical TEC for a geostationary satellite viewed from a fixed receiver is a fixed value and hence will not affect the correlation results presented later in this chapter.

This visual inspection suggests that the technique performs well for all four GPS-GEO examples. It should be emphasised that only the relative TEC changes should be considered here. The offsets seen between the relative TEC values derived from the three receivers are caused by differences in receiver hardware ($\tau_1^r, \varepsilon_1^r$ and n_1 in Equation 5.4) and the minimum of the GPS-GEO value each day has been set to a value of 5 TECu for plotting purposes.

5.5.2 Preliminary inspection of relative TEC time series

For quality control purposes all time series generated using the single frequency technique were visually inspected. Those that were judged unrealistic because they were either contaminated by substantial losses of lock or because they were incomplete days were discarded to avoid contamination of the data set used for validation. A day was discarded if it met any of the following criteria:

(1) Diurnal TEC pattern absent due to phase jumps, as in Figure 5.6 panels (c) and (d)
(2) More than 15% of data missing
(3) Large discontinuities in TEC time series, as in Figure 5.6 panel (b)
(4) One constant TEC value over a 24-hour period (i.e. no data)

Figure 5.6 shows examples of time series derived using the single frequency technique at the Helg receiver for days that were discarded.

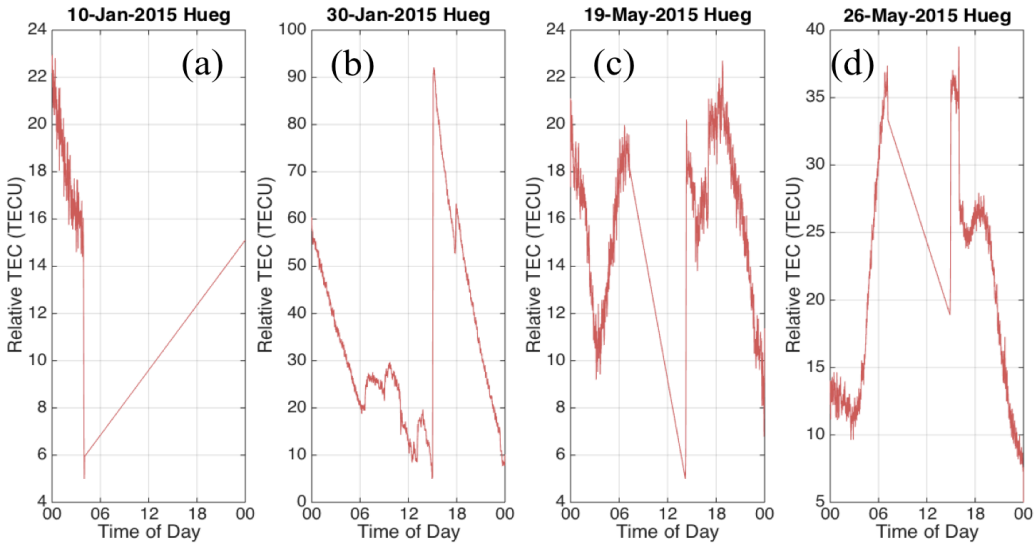

Figure 5.6: Examples of unrealistic time series derived using the single frequency technique, which were discarded to prevent contamination of the verification data set.

From Figure 5.6 it can be seen that time series often become unrealistic if the receiver loses lock (where a near-instantaneous large jump in y-axis value occurs) at any point in the day. Lock is lost when the terrestrial receiver cannot detect the signal from the satellite, and can be near instantaneous or last for a few minutes. Lock can be lost in the presence of ionospheric scintillation, or when the amplitude of the signal changes (Leick 2004). The number of days in 2015 that were discarded for each station are listed in Table 5.1. It is acknowledged that the number of days discarded is high, but considered acceptable for this proof of concept.

Table 5.1: Days discarded for each GPS receiver for the year 2015.

Station	Number of Days Discarded
Helg	126 (35%)
Hueg	115 (32%)
Sfer	241 (66%)

5.6 Cross-correlation analysis

5.6.1 Cross-correlation analysis between TEC time series

The agreement between time series obtained from three GPS receivers was assessed using a correlation analysis over a year's worth of data for the year 2015. The analysis is similar to that described in Chapter 4, for each combination of receivers, a 24-hour TEC time series from one receiver was correlated with the 24-hour time series from the second receiver for the same day. The two time series were interpolated from 30 second onto a 1-minute time scale, then overlaid, and the correlation was calculated to find a measure of the

agreement between them. Next, one time series was fixed and the other was shifted in 1-minute time steps. A correlation value was calculated between the fixed and shifted time series after each shift for shifts extending up to 180 minutes. The percentage of days each correlation value was measured for each shift was then computed, and represented with a colour scale.

The TEC time series for each GPS receiver were correlated with the time series derived for each of the other two receivers, with days discarded as explained in Section 4.2. Table 5.2 lists the number of days included in each receiver pair analysis after invalid time series were discarded.

Table 5.2: Days included in each GPS pair analysis.

Station One	Station Two	Number of Days Included
Sfer	**Helg**	101
Sfer	**Hueg**	112
Helg	**Hueg**	211

Figure 5.7 shows the results from the correlation analysis for each pair of GPS receivers. In these correlation plots each pixel represents the percentage of data recorded, with lag on the x-axis and correlations on the y-axis. A year's worth of data is displayed in each plot, with each day providing a single correlation value for each lag value. The majority of the correlations calculated were between 0.8 and 0.9. Anti-correlations were negligible in number and thus only positive correlations are shown.

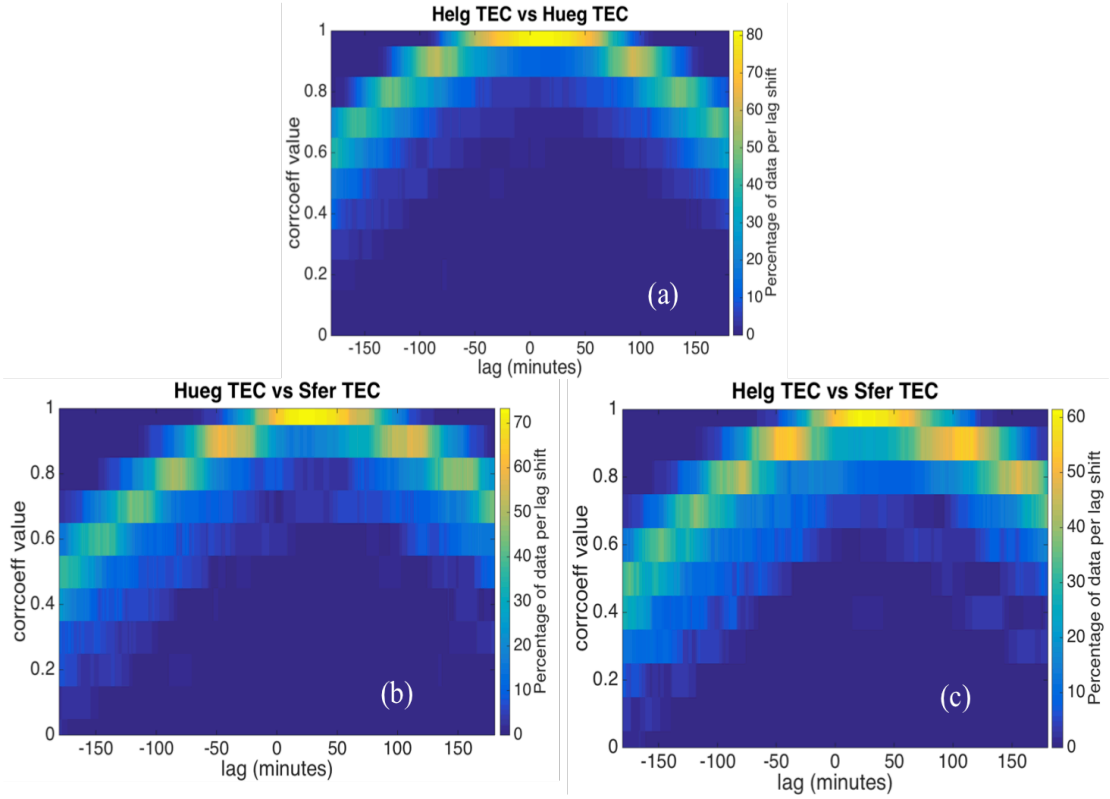

Figure 5.7: Correlation analysis of daily GPS derived relative TEC time series from pairs of GPS receivers, (a) Helg vs. Hueg, (b) Hueg vs. Sfer and (c) Helg vs. Sfer, for all usable days in 2015.

High correlations are seen between all pairs of GPS stations, peaking around a lag of zero (when both time series are overlaid for the same time). Correlations are lower at lags moving away from zero. This is consistent with expectations, as at these lags there is a significant time difference between the two time series being correlated. Figure 5.7 shows that the correlations are higher between Helg and Hueg (panel a) than for either of the correlation pairs involving Sfer (panels b and c). This is to be expected, as the Sfer receiver is geographically further away from both Helg and Hueg than they are from each other. This means that correlations between Sfer and other stations will be high for a shorter time, and lower at large lags.

It can be seen in Figure 5.7 that there is a slight offset from zero for the lag at which peak correlation values are attained, most noticeably for correlations involving Sfer. As electron density in the ionosphere is dependent upon solar radiation, the time of day at which peak density occurs will correspond with local solar noon time at the observing receiver location. Consequently, the time series will correlate best when the local solar noon of each time series are aligned, which as these data are in UTC will cause an offset. Peak values are reached at a lag close to corresponding local time difference, suggesting the offset is mostly due to local time difference.

5.6.2 Cross-correlations with diurnal cycle removed

The diurnal cycle was removed from the 24-hour time series to investigate its impact on correlation, following the approach used in Chapter 4. A smoothed version of each day's time series was subtracted from the raw data to leave perturbations around the diurnal cycle for each day. The correlation analysis was then repeated for each pair of receivers using only the perturbations outside of the diurnal cycle. Figure 5.8 shows the correlation results for each pair of GPS receivers. Anti-correlations were again negligible in number.

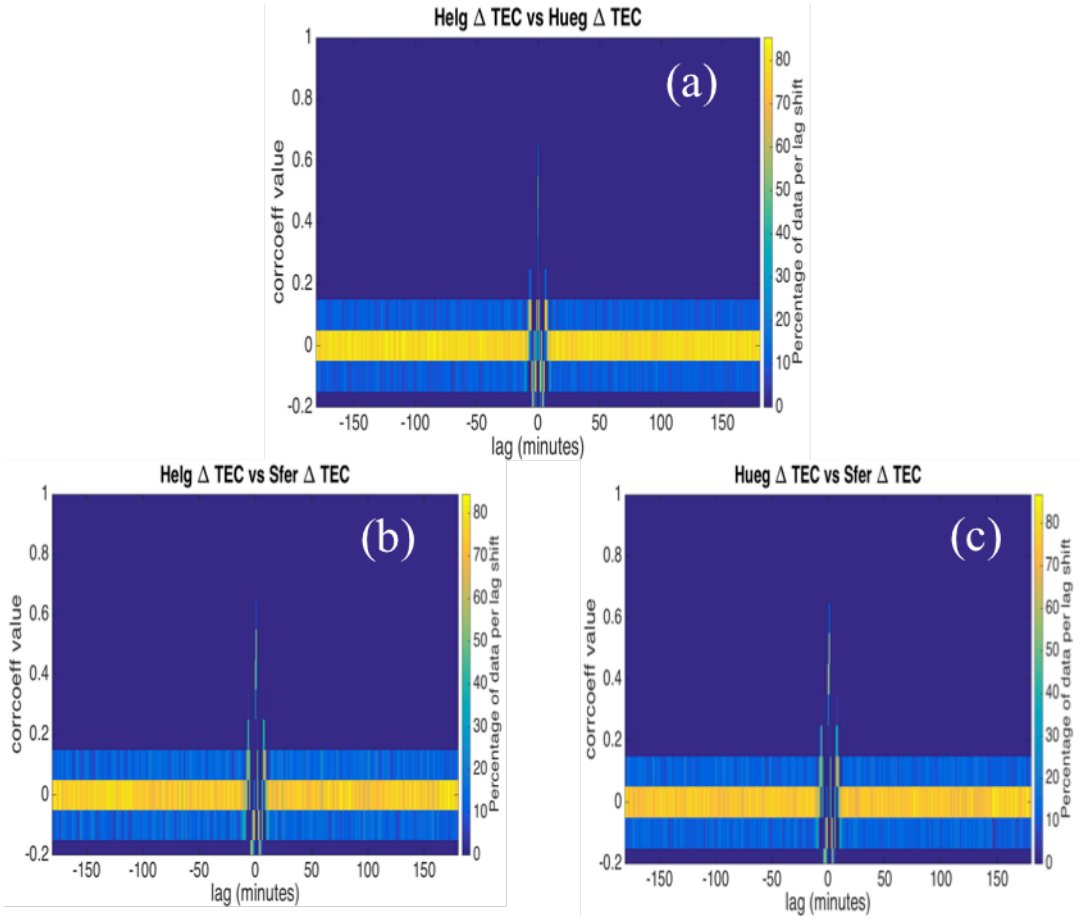

Figure 5.8: Daily correlations between relative TEC from GPS receivers calculated after diurnal cycle removed for all usable days in 2015.

We see that most of the correlations for data with the diurnal cycle removed are centred strongly around zero. This suggests that the diurnal cycle was responsible for almost all of the high correlations seen in Figure 5.7.

5.7 Cross-correlations between ionosonde TEC and GPS TEC

Daily time series of GPS TEC from the three receivers were each correlated with daily time series of ionosonde TEC from the Roquetes ionosonde. Ionosonde TEC values were used rather than foF2 so correlations were between as similar

parameters as possible. However it is also to be noted that TEC is a derived quantity from the ionosonde. Correlations were found for the year 2015 using the same process as described in section 5.1, but with the GPS data downsampled onto a 5-minute timescale to match the ionosonde sampling rate. The results are shown in Figure 5.9. Only positive correlations are shown, as anti-correlations were negligible in number.

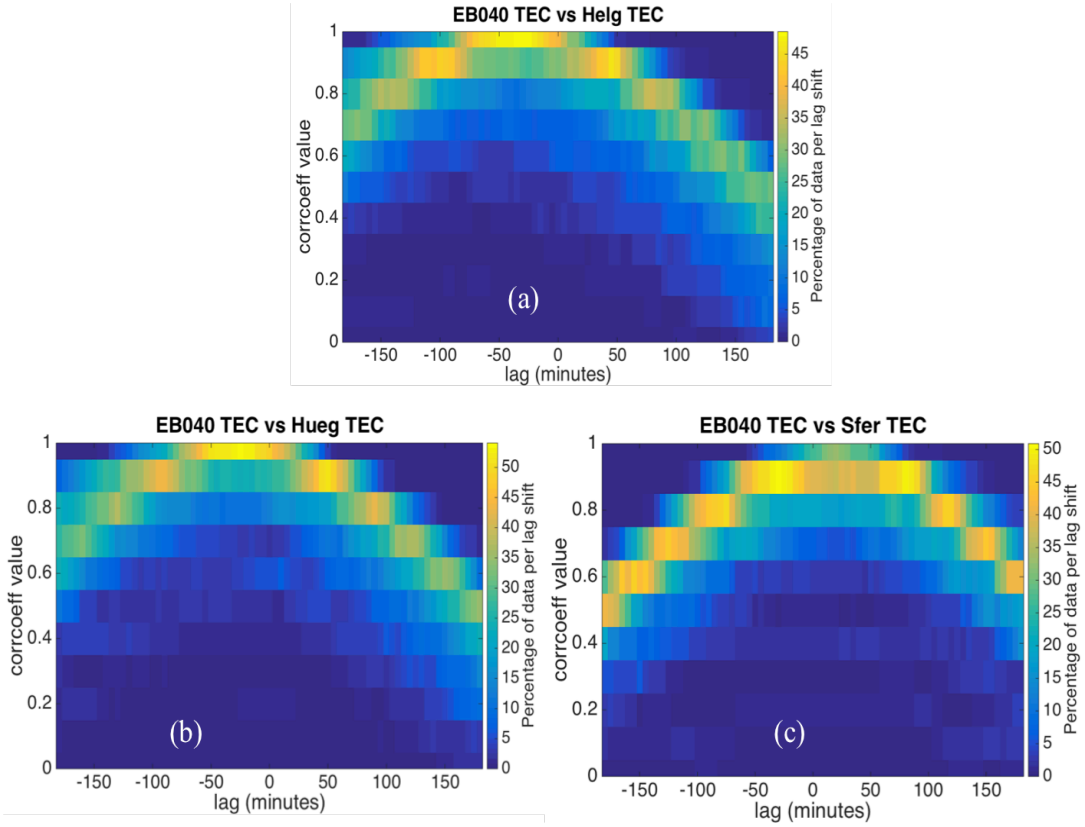

Figure 5.9: Daily correlations between relative TEC from the three GPS receivers and the Roquetes ionosonde, (a) EB040 vs. Helg, (b) EB040 vs. Hueg and (c) EB040 vs. Sfer, for all usable days in 2015.

Correlations are high between the ionosonde and all three receivers, however peak correlations are slightly lower between the ionosonde and Sfer (panel c) than for the other two receivers. Whilst Sfer is the closest of the three receivers to the ionosonde at the Earth's surface, the satellite to receiver measurement paths for Helg and Heug are closer to the ionosonde's measurement path in the ionosphere than for Sfer (see Figure 5.3).

It can be seen from Figure 5.9 that the peak correlation is offset from zero lag for all three receivers. This shift implies that the ionosonde time series correlates best with GPS time series from earlier or later times (plots imply a shift of 30-50 minutes). This shift is probably the result of the movement of the sun as the lag delay matches up approximately with the local time difference between the receivers and the ionosonde. Sfer (panel c) also shows a broader temporal peak

in lag. The high correlations seen in all three plots imply a consistent, good agreement between the ionosonde observed profiles and the GPS derived profiles over a year.

5.8 Chapter 5 discussion and conclusions

A technique has been demonstrated that allows daily relative TEC time series to be derived using a single frequency signal transmitted from a geostationary satellite to a ground-based receiver. Initial analysis through visual inspection of the slant TEC shows that the time series produced similar diurnal variations at three ground receivers in Europe. Some of the short-term features were also similar. Statistical correlations were calculated between pairs of 24-hour TEC time series for the same day from different ground receivers. The results show strong agreement (correlations above 0.9), with shifts in the lag at which peak correlation is reached occurring mostly due to local time difference. Analysis between daily time series generated by the GPS GEO technique and daily time series of TEC observed by the Roquetes ionosonde showed high correlations consistently over a year. A shift in the time at which peak correlations were seen was observed due to local time differences. This shows the usefulness of the correlation analysis introduced in Chapter 4 for evaluating the quality of new ionosphere observations.

Further refinement of the technique is needed to automatically and reliably reject discontinuous or missing data streams and in some cases to resolve issues by fixing cycle slips. Although many GPS 24-hour time series were discarded using criteria explained in section 6.4.2, it is possible that sections of these time series could be recoverable. It is possible that if a 24-hour time series is rejected due to a phase jump near the start of the day, several hours of data collected later in the day could still be useable. The same principle applies for the 15% missing data caveat. If hypothetically all the missing data were consecutive observations, the remaining 85% of the time series could be valuable. Development of a technique for more skillfully discarding unusable time series whilst extracting usable portions could improve the operational usefulness of the technique.

A potential source of error in the technique arises from clock drift. One of the three receivers used in this study was linked to an atomic clock, but the other two were not. The receivers lacking an atomic clock link experienced a timing drift of tens of nanoseconds over a 24-hour period. This drift was noticeable in the raw derived time series, but a linear detrending these results allowed the clock drift to be removed and final time series to be produced. Higher order terms in clock drift would have an effect on the correlations, however by visual inspection of drift in Figure 5.4 it appears that clock drift is not causing a significant deterioration in end results. A possible extension of this project would be to investigate clock drift further across different GPS receiver types following this

study to fully assess its impact and identify potential mitigations.

The technique offers significant advantages as a data source for ionospheric mapping because it provides a time series of relative TEC from fixed-elevation and azimuth paths through the ionosphere. It is anticipated that future research will quantify the benefit of this data for ionospheric data assimilation. Validation of the single frequency GPS TEC derivation technique has shown it to routinely produce realistic time series of TEC. The time series are also consistent between receivers and correlate well with ionosonde observations of both foF2 and TEC. In Chapter 6 this now verified technique will be used to investigate a geomagnetic storm.

Chapter 6

Investigation into the ionospheric response to geomagnetic storm conditions

Abstract

This chapter investigates how the correlation relationships discovered in Chapter 5, and the Global Positioning System (GPS) total electron content (TEC) derivation technique introduced in Chapter 6, are impacted by geomagnetically disturbed conditions. Firstly, the impact of geomagnetic storm conditions on the cross-correlation of ionospheric parameters was investigated. The amount of correlation between foF2 and hmF2 during multiple storms took on a range of values, but often the correlations remained similar to those for all conditions (reported in Chapter 4). The time of day at which the storm occurred also gave no consistent cross-correlation response, however storms covering both dawn and dusk reduced the strength of the anti-correlation at positive lags. Ionosonde foF2 and GPS derived TEC (GPS TEC) remained strongly correlated over multiple storm days. The storm days caused a range of responses to the strength of the anti-correlation between hmF2 and GPS TEC, with some storms strengthening and others weakening the relationship. The storm causing the greatest weakening of anti-correlations caused the cross-correlations between the two parameters at some lags to fall above -0.5, and for the parameters to therefore no longer be considered correlated. Correlations between pairs of GPS TEC measured by receivers at different locations remained strong, peaking above 0.8 on all disturbed days. The analysis suggests good consistency and reliability of the new technique in strong storm conditions, however as the data set available was small this conclusion cannot be stated with total confidence. Secondly the response to the geomagnetic storm observed on December 20th 2015 was investigated as a case study. On this day the strength of the anti-correlation between foF2 and hmF2 was significantly reduced at positive lags. foF2 and GPS TEC however remained strongly correlated, peaking above 0.8, and hmF2 and GPS TEC were strongly anti-correlated. Correlations between pairs of GPS receivers on the storm day also remained high. Comparisons between the new technique and model data showed a good agreement. This suggests the new technique remains reliable in all geomagnetic conditions.

6.1 Introduction

6.1.1 The storm-time ionosphere

The ionosphere is sensitive to geomagnetic storm activity. A divergence from typical solar activity can result in an altered solar wind stream arriving at Earth,

usually faster moving and with a higher particle density, and can cause disturbances in the planet's magnetic field (Ratcliffe 1972). This can influence the ionosphere due to the coupling between the ionosphere, the surrounding neutral atmosphere, and the magnetosphere (Mannucci et al. 2005). Such events are usually referred to as geomagnetic storms. These storms can affect various ionospheric characteristics, including the behaviour of the neutral winds, the movement of ionospheric electric fields, and the composition of the neutral atmosphere (Forbes et al. 2000). These changes can have adverse effects for technology that makes use of radio waves traveling through the ionosphere, such as the Global Positioning System (GPS), which can experience temporary fading in signals and frequent changes in signal phase due to ionospheric storms (Mitchell et al., 2005).

The storm-time ionosphere has been of scientific interest for some time and has been frequently investigated. As far back as the 1950s positive and negative phases in ionospheric responses to geomagnetic storms were identified by Sato 1957 and Matsushita 1959 (Matsushita 1959) (Mendillo 2006). Early ionospheric storm investigations predominantly relied upon data provided by ionosondes. However, almost immediately after the installation of artificial satellites capable of deriving ionospheric Total Electron Content (TEC) this method became popular for storm-time analysis (Mendillo 2006). Satellites became an even more useful tool for studying TEC when a technique coupling satellites with GPS receivers was developed, allowing a global network of TEC observations (Mendillo 2006). TEC is particularly useful for investigating ionospheric conditions during geomagnetic storms, TEC measurements are less vulnerable to storm related disruption than other forms of ionospheric observations including ionosondes (Mendillo 2006).

6.1.2 Chapter aims

The aim of this chapter is to investigate the relationship between ionospheric parameters under geomagnetically disturbed conditions, and to continue the validation of the new total electron content (TEC) derivation technique introduced and validated in Chapter 4. Specifically, this chapter aims to answer the following questions:

1. Do the correlation relationships identified in Chapter 4 hold in geomagnetically disturbed conditions?
2. Is the correlation response to geomagnetically disturbed conditions consistent over multiple storm days?
3. Does the new single frequency Global Positioning System (GPS) TEC derivation technique remain reliable and consistent in geomagnetic storm conditions?

Section 6.2 discusses the data sources for this chapter. Section 6.3 introduces the geomagnetically disturbed days. Section 6.4 investigates the cross-correlations

between ionospheric parameters in geomagnetically disturbed conditions. Section 6.5 takes a single storm a case study for more in depth analysis, and Section 6.6 provides concluding statements.

6.2 Data sources used

The data and techniques used in this chapter are as listed in Chapters 4 and 5. Ionosondes were used to acquire values of the F2 region critical frequency, known as foF2 and measured in MHz, and the corresponding height, known as hmF2 and measured in km. Values of TEC used here are derived using the new technique explained and validated in Chapter 5. This technique analyses the variations in the pseudorange and carrier phase range of signals travelling between geostationary satellites and single frequency GPS ground receivers to give values of relative slant TEC. The phrase 'GPS TEC' in this chapter will always refer to relative slant TEC values derived using the new technique. As a reminder, the locations of the ionosonde (EB040) and GPS receivers (Helg, Hueg, Karl and Sfer) used in this chapter are shown in Figure 6.1.

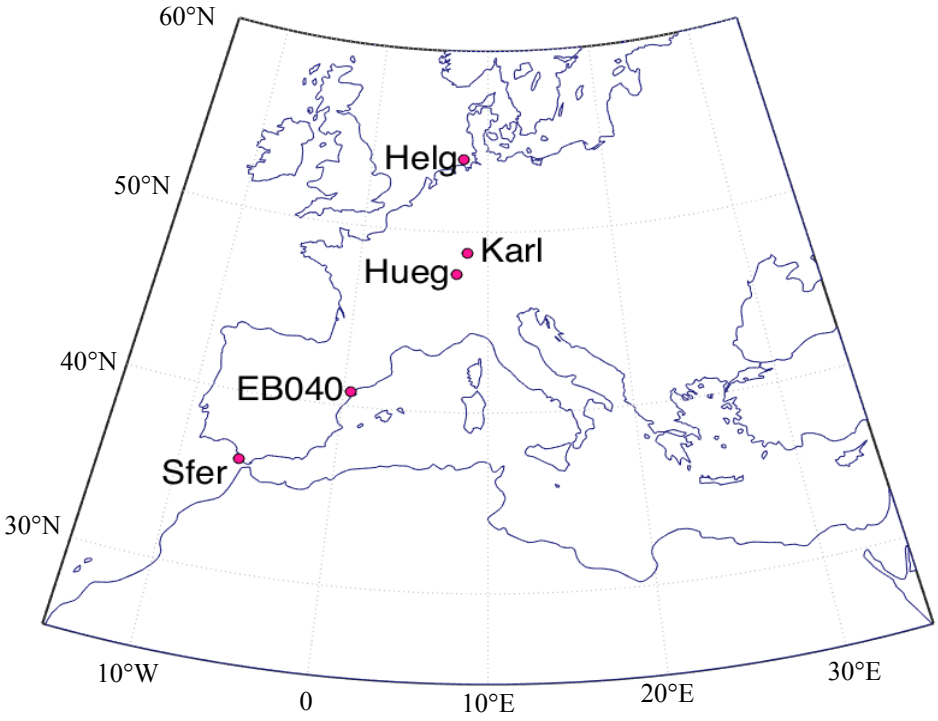

Figure 6.1: Locations of Ionosondes (EB040) and single frequency GPS receivers (Helg, Hueg, Karl and Sfer)

Full details on the locations of these data sources are listed in Section 5.2 of Chapter 5. Data from the GPS receiver Karl is used for the first time in this Chapter. This receiver is located at Karlsruhe, Germany with co-ordinates 49.00°N and 8.24°E. This receiver had insufficient data over a year to be included in the analysis in Chapter 5, however data were available for December

2015. It is hoped that adding an additional GPS receiver will help to counteract the small size of the GPS dataset used in this chapter, which is only the month of December 2015. Days from the GPS data were discarded as described in Chapter 5 section 5.4.2. The number of days included in subsequent analysis for the four GPS receivers are listed in Table 6.1.

Table 6.1: Number of useable 24-hour TEC time series generated by the new technique for December 2015.

Receiver	Number of Usable Days in December 2015
Helg	31
Hueg	31
Karl	30
Sfer	27

Cross-correlation analysis using only ionosonde data is completed using data from 6 Decembers (2010 – 2015), whilst cross-correlation analysis involving GPS derived TEC (both TEC with ionosonde parameters and TEC from pairs of receivers) uses only data from a single December, for the year 2015.

The K index is a measure of the amount of disturbance observed in the magnetic field over 3 hours, with values ranging from a minimum of 0 to a maximum of 9 (Hargreaves 1992). The Kp value is the average K value across the planet calculated using data from 13 stations around the world (Tascione 1994; McNamara 1991). K and Kp values range on a quasi-logarithmic scale from a value of 0, indicating the magnetic field is not disturbed, to a value of 9 which indicates a significant disturbance (McNamara 1991; Kelley 2009). K index data for storm identifications were provided by the Space Weather Prediction Centre (SWPC) online database archive (Space Weather Prediction Centre (SWPC) n.d.). K and Kp index observations are made every 3 hours, and hence there are 8 observations in each 24-hour period.

6.3 Identification of geomagnetically disturbed days

Days were classified as disturbed where K values were 5 or above for at least 3 of the 8 K measurements observed at either high latitudes, or across the planet. Table 6.2 lists days that were disturbed, and highlights in blue the measurements of 5 or above in the location (high latitude or planetary) at which 3 or more of these values were present. 13 Days were identified that met these criteria, all occurring in either 2014 or 2015.

Table 6.2: K indices of December storm days 2010 – 2015, blue values indicate

where the requirements for a day to be classified as disturbed were met (data from Space Weather Prediction Centre (SWPC), available at https://www.swpc.noaa.gov/products/planetary-k-index).

Date	Middle Latitude (Fredericksburg) K-indices	High Latitude (College) K-indices	Estimated Planetary K-indices
2014 12 07	4 2 2 3 4 4 4 3	4 3 3 6 7 6 5 3	5 3 3 3 5 4 4 4
2014 12 12	2 2 3 2 5 3 3 2	2 2 6 5 6 6 4 3	3 3 4 3 5 4 4 3
2014 12 15	1 2 2 3 3 3 2 3	1 2 5 5 6 4 3 1	2 3 3 3 3 3 3 3
2014 12 22	4 3 4 2 2 3 1 1	5 5 5 5 2 3 1 1	5 5 4 2 2 3 2 2
2014 12 29	1 2 2 3 3 4 3 4	1 2 3 5 6 6 3 4	2 3 2 3 4 5 4 5
2015 12 01	2 3 1 2 3 3 2 3	2 2 1 6 6 5 3 3	2 3 1 3 3 4 3 4
2015 12 05	1 2 4 4 2 3 3 2	0 0 5 5 5 5 3 2	2 2 4 4 3 4 4 3
2015 12 06	2 4 2 5 5 4 3 4	2 4 4 7 7 5 3 3	3 4 3 5 4 4 4 4
2015 12 10	2 4 3 4 2 3 3 4	2 4 5 5 6 4 4 2	3 5 4 3 3 3 4 4
2015 12 11	4 2 2 3 2 3 3 3	3 4 6 6 5 5 2 2	4 3 3 3 3 4 3 4
2015 12 20	3 5 4 4 4 5 4 5	2 6 6 7 7 7 6 5	4 6 5 5 5 6 6 6
2015 12 21	5 5 4 4 2 2 2 2	3 6 6 7 5 3 2 2	6 6 5 4 3 3 2 3
2015 12 31	3 3 4 4 4 3 4 5	2 2 6 5 7 6 6 5	4 3 4 4 6 4 5 6

Table 6.1 shows that of the 13 storms that occurred in the month of December between 2010 and 2015 most only met the K index requirement at high latitudes. The final three storms on the 20th, 21st and 31st of December 2015 meet the requirement at both high latitudes and planet wide. The storm on December 20th is the strongest in the data set, with planetary Kp values of 5 or above for 8 out of 9 measurements. A disturbed ionosphere would be expected in all 13 days, and a stronger response might be expected for the strongest three storms. None of the storms have K indices of 5 or above for three observations at mid-latitudes. Ionosonde data for 11 December 2015 was missing from the data set, and this storm is consequently excluded from subsequent ionosonde analysis.

6.4 Influence of storm conditions on the cross-correlation of ionospheric parameters

In order to assess if the correlation relationships identified in Chapter 4 remained in geomagnetically disturbed conditions, the cross-correlation analysis was repeated for all available geomagnetically disturbed days in all Decembers.

6.4.1 Cross-correlations between ionosonde parameters

Cross-correlations were calculated between ionospheric parameters as explained in Chapter 4 Section 4.4. Correlations were found using 24-hour time series with lags of ±180 minutes around time 0. Chapter 4 Section 4.5 showed a strong anti-correlation between foF2 and hmF2 over a 24-hour period (see Figure 4.10),

peaking at a cross-correlation of -0.8 and sustained for approximately 100 minutes. Figure 6.2 shows the cross-correlations between foF2 and hmF2 on multiple storm days and compares them with corresponding cross-correlations for all 6 Decembers. In Figure 6.2 panel (a) each pink line represents the correlations for a single storm day, and each patch the 5^{th} – 95^{th} percentiles calculated from a single December's data. It was expected that by using the 5^{th} and 95^{th} percentiles all storm data would have been excluded. If storm conditions are infrequent and extreme they would all fall outside the 5th and 95th percentiles. For comparison the statistical process was repeated using the maximum and minimum values as patch boundaries instead of percentiles. Figure 6.2 (b) compares the correlations from the storm days to the maximum and minimum values for 6 Decembers. Each black line in both panels represents the median correlations for a single December.

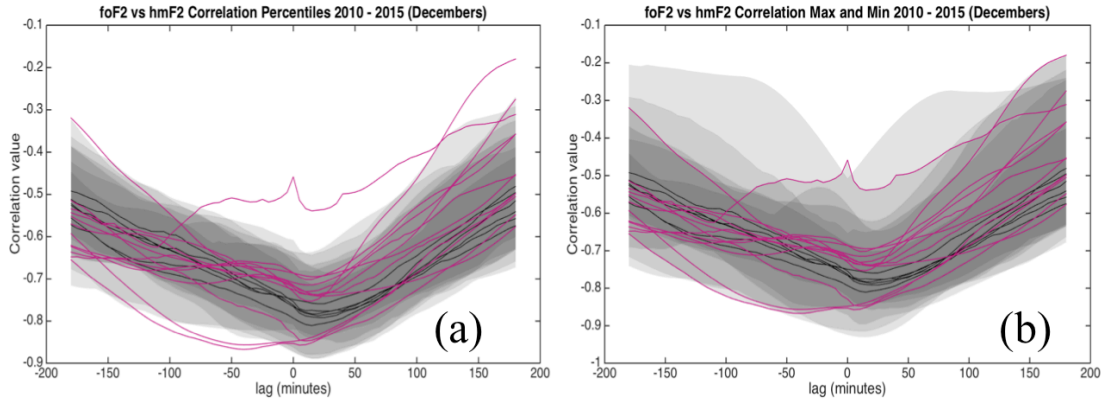

Figure 6.2: Cross-correlation values between foF2 and hmF2 observed at the EB040 ionosonde for each December with pink lines depicts storm day correlations and patches indicating (a) 5^{th} and 95^{th} percentiles and (b) maximum and minimum for each December. Negative lag indicates that foF2 leads and hmF2 lags.

Figure 6.2 shows that storm day correlations cover a range of values, and there is no consistently unusual behaviour for storm-time conditions. Figure 6.2 (a) shows that for several of the storms the correlations are similar to the medians and lie within the 5-95 percentile patches of most years. Three storm days are outside all the patches between lags of -100 and 0, two showing stronger than average correlations (high anti correlation values) and one showing much lower strength anti-correlations. Storm days are not always within the 5-95th percentile. Figure 6.2 (b) gives a similar message, that storm day correlations are often within the range of correlations seen for the entire dataset. Interestingly, this plot also shows that most of the maximum and minimum correlation values for each December were not the result of storm activity. Figure 6.2 may suggest that there is no consistent correlation response to geomagnetically disturbed conditions between the variables foF2 and hmF2.

The strong anti-correlation seen between foF2 and hmF2 is caused mainly by the changes that occur at dawn and dusk, foF2 rises at dawn and decreases at dusk, whilst hmF2 does the opposite. It was thus considered that storm conditions being present at dawn or dusk could have a greater impact on the amount of cross-correlation observed than storm conditions in the centre of the day. This could be the reason why no consistent cross-correlation response to storm conditions is observed. The storm days were therefore split into 3 categories using the high latitude K-indices listed in Table 6.2. The categories of each storm using these specifications are listed in Table 6.3.

Table 6.3: Storm days and their high latitude K indices and consequential storm classification. Elevated values are highlighted in blue.

Date	High Latitude (College) K-indices	Storm Classification
2014 12 07	4 3 3 6 7 6 5 3	Dusk
2014 12 12	2 2 6 5 6 6 4 3	All-day
2014 12 15	1 2 5 5 6 4 3 1	Dawn
2014 12 22	5 5 5 5 2 3 1 1	Dawn
2014 12 29	1 2 3 5 6 6 3 4	Dusk
2015 12 01	2 2 1 6 6 5 3 3	Dusk
2015 12 05	0 0 5 5 5 5 3 2	All-day
2015 12 06	2 4 4 7 7 5 3 3	Dusk
2015 12 10	2 4 5 5 6 4 4 2	Dawn
2015 12 11	3 4 6 6 5 5 2 2	All-day
2015 12 20	2 6 6 7 7 7 6 5	All-day
2015 12 21	3 6 6 7 5 3 2 2	Dawn
2015 12 31	2 2 6 5 7 6 6 5	All-day

Dawn storms were those with an elevated value (5 or above) in the first three K measurements, Dusk storms were those with an elevated value in the last three K measurements, and All-day storms are those where elevated values were seen in both the first three and last three K indices. Each storm day fits into one of these categories. Figure 6.3 shows Figure 6.2 panel (a) replotted with storm lines split into their classifications, indicated by colour. Data from the 11/12/2015 storm were not available.

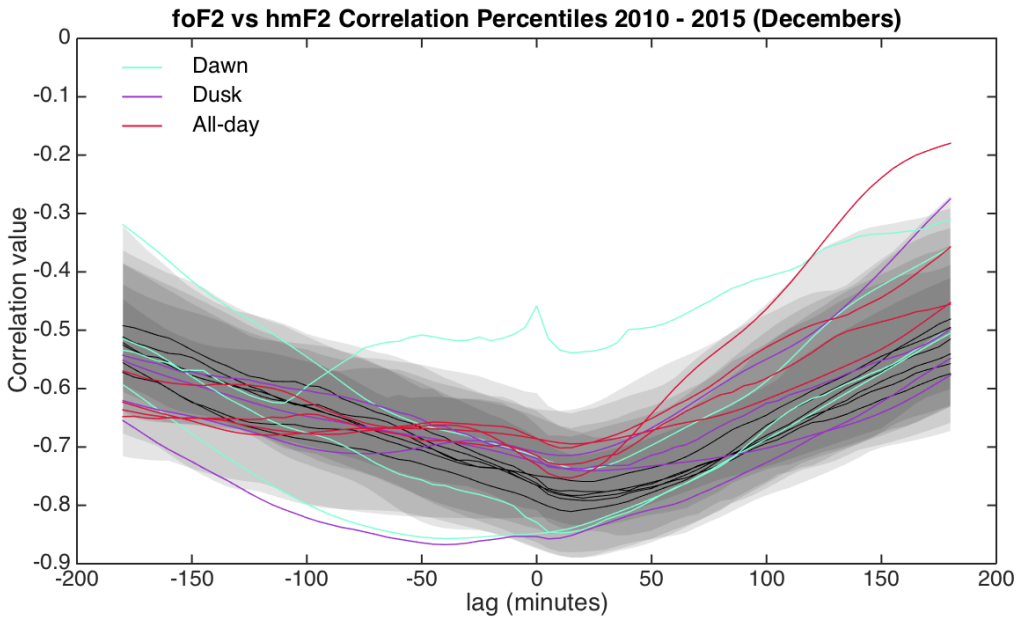

Figure 6.3: Cross-correlation values between foF2 and hmF2 observed at the EB040 ionosonde for each December with coloured lines depicting storm day correlations and patches indicating 5th and 95th percentiles. Negative lag indicates that foF2 leads and hmF2 lags.

Figure 6.3 shows the correlation response to the time of day at which geomagnetic conditions were detected. It can be seen that there is no consistent response. Dawn storms (light blue lines) are seen to cause stronger anti-correlations than the medians for two storms, and weaker anti-correlations than the medians for the other two storms. Dusk storms (purple lines) also do not show a consistent response, with some storms strengthening correlations and others weakening it. All-day storms (red lines) appear to cause anti-correlations to weaken at positive lags, and at negative lags correlations stay close to the medians. Of the two outliers seen from lags of roughly -100 to -20 minutes one was a Dawn storm and the other a Dusk storm. The positive outlier is a Dawn storm. Only one All-day storm leaves the 5-95 percentile patch between lags of +125 and +180 minutes. This may suggest that there is no consistent correlation response to the presence of geomagnetically disturbed conditions observed at either dawn or dusk, but that storms with disturbed conditions at both dawn and dusk may result in reduced strength of the anti-correlation between foF2 and hmF2.

6.4.2 Cross-correlations between ionosonde parameters and GPS derived TEC

Figures 6.4 and 6.5 depict the results from cross-correlating foF2 and GPS TEC, and hmF2 and GPS TEC respectively, at the four GPS receivers. Ionosonde parameters were observed by the EB040 ionosonde and TEC time series were derived using the new technique introduced in Chapter 5. The locations of the ionosonde and four receivers are shown in Figure 6.1. It should be noted that this

dataset is small so conclusions should be treated with caution. As data from only one December (2015) were available for this analysis the patches on these plots represent the 5-95 and 25-75 percentiles at each lag for the month. The black line represents the median value at each lag for the month, and each pink line represents cross-correlations for a single storm day.

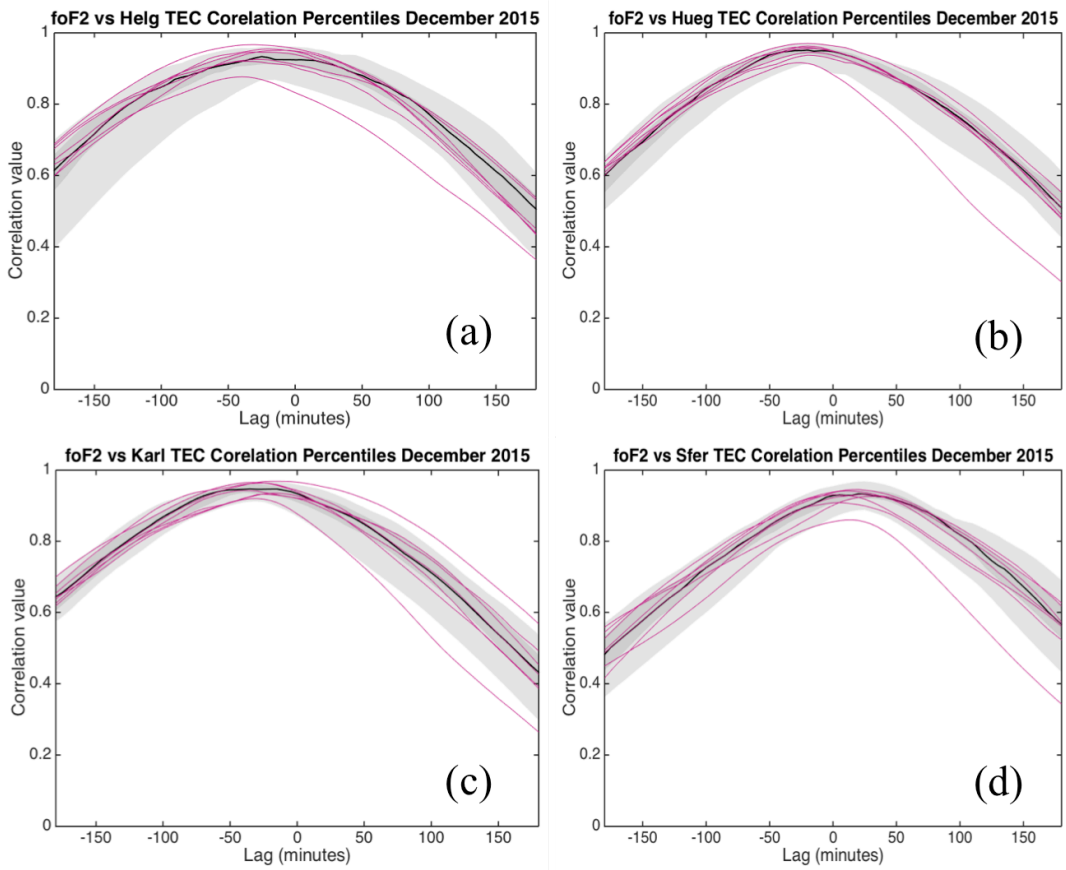

Figure 6.4: Cross-correlations between foF2 observed at EB040 and GPS TEC with pink lines indicating storm days at receivers (a) Helg, (b) Hueg, (c) Karl and (d) Sfer. Shading indicates the 5-95 and 25-75 percentiles. Negative lag indicates that foF2 leads and TEC lags. Note: only positive cross-correlations shown.

Figure 6.4 compares storm cross-correlations to typical crosscorrelations between ionosonde foF2 and GPS derived TEC for December 2015. Chapter 4 Section 4.8 showed a strong correlation across all geomagnetic conditions, peaking close to a value of 1 sustained for roughly 50 minutes. This relationship appears to hold also in storm conditions. It can be seen that across all four panels most of the storm day correlations (pink lines) seem typical for the month. Most of the pink lines in each panel are close to the median values for the month (black line), and are also within the percentile patches. Cross-correlations for every storm day in all panels peak above 0.8 and remain above this value for approximately 150 minutes of lags.

Figure 6.4 (a) shows one pink line slightly above the 95th percentile from lags of approximately -100 to -25 minutes, and one pink line below the 5th percentile from lags of -25 minutes to lags of 180 minutes. Figure 6.4 (b) has one storm event evidenced with correlations below the 5th percentile from lags of 0 to 180 minutes. Figure 6.4 (c) has one storm line above the 95th percentile from lags of 0 to 180 minutes and one stormline below the 5th percentile from 50 to 180 minutes. Figure 6.4 (d) has one stormline below the 5th percentile from lags of approximately -10 minutes to 180 minutes. The largest amount of difference between a storm line and patch is seen in Figure 6.4 (b) when one storm line is approximately 0.1 below the correlation value of the 5th percentile at a lag of 150 minutes. The pink line falling below the 5th percentile patch in each panel is always for the same storm, which occurred on 20/12/2015, and the storm above the 95th percentile in Figure 6.4 (c) was that which occurred on 1/12/2015

All other storm lines remain inside the percentile patches in all four panels. This suggests that ionosonde foF2 and GPS derived TEC remain strongly correlated in geomagnetic storms.

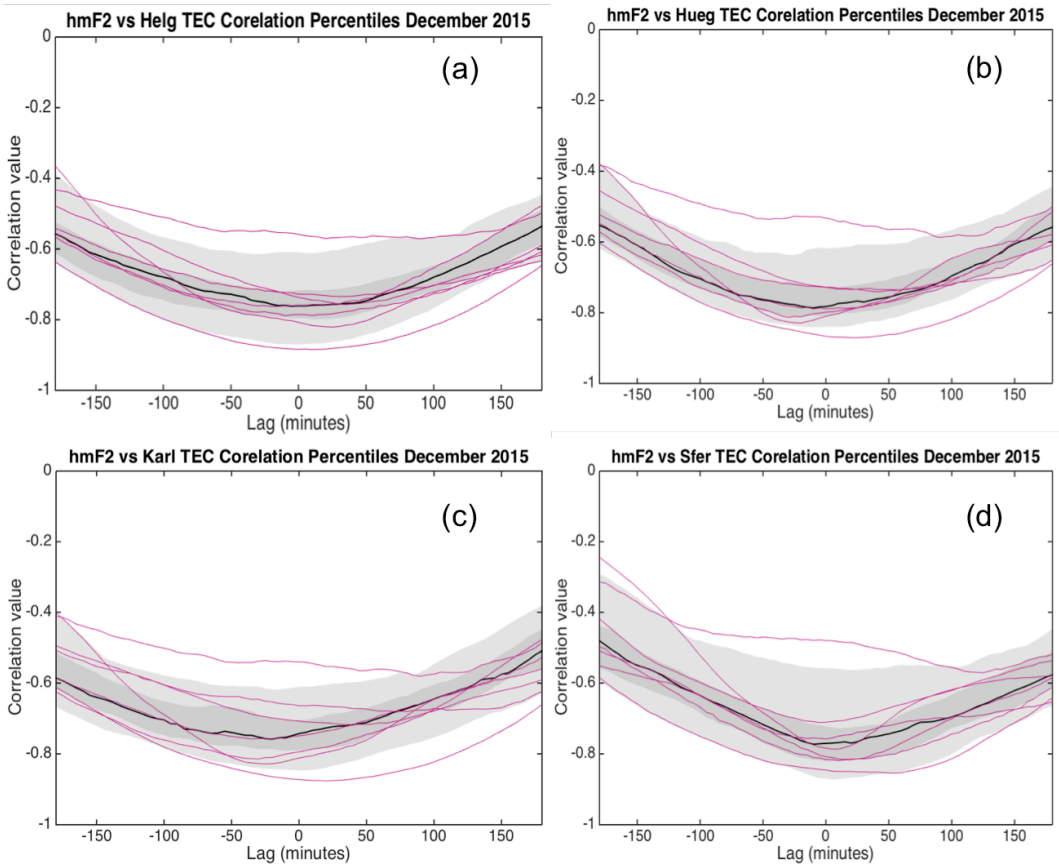

Figure 6.5: Crosscorrelations between hmF2 observed at EB040 and GPS derived TEC with pink lines indicating storm days at receivers (a) Helg, (b) Hueg, (c) Karl and (d) Sfer. Shading indicates the 5-95 and 25-75 percentiles. Negative lag indicates that the hmF2 leads and TEC lags. Note: only negative cross-correlations shown.

Chapter 4 Section 4.8 showed a strong anti-correlation between ionosonde hmF2 and GPS TEC peaking at -0.8 and sustained for roughly 100 minutes (see Figure 4.24 (d)). Figure 6.5 shows that this relationship is maintained during geomagnetically disturbed conditions. In Figure 6.5 (a) 5 of the 7 storm lines are within the 25-75 patch for most lags and remain within the 5-95 patch for all lags. One storm day remains below the 5th percentile over all lags, suggesting hmF2 and GPS TEC were more strongly anti-correlated during this storm. However, a second pink line is above the 95th percentile between lags of roughly -160 to 125 minutes, suggesting less correlation between the two parameters. Figure 6.5 (b) shows a similar pattern to Figure 6.5 (a), with 5 storms close to the median, one below the 5th percentile and one above the 95th percentile. Figure 6.5 (c) again shows the two storms outside the most extreme patch, however in this panel the other 5 storms (those that remain inside at least the most extreme patch across all lags) are grouped less strongly around the median than in Figure 6.5 (a) and (b). Two storms are also seen outside the 5-95th percentile patch in Figure 6.5 (d), however it should be noted that the patches for this panel are broader than in the other patches, suggesting a less consistent relationship between the two parameters at Sfer over the month.

Investigations into the two lines that are outside the 5-95 patch in all four panels revealed that it was conditions on 01/12/2015 that caused a weakening of the anticorrelations, and the conditions on 21/12/2015 which caused a strengthening. This suggests that a storm causes similar response to the amount of correlation between hmF2 and GPS TEC at all four locations. The most extreme divergence of storm correlations from the 5-95th percentile patch is approximately 0.1, and can be observed in panel (b) from lags of roughly -100 minutes to 0, and in panel (d) at a lag of roughly 0 minutes. The range of responses suggest that there is no consistent response of the correlation between hmF2 and GPS TEC to storm conditions, as the anti-correlation may be either strengthened or weakened. In the most extreme cross-correlation weakening the anti-correlations reach a value above -0.5, meaning they would not be considered correlated.

6.4.3 Storm-time cross-correlations between GPS derived TEC at different locations

It was of interest to investigate the performance of the new TEC derivation technique in storm conditions. To accomplish this a cross-correlation analysis was conducted between time series generated by the new technique at two single-frequency GPS receivers at different locations on the storm day. The number of usable days for each receiver pair analysis after unusable days were discarded is listed in Table 6.4.

Table 6.4: Number of usable days in December 2015 for cross-correlations analysis between GPS receiver pairs.

Receiver pair	Number of usable days in December 2015
Helg vs. Hueg	31
Hueg vs. Sfer	27
Helg vs. Sfer	27

Chapter 5 Section 5.5 showed that correlations between TEC time series of GPS receivers were high, peaking above 0.9 and sustained for lags over 50 minutes. Figure 6.6 shows cross-correlations between pairs of GPS receivers. The patches represent the 5th-95th and 25th -75th percentiles for December 2015; the blue line is the median, and the pink lines the storm days. GPS data were available for 11/12/2015 so this storm is included in GPS to GPS analysis.

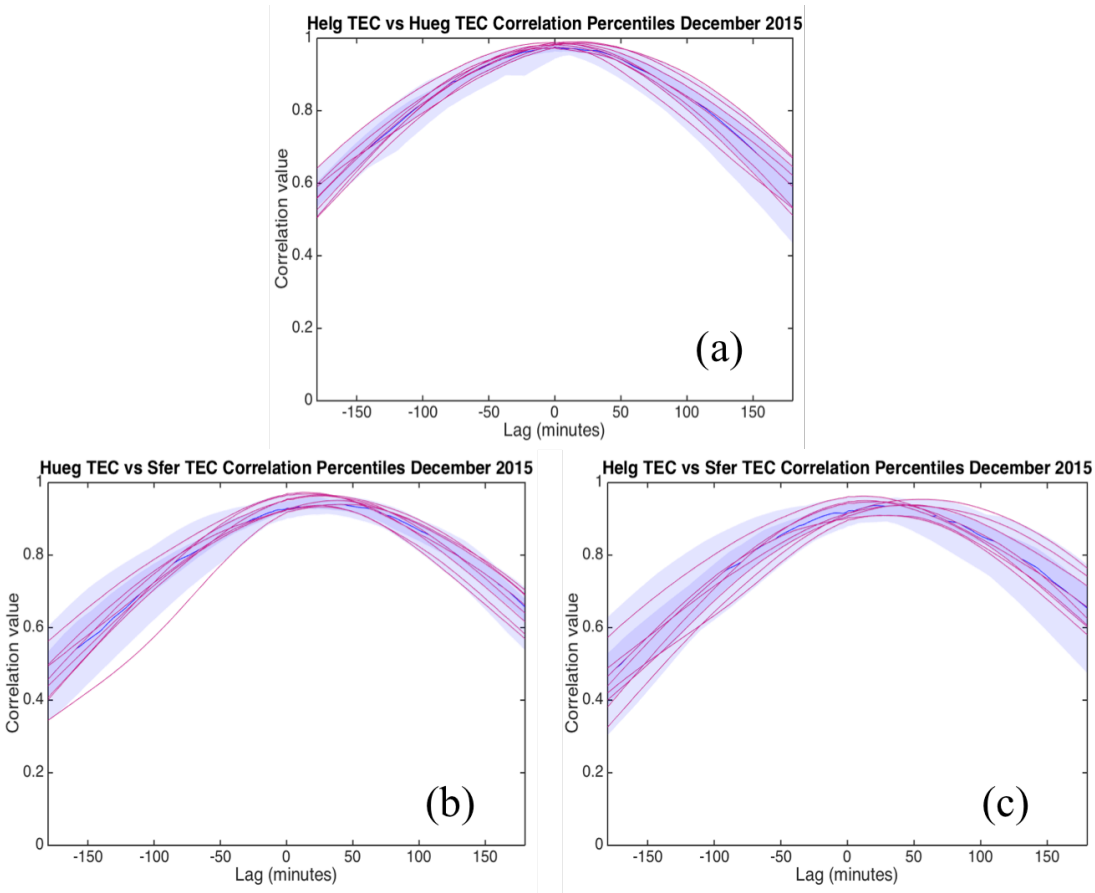

Figure 6.6: Correlation analysis of time series of GPS derived relative TEC from pairs of GPS receivers, (a) Helg vs. Hueg, (b) Hueg vs. Sfer and (c) Helg vs. Sfer, for December, with pink lines representing storm day correlations. Shading indicates the 5-95 and 25-75 percentiles. Negative lag indicates that the first location leads and second location lags.

Figure 6.6 compares cross-correlations on storm days to typical December correlations between single frequency GPS receivers at different locations. It can be seen that in all 3 panels the storm lines (pink) are similar to the median (blue line). Correlations between receivers on each storm day peak above a value of 0.8, and remain above a value of 0.8 for roughly 150 minutes of lags. In Figure 6.6 (a) and Figure 6.6 (c) all storms fall within the 5-95 percentile patch over almost all lags. In Figure 6.6 (a) 6 of the 8 storm lines stay within the 25-75 percentile patch over most lags, with 3 lines leaving this patch at approximately -100 minutes. In Figure 6.6 (b) storm lines follow the median, however there is one storm outside the 5-95 percentile patch from lags of -180 to lags of approximately -40 minutes. In Figure 6.6 (c) the storm lines are slightly less tightly grouped but several remain in the 25-75 percentile patch for most lags.

6.4.4 Conclusions

Figures 6.4, to 6.6 suggest that storm conditions do not significantly alter the cross-correlation relationship between foF2 and hmF2, foF2 and TEC or hmF2 and TEC. Pairs of TEC time series derived using the new technique at different receivers also remain strongly correlated in storm conditions. This suggests that the new TEC derivation technique consistently produces sensible time series in geomagnetic storm conditions and remains reliable. Good agreement is seen between TEC time series and those observed by an independent ionosonde in storm conditions, as well as between terrestrial receivers. Since this data set is small further long-term analysis of more events would be required to state these conclusions with greater confidence. However, there are limited numbers of storm events in recent years when the GPS GEO data are also available.

6.5 Case study: the geomagnetic storm of 20/12/2015

It was of interest to take a single day when a strong storm was observed and analyse the response in detail. The storm on 20/12/2015 was taken as a case study day for in depth analysis. This was the storm with the highest number of elevated K and Kp indices, as seen in Table 1. Coronal mass ejections (CMEs) in the days preceding 20/12/2015 reached Earth in the evening of 19/12/2015 and resulted in disturbed geomagnetic conditions, with G2 (moderate) storm conditions recognised between 03:00 and 06:00 UTC, and between 15:00 and 23:59 UTC on 20/12/2015 (Space Weather Prediction Centre (SWPC) 2015a; Space Weather Prediction Centre (SWPC) n.d.).

6.5.1 K-index values and MIDAS observations of case study day

Both Kp and high latitude K values on 20/12/2015 were measured as 5 or above for 7 out of 8 daily recordings, and the high latitude K values remained at a value of 7 for three consecutive recordings (Space Weather Prediction Centre (SWPC) n.d.). An example quiet day was also identified for comparison purposes. Both

solar and geomagnetic field activity were quiet in the days preceding 25/11/2015 (Space Weather Prediction Centre (SWPC) 2015b). K measurements on 25/11/2015 remained at a value of 0 for 7 out of 8 planetary values, and for all 8 high latitude values (Space Weather Prediction Centre (SWPC) n.d.). Figure 6.7 illustrates K values for dates surrounding the storm and quiet days.

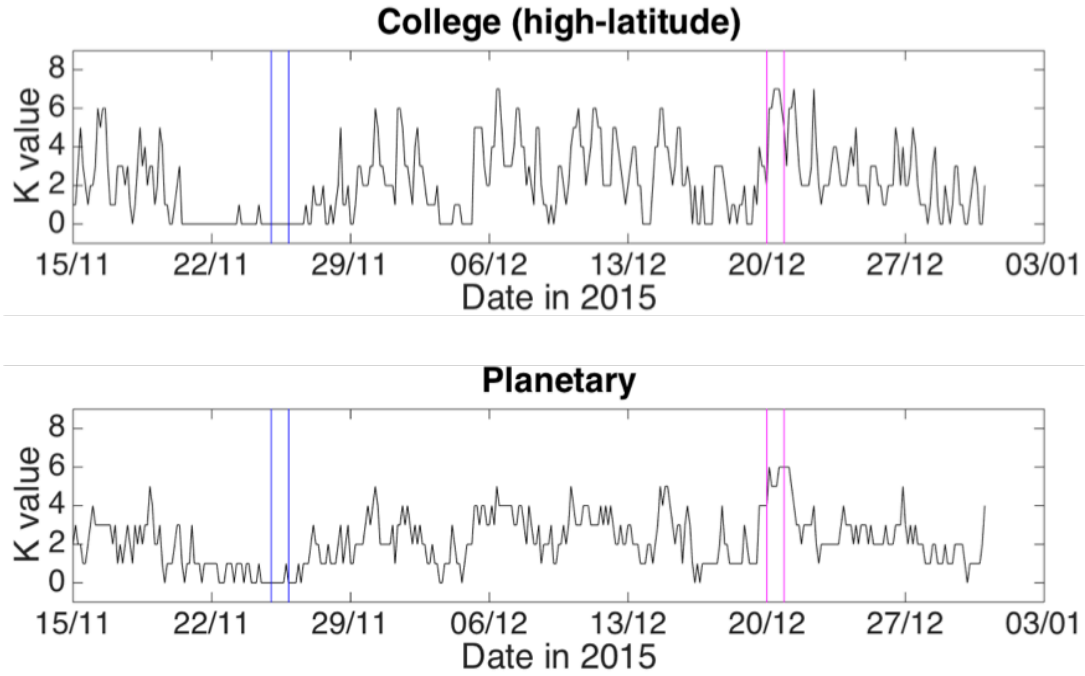

Figure 6.7: 3-hour K indices for the quiet day (blue lines) and storm day (pink lines) for (a) High latitudes (College Observatory, Fairbanks, Alaska) and (b) Planet wide.

It can be seen from Figure 6.7 that the storm day has significantly higher K values for both high latitude and planetary observations than the quiet day. Figure 6.7 also shows that the case study quiet day is preceded by several quiet days.

The state of the ionosphere over Europe is illustrated by Figure 6.8, generated by the Multi Instrument Data Analysis System (Mitchell & Spencer, 2003). MIDAS makes use of slant TEC measurements provided by a large number of receivers of the global navigational satellite system (GPS), along with ionosonde data. MIDAS however does not incorporate TEC observations from single-frequency receivers made using the new technique. MIDAS was first developed by Mitchell and Spencer 2003 at the University of Bath (Mitchell & Spencer, 2003). MIDAS images the ionosphere via the technique of tomography in three spatial and one temporal dimension, using the International Reference Ionosphere (IRI) (Bilitza 1990) model as a background. Figure 6.8 shows selected MIDAS modelled vertical TEC over the northern hemisphere for the storm day.

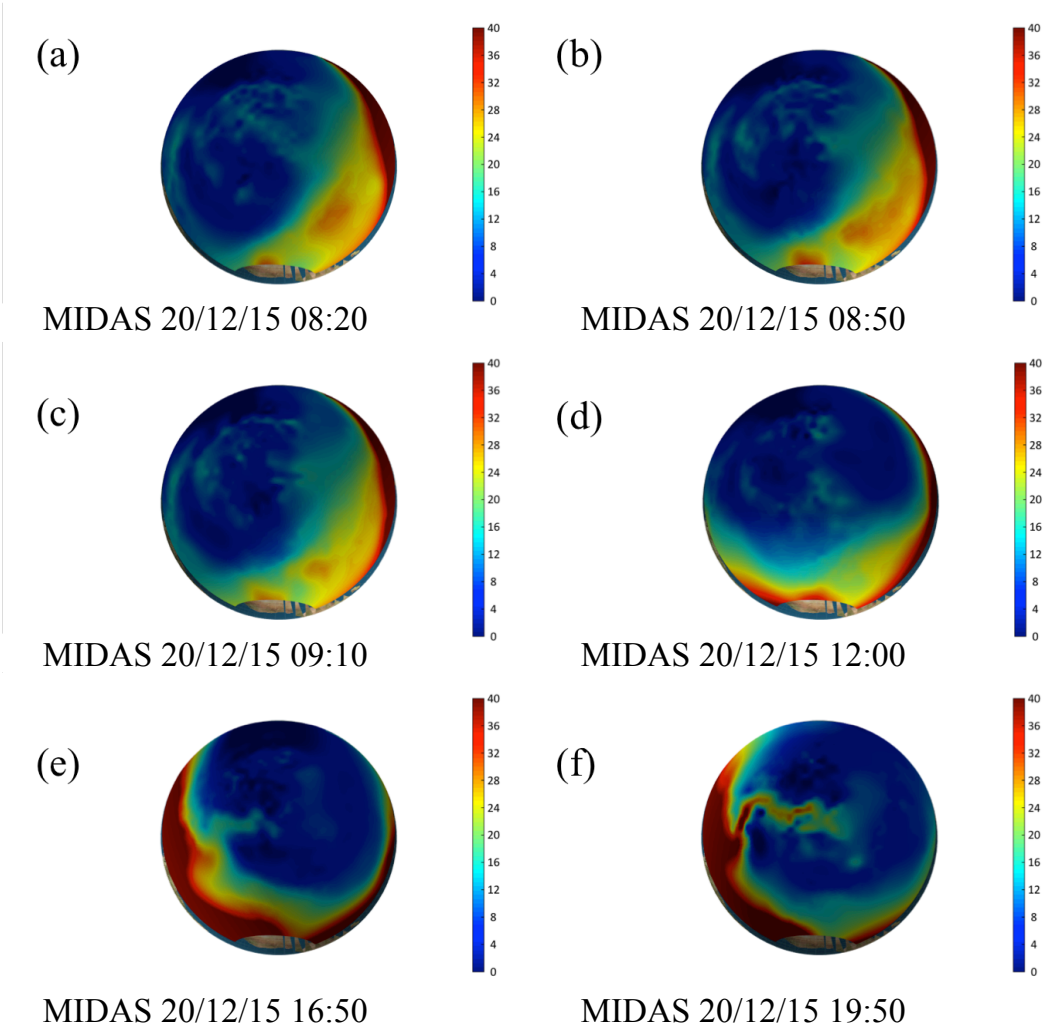

Figure 6.8: MIDAS Northern hemisphere vertical TEC maps of 20th December 2015 at: (a) 08:20 (b) 08:50 (c) 09:10 (d) 12:00 (e) 16:50 (f) 19:50 UTC. Units of the colourbar are TECU where one TECU is equal to 10^{16} electrons m^{-2}.

In Figure 6.8 (a), (b) and (c) it can be seen that two patches are higher level TEC seen at 8:20, 8:50 and 09:10, but which have blended into the surroundings by 12:00 (panel (d)). A tongue of ionisation heading polewards can be seen in Figure 6.8 (e) and Figure 6.8 (f) over North America.

6.5.2 Case study cross-correlation analysis between ionosonde parameters

The hmF2 and foF2 time series for both the case study day and quiet day is shown in Figure 6.9, which depicts the 24-hour time series of both parameters measured at the EB040 ionosonde.

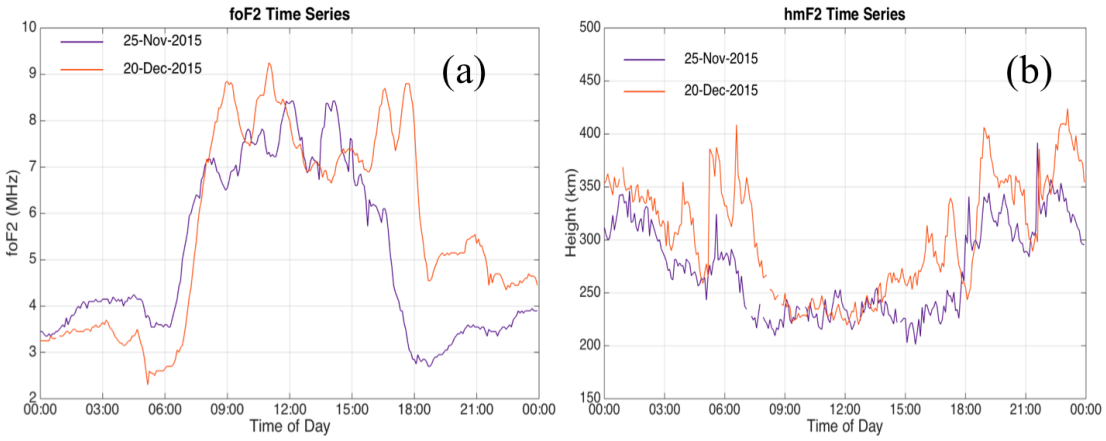

Figure 6.9: Ionosonde observed (a) foF2 and (b) hmF2 for geomagnetically quiet day (purple) geomagnetically stormy day (orange).

Figure 6.9 (a) shows that values for foF2 peak slightly higher on the storm day (orange) than the quiet (purple), but not significantly. A double diurnal maximum is also noticeable in the storm day foF2 time series. Figure 6.9 (b) shows that the hmF2 time series is noticeably disturbed on the storm day (orange). The periods between 03:30 and 06:00 and between 15:00 and 23:59, when storm conditions were acknowledged, contain jumps in observed height that are slightly greater than are seen in the quiet day.

Chapter 4 Section 4.5 demonstrated a strong cross-correlation relationship between foF2 and hmF2, with an anticorrelation reaching values of -0.8 for over 50% of the data. It was of interest to examine how this relationship was affected by the storm in this case study. In Figure 6.10 each grey patch represents the 5th and 95th percentile values at each lag value for one December's data. Each black line represents the median for a December. The 6 patches represent percentiles from 6 Decembers data, 2010 to 2015, and the black lines the 6 medians. The pink line indicates the correlations calculated for the 20th December 2015 storm day.

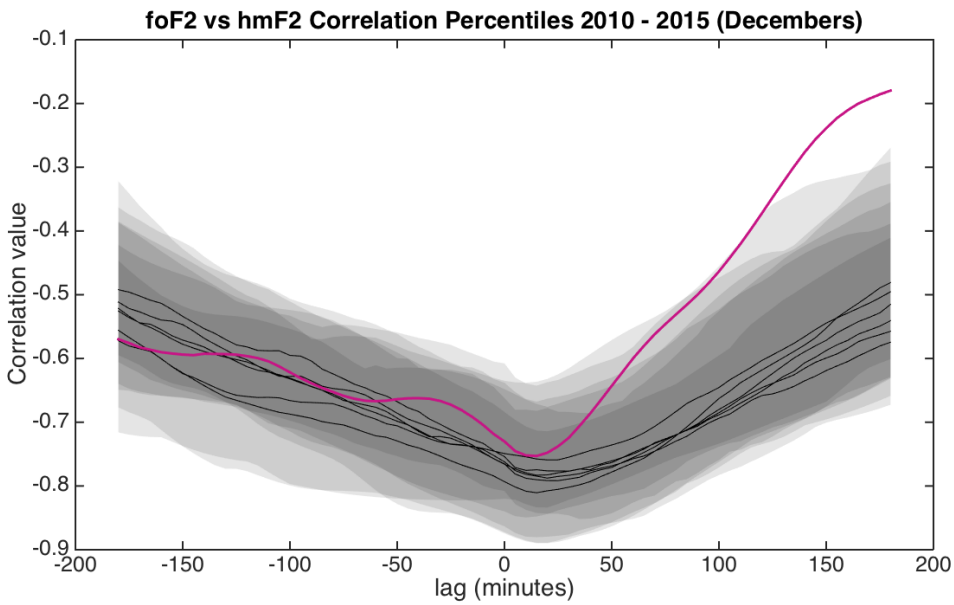

Figure 6.10: 5th and 95th percentiles of cross-correlation data for each December, pink line depicts storm day correlations. Black lines show median correlations for each December and the pink line represents correlations for the storm day. Negative lag indicates that foF2 leads and hmF2 lags. Note: Only negative correlations are shown.

Figure 6.10 shows how the case study storm day correlations relate to correlations in past Decembers. It can be seen that the negative lags from -180 to -50 minutes are typical, within all 6 patches and similar to the median lines. From -50 minutes to 0 minutes the storm day correlations are slightly closer to zero than the median values, but still within the range of all 6 patches. The positive lags however are noticeably different. The storm day correlations, which never fall to as strong an anti-correlation as the median for any year, approach zero correlation very rapidly. At lags of roughly +60 minutes the storm day correlations are closer to zero than the 95th percentile of 4 out of the 6 Decembers. At lags of approximately 100 minutes the storm day correlations have moved above -0.5 and are closer to zero than for the 95th percentile of any December. This suggests that the two parameters are less strongly correlated in storm conditions than in normal or quiet conditions. For Figure 6.11 the patch edges represent the maximum and minimum values at each lag for 6 Decembers, with the solid black lines the medians and the pink line the storm days.

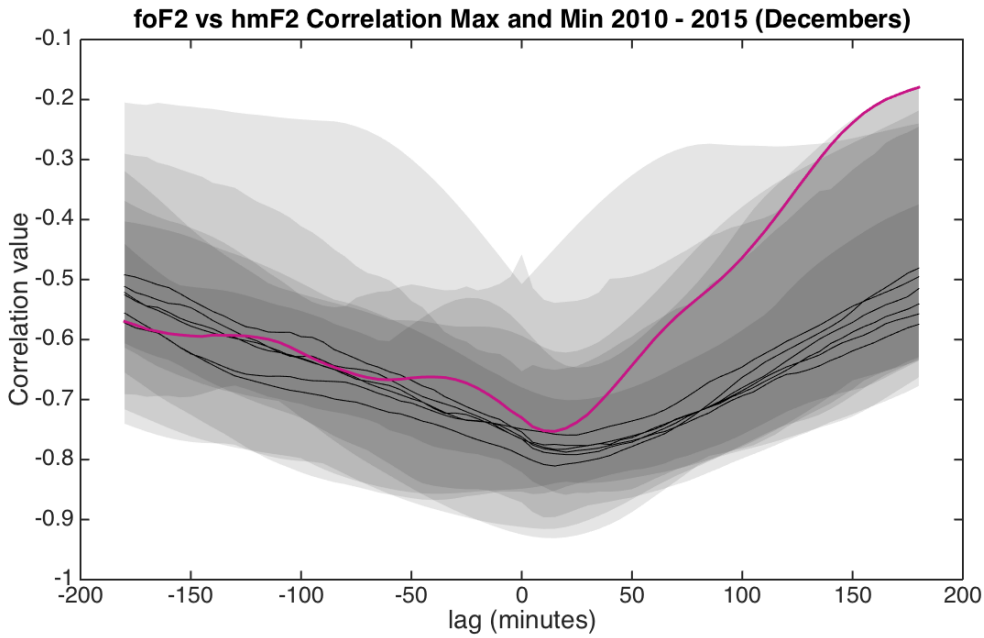

Figure 6.11: Maximum and minimum cross-correlation values for each December, pink line depicts storm day correlations. Black lines show median correlations for each December and the pink line represents correlations for the storm day. Negative lag indicates that foF2 leads and hmF2 lags. Note: Only negative correlations are shown.

It can be seen that the storm day correlations (pink line) are not exceptional when compared to the patch edges. For lags of 40 to 100 minutes the storm day is outside of the maximum of one December, at a lag of 100 minutes it is outside 2 patches, and outside a third at a lag of approximately 120 minutes. After a lag value of 150 minutes correlations are outside all patches and consequently are closer to zero than have been seen in any year. The unusual shape of the patches in Figure 6.11 suggests that the patch edges may have resulted from outliers within the dataset.

Figures 6.10 and 6.11 suggest the amount of correlation between foF2 and hmF2 is sensitive to strong geomagnetic conditions. Storm conditions were identified between 03:00 and 06:00 UTC, and between 15:00 and 23:59 UTC, meaning that at shifted lags (both positive and negative) storm conditions will be correlated with non-storm conditions. Figure 6.9 shows that hmF2 values between 03:00 and 06:00 and between 15:00 and 23:59 were elevated on the storm day when compared to the normal day. At increasing lags the central section of the foF2 time series begin to be compared to the post noon section of the hmF2 time series. The F region can be lifted by neutral wind activity without affecting the electron density of the region, and conversely the electron density of the F region can be affected by storm activity without any influence upon the vertical location of the peak height. It has been observed that ionospheric electron density can be increased by disturbed conditions following the arrival of storm, and then later

decrease in a recovery period following the storm (Hargreaves 1979). It has also been observed that during storm conditions there can be a decrease in ionosonde observed foF2 values and a concurrent increase in ionosonde observed hmF2 (Hargreaves 1979), although activity meeting this description is not obvious in Figure 6.9. This relationship has been attributed to a decrease in the speed of the ionosonde transmitted radio wave, rather than to any physical ionospheric change (Hargreaves 1979).

A decrease in foF2, increase in hmF2 or both, could result in a less extreme anticorrelation between the time series than in normal conditions. A noticeable feature in Figure 6.9 is that on the storm day foF2 values remained elevated around dusk for longer than is typical. Figure 6.12 shows hmF2 and foF2 profiles for all December days 2010 to 2015, with the storm day time series represented by the black line in each panel.

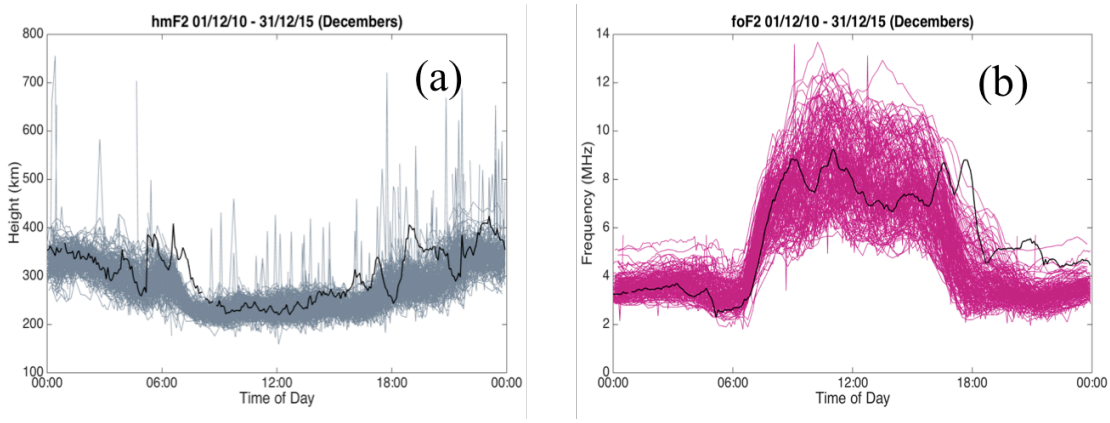

Figure 6.12: 24-hour time series ionosonde observations from the EB040 ionosonde for (a) hmF2 and (b) foF2 with the storm day time series in black.

Figure 6.12 (a) shows that the magnitude of hmF2 values appear typical for some of the storm day, but not all. It appears that hmF2 values start to fall (after 06:00) later on the storm day than is observed on any other December day. From 14:00 to 23:59 values are often near to the top of the band and peak above the band 4 times. Figure 6.12 (b) shows that the magnitude of foF2 values for the storm day appear typical when compared to values from all Decembers up until roughly 17:00, after which they remain higher than is seen on most December days. foF2 values remain elevated for longer and start to decrease later on the storm day than has been observed when compared to all December days over 6 years. foF2 values remain higher than is typically seen from 18:00 until 23:59. This unusual behaviour from 18:00 onwards may have reduced the strength of anti-correlations seen in positive lags in Figures 6.10 and 6.11. A less strong dip in foF2 values whilst hmF2 values stay constant will reduce the strength of the anti-correlation.

6.5.3 Case study cross-correlation analysis between ionosonde parameters and GPS derived TEC

Figure 6.13 depicts the daily time series of the GPS derived TEC from the hueg receiver and the observed foF2 time series at the EB040 ionosonde on both the normal day and the storm day.

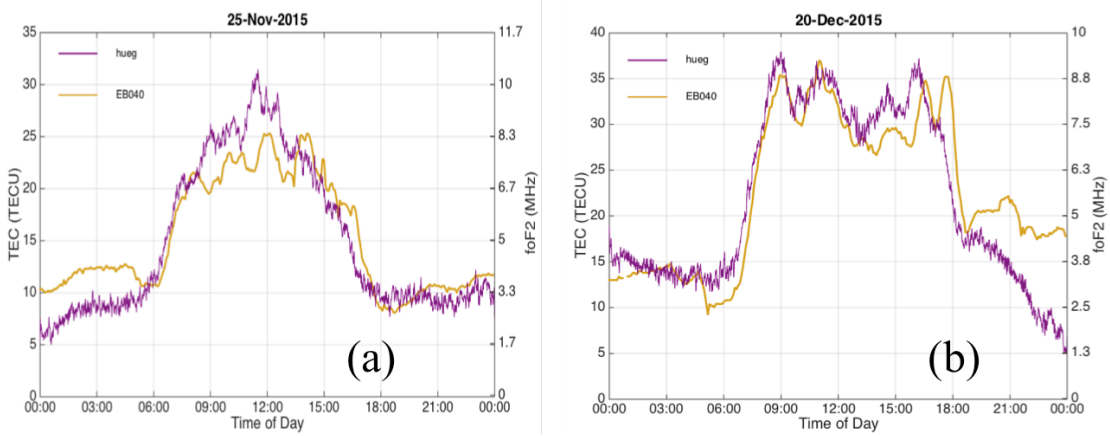

Figure 6.13: GPS relative TEC (left axis) and ionosonde foF2 (right axis) on (a) geomagnetically quiet day and (b) geomagnetically stormy day.

Figure 6.13 shows that the time series for the storm and quiet days are not noticeably different. Values for both TEC and foF2 remain similar for both days; there is a slight increase in values for both parameters but not by a significant amount. The GPS TEC and ionosonde foF2 follow each other well, showing a similar pattern throughout the time series, suggesting that the TEC derivation technique has performed reliably during the storm.

Figures 6.14 and 6.15 shows the cross-correlations between parameters observed by the EB040 ionosonde, and GPS derived TEC calculated using the technique introduced in Chapter 5 at four single frequency ground receivers. Figure 6.14 shows the correlations between ionosonde foF2 and GPS TEC for daily 24-hour time series over only December 2015. In these plots the three shaded patches represent the 5^{th}-95^{th} percentile and the 25^{th} -75^{th} percentile, the black solid line represents the median correlations at each lag for the year, and the pink line the correlations from the case study storm day.

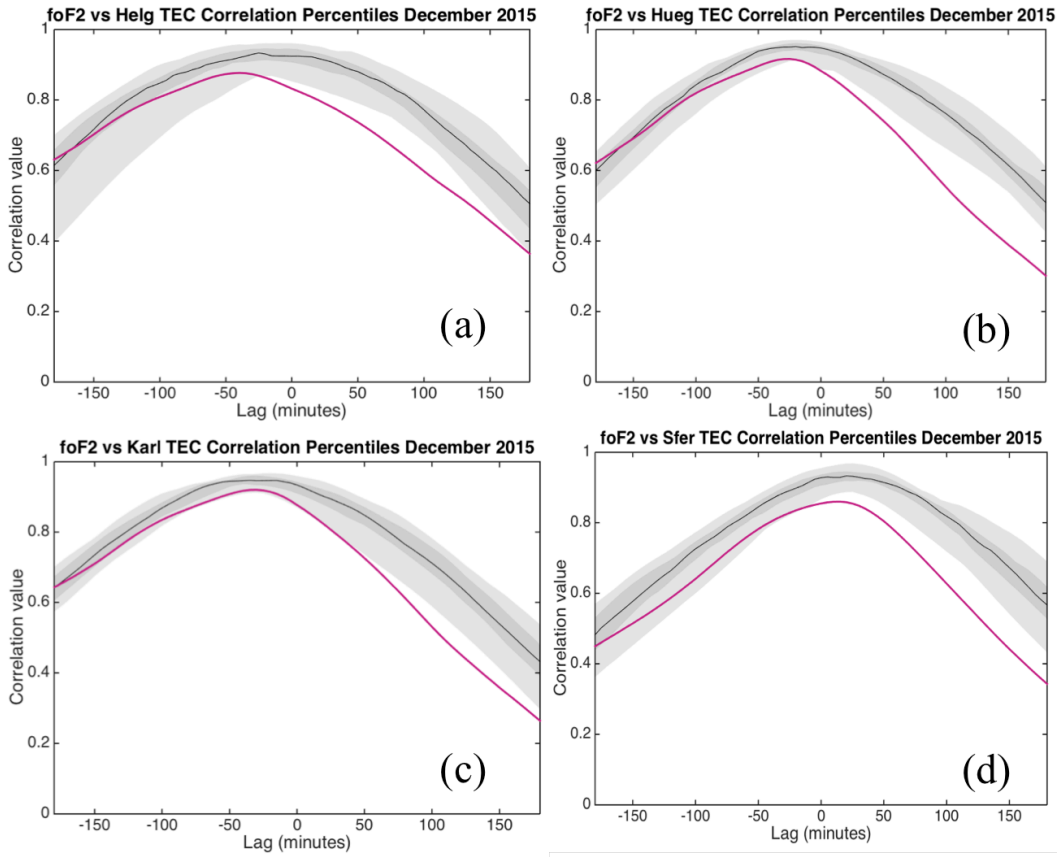

Figure 6.14: Cross-correlations between foF2 observed at EB040 and GPS TEC with pink lines indicating the case study storm day at receivers (a) Helg, (b) Hueg, (c) Karl and (d) Sfer. Shading indicates the 5-95 and 25-75 percentiles. Negative lag indicates that foF2 leads and GPS TEC lags. Note: only positive cross-correlations shown.

Figure 6.14 compares storm day correlations between foF2 and GPS TEC to typical December correlations for 2015. The storm day correlations (pink line) follow the same shape as the patch correlations in all four panels. In all four panels the storm correlations fall outside the 5-95 percentile patch in positive lags, but not by a large amount, with the furthest deviation seen in panel (b) with a difference of cross-correlation of roughly 0.1. This indicates that although parameters may be slightly less strongly correlation in strong storm conditions, they still remain highly correlated. This relationship is logical as the F region, and specifically the F2 region, is responsible for the greatest contribution to the TEC value along a path (Mosert et al. 2002). Thus, if the electron density of the F region is affected by a geomagnetic storm this should in turn influence the TEC values in the same way.

The same technique was used to compare cross-correlations between hmF2 and GPS derived TEC on the storm day to typical December correlations.

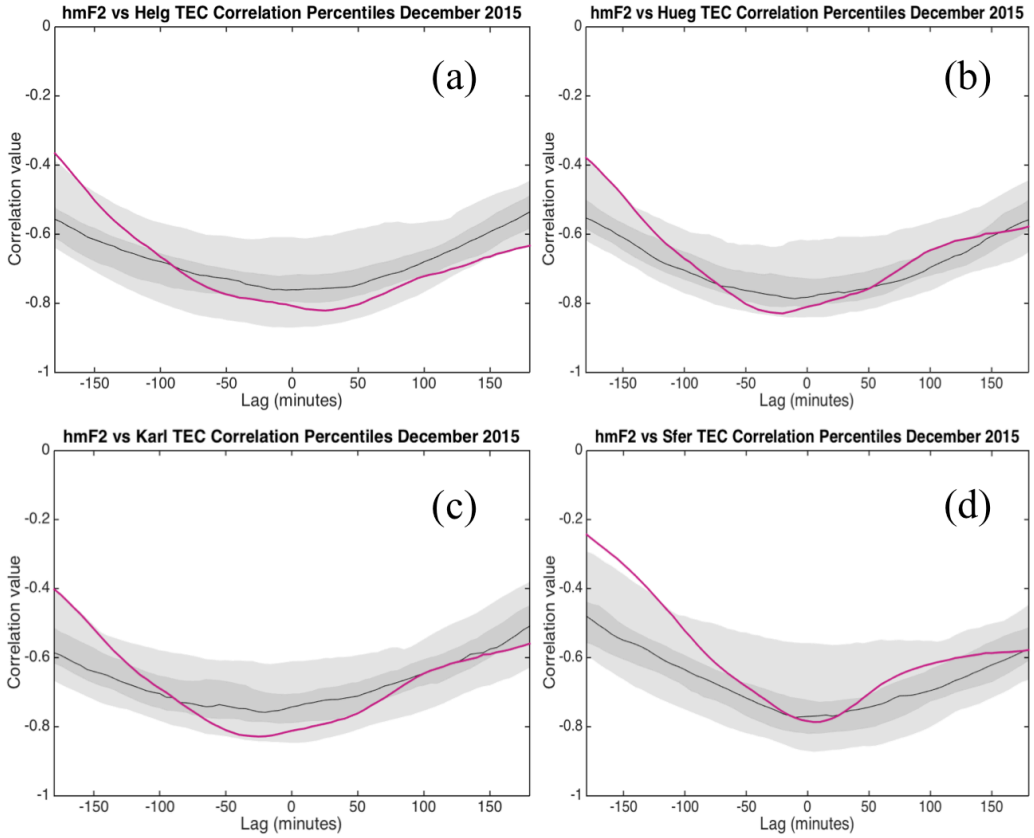

Figure 6.15: Cross-correlations between hmF2 observed at EB040 and GPS TEC with pink lines indicating the case study storm day at receivers (a) Helg, (b) Hueg, (c) Karl and (d) Sfer. Shading indicates the 5-95 and 25-75 percentiles. Negative lag indicates that hmF2 leads and GPS TEC lags. Note: only positive cross-correlations shown.

Figure 6.15 compares the cross-correlations between hmF2 and GPS TEC to correlations from December 2015. Storm day correlations (pink line) are within the 5-95 percentile for most lags in all four panels. In all four panels a strong anti-correlation between the parameters is seen, peaking at -0.8 for Figure 6.15 (a) (b) and (c), and below -0.7 for Figure 6.15 (d). In all four panels anti-correlations become less strong from -150 to -180 minutes. In Figure 6.15 (d) storm correlations are outside the 5-95 percentile at these lags. This suggests that in strong geomagnetic storm conditions ionosonde hmF2 and GPS TEC remain strongly anti-correlated.

For correlations between ionosonde parameters and GPS TEC it should be remembered that only a month's data is available, and with such a small data set any conclusions must be regarded with caution.

6.5.4 Case study cross-correlation analysis between GPS derived TEC at different locations

The cross-correlation analysis completed in Section 6.4.3 between pairs of GPS receivers was repeated using correlations from only the storm day. As before Figure 6.16 compares storm-time correlations to typical cross-correlation values. These plots use data from December 2015 and patches represent the 5-95 and 25-75 percentiles at each lag for the month.

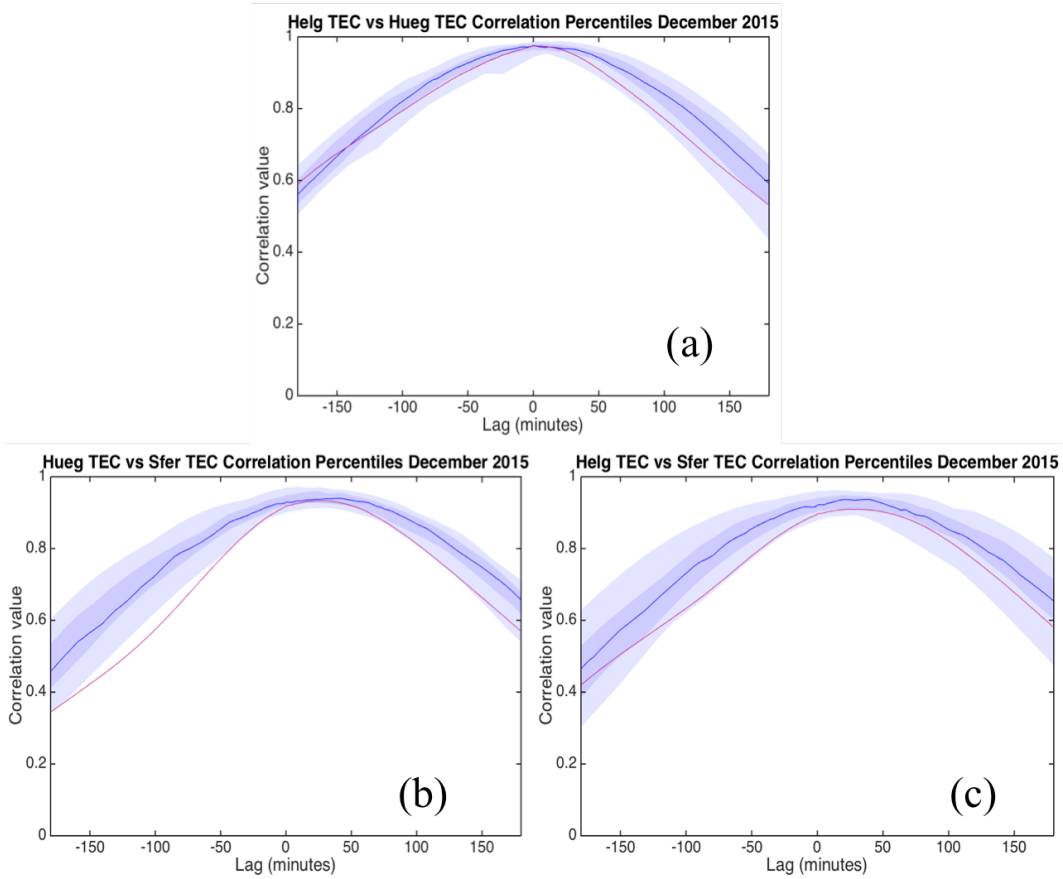

Figure 6.16: Correlation analysis of time series of GPS derived relative TEC from pairs of GPS receivers, (a) Helg vs. Hueg, (b) Hueg vs. Sfer and (c) Helg vs. Sfer, for December, with pink lines representing case study day correlations. Shading indicates the 5-95 and 25-75 percentiles. Negative lag indicates that the first location leads and second location lags.

It can be seen from Figure 6.16 that correlations between GPS receivers remain high on the storm day, peaking above a value of 0.8 and remaining above this value for over 100 minutes of lags in all three panels. A decrease in the strength of the correlation at negative lags is seen in panel (b), with storm day correlations falling slightly outside the 5-95 percentile patch. This suggests that the time series generated by the new technique at all three receivers were similar, indicating a good agreement between stations.

6.5.5 Comparisons between GPS derived TEC and MIDAS modelled TEC

In order to further assess the performance of the new technique in storm conditions, TEC time series derived using the new technique were compared with MIDAS TEC time series for as close latitudes and longitudes as was possible. The closest available latitudes and longitudes are listed in Table 6.5:

Table 6.5: GPS receiver locations and closest MIDAS co-ordinates.

	Latitude	Closest MIDAS Latitude	Longitude	Closest MIDAS Longitude
Helg	54.1	54	7.53	8
Hueg	47.5	48	7.35	8
Karl	49.0	50	8.24	8
Sfer	36.28	36	6.12	6

Figure 6.17 shows a direct comparison between the GPS derived TEC at the four single frequency receivers and the corresponding MIDAS TEC.

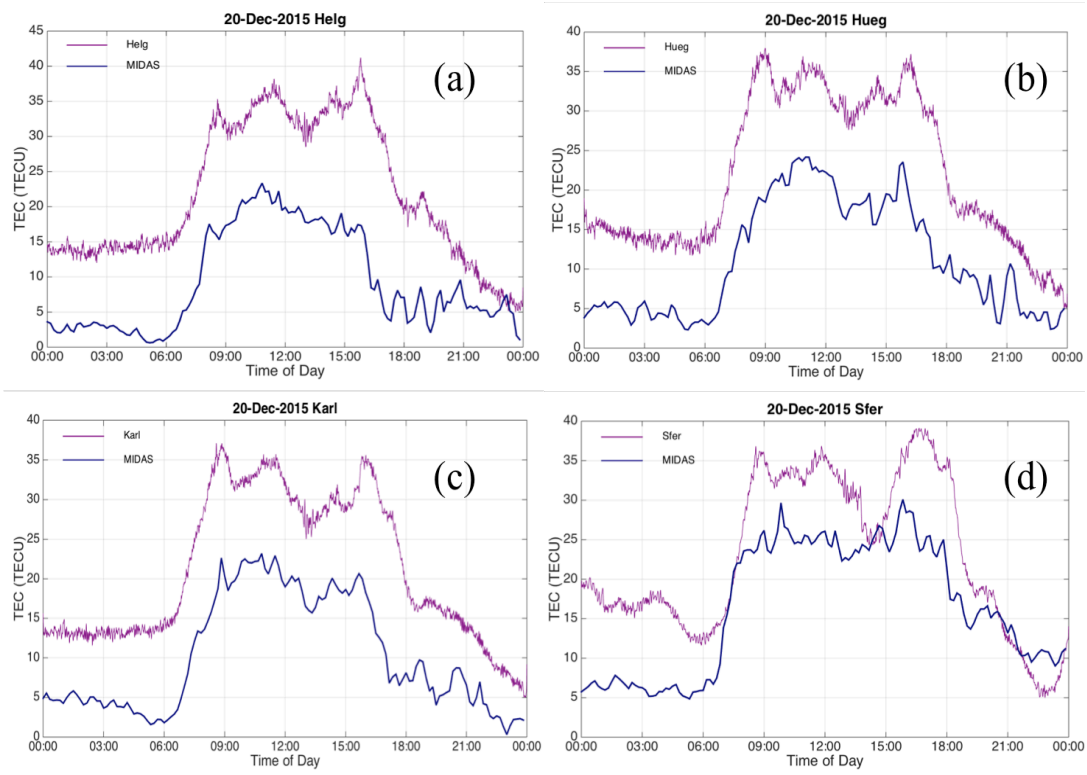

Figure 6.17: Direct comparisons between TEC derived at single frequency GPS receivers and TEC modeled by MIDAS at the closest available latitude and longitude (a) MIDAS and Helg (b) MIDAS and Hueg (c) MIDAS and Karl and (d) MIDAS and Sfer.

Figure 6.17 shows that in all four panels the shapes of the GPS and MIDAS TEC are similar. In all four panels the pairs of time series rise and fall similar at times. Small scale peaks and dips within the diurnal cycle are similar between pairs,

with the presence of a double diurnal maximum (DDM) suggested by both data sets in Figure 6.17 (b) and (c). In Figure 6.17 (d) the GPS TEC suggests a DDM which is not indicated by the MIDAS time series. An offset is seen between the GPS and MIDAS TEC with GPS TEC being higher than MIDAS TEC over most of the time series, which is present as MIDAS produces estimates of verticalised TEC whilst the GPS derived values are for slant TEC. The comparison here is to analyse the similarity of the overall shape and small-scale features rather than to compare numerical values.

Figure 6.17 (a), (b) and (c) show very good agreement between the shape of the GPS and MIDAS TEC. In Figure 6.17 (a) and Figure 6.17 (c) sunset is observed earlier in the MIDAS time series than in the GPS data, with a difference of roughly an hour in Figure 6.17 (a) and 30 minutes in Figure 6.17 (c). Figure 6.17 (d) shows the least good agreement between time series. In this panel there is roughly an hour discrepancy between sunrise times, and the TEC patterns after sunset are quite different, with the GPS TEC showing a larger range of values than MIDAS.

The good agreement between the GPS and MIDAS time series further suggests the new technique performs well in storm conditions.

6.5.6 Conclusions

On the case study day, the anti-correlation observed between foF2 and hmF2 was noticeably weaker at positive lags when compared to typical December data. Cross-correlations between foF2 and GPS derived TEC remained high at all four receiver locations but fell outside the 5^{th}-95^{th} percentile at each location. Cross-correlations between hmF2 and GPS TEC showed a strong anti-correlation which was typical when compared to December data. Cross-correlations between TEC derived at two different receivers remained strong, suggesting consistency and reliability of the new technique.

6.6 Chapter 6 discussion and chapter conclusions

In this chapter the correlation response to geomagnetic conditions was investigated. Analysis was conducted for all geomagnetically disturbed days from December 2010 to December 2015. 13 disturbed days were identified. In Section 6.4.1 cross-correlations between foF2 and hmF2 showed a range of responses over these days, ranging from typical correlations to a significant depletion in the strength of anticorrelation. Splitting the storm days by the time of day at which geomagnetic disruption was detected showed no consistent response for storms occurring at dawn or dusk, however when disturbed conditions were observed at both dawn and dusk a reduced anti-correlation between foF2 and hmF2 was seen at positive lags.

Investigations into storm-time cross-correlations between foF2 and GPS TEC in Section 6.4.2 showed that correlations remained strong, peaking above 0.8 on every disturbed day. Correlations between foF2 and GPS derived TEC on storm days in December are often similar to the median values for the month, and rarely fall outside the 5^{th} – 95^{th} percentile. The maximum deviation seen was observed only for a single storm day, which showed a cross-correlation of approximately 0.1 below the month's 5th percentile.

Cross-correlations between hmF2 and GPS TEC in storm conditions showed a range of responses, with one storm strengthening the anti-correlation between the parameters and another weakening the anti-correlation. These two responses were seen at 4 different receivers over almost all lags. For 5 of the 7 storm days in December 2015 the correlations between the parameters remained inside the 5^{th} - 95^{th} percentile of December observations across all lags, and at 3 out of the 4 receiver stations these 5 storm days also closely followed the median correlation response for the month. At some lags the anti-correlation weakening storm caused cross-correlation values to increase to a value above -0.5, such that the two parameters would not be considered anti-correlated.

Correlations between TEC derived at pairs of GPS receivers in Section 6.4.3 were high, peaking above a value of 0.8 on all storm days. Storm day correlations were also similar to the monthly median and only one storm day fell slightly outside the 5th -95th percentile for the month. The cross-correlations between both GPS TEC and ionosonde data and between pairs of TEC time series from different receivers suggest that the new technique produced consistent, sensible time series of TEC during multiple storm days and disturbed geomagnetic conditions. It should be noted that as GPS the dataset is so small (comprising only of December 2015) the conclusions drawn here should be examined over a longer time period before they can be stated with total confidence.

The storm which occurred on the 20/12/2015 was taken as a case study in Section 6.5 and was more thoroughly investigated. This was a strong storm with Kp values of 5 or above for 7 out of 8 daily recordings. The MIDAS model showed elevated TEC values across Europe and a tongue of ionisation heading poleward on the day of the storm. On the storm day the strength of the anti-correlation between foF2 and hmF2 was significantly reduced at positive lags compared to typical values from 6 Decembers data. foF2 and GPS derived TEC remained strongly correlated, peaking at a value above 0.8, with correlations falling slightly outside the 5th-95th percentile patch in positive lags at all four receiver locations. The strong correlation between these parameters is logical as the F2 region provides the biggest contribution to TEC values. Correlations between hmF2 and GPS TEC also remained typical during this storm, showing a strong anticorrelation peaking below -0.7 at all four receiver locations and

remaining within the 5th-95th percentile for almost all lags. Strong correlations were also observed between pairs of GPS receivers on the storm day. This suggests that the new technique produced reliable and consistent results during geomagnetically disturbed conditions at three separate receiver locations.

The first aim of the chapter was to determine if the correlation relationships identified in Chapter 4 held in geomagnetically disturbed conditions. The results of this chapter suggest that the answer to this is generally yes. Looking at multiple geomagnetically disturbed days however showed that there was no consistent cross-correlation response to geomagnetically disturbed conditions. This suggests that it isn't possible to deduce much information about storms from ionospheric cross-correlation results. The cross-correlations in geomagnetic conditions also suggest that the new TEC derivation technique using GPS satellites and single-frequency receivers remains reliable during disturbed conditions. The good agreement between new technique TEC time series and TEC modeled by MIDAS on the case study storm day further suggests that the new technique remains reliable in storm conditions. It should be remembered however that the size of the data set used here may make the results less robust.

Chapter 7

Conclusions

This EngD thesis aimed to advance the range of techniques available to investigate the ionosphere and to improve the confidence in those techniques. It was also concerned with the correlation between different ionospheric parameters to investigate the relationships between them. The thesis questions listed in Chapter 1 were as follows:

1. How well correlated are 24-hour time series of pairs of parameters observed by a single ionosonde?
2. Can ionospheric TEC be determined using a new method involving a geostationary satellite and a single frequency Global Positioning System (GPS) receiver?
3. Does cross-correlation validation imply that the new TEC derivation technique produces consistent, reliable results?
4. How well correlated are time series of TEC derived using this new method with time series of ionosonde parameters?
5. Do the correlation relationships identified hold for geomagnetically disturbed conditions?

7.1 How well correlated are 24-hour time series of pairs of parameters observed by a single ionosonde?

Chapter 4 investigated the relationships between the 24-hour time series of ionosonde observed foE, hmE, foF2 and hmF2 with a cross-correlation analysis using December data of 6 years. Cross-correlations were found between pairs of 24-hour time series for the F region, and 9am – 3pm time series for the E region, for both the raw data and the 24-hour time series data from which the diurnal cycle had been removed. This analysis found little correlation between pairs of E region parameters. Some correlation was found between foE and foF2, with a peak cross-correlation of 0.5 for 15% of the data. This peak occurs at a shifted lag of between 0 and -20 minutes, occurring as a result of the different times at which these variables reach peak values. A cross-correlation between foF2 and hmF2 over 24 hours showed a strong anti-correlation peaking at a cross-correlation of -0.8, which was sustained over lags of roughly 100 minutes.

The use of time series generated by IRI-2012 and IRI-2016 to remove the diurnal cycle from data was attempted, however it was found that there were large discrepancies between observational and model data. These discrepancies were seen to be largest at sunset and sunrise. Discrepancies were also seen on days when a double diurnal maximum was seen in observational data. Consequently, a smoothing technique was used to remove the diurnal cycle from data. However,

a cross-correlation analysis between pairs of parameter time series with the diurnal cycle removed showed little correlation outside of solar driving for most ionosonde parameter pairs. A cross-correlation of 0.8 was observed between the time series of foE and hmE when their diurnal cycle was removed. This peak was located at a lag of 0 minutes for approximately 20% of the data. This peak was observed for these parameter pairs at 2 different ionosondes. The scientific reason behind this relationship has not yet been identified.

Cross-correlations were also calculated for a single parameter observed at pairs of ionosondes within Europe. Correlations were high for foF2 between ionosondes, the peak value was above 0.9 and sustained for roughly 150 minutes, with correlations remaining above 0.5 for the full 180 minutes of analysis. Pairs of hmF2 were also highly correlated, peaking above 0.8, but showed a greater variation in the time for which peak correlations were sustained, ranging from approximately 50 minutes for 2 ionosonde pairs and closer to 100 minutes for the other 2 pairs. Peak foE correlations were again high with a peak value above 0.8 sustained for 20 to 30 minutes, falling rapidly with correlations remaining above 0.5 for only 20 to 40 minutes after the peak. Cross-correlations between hmE time series and at ionosonde pairs showed almost no large (above 0.4) correlation. A shift was observed in the lag location of peak correlations between all ionosonde to ionosonde correlations for foE, foF2 and hmF2, caused by the local solar time differences between ionosondes.

The parameters hmF2 and foF2 showed a strong, sustained anti-correlation. Time series of E region parameters appear to not be very well correlated with any other parameters, in either the E or F region. The lack of correlation found between parameters once the diurnal cycle had been removed suggests that the majority of the correlation seen between raw time series is the result of solar forcing. However, one parameter pair without the diurnal cycle, foE and hmE, showed a high correlation. Ionosonde parameters are also found to be highly correlated with identical parameters at a different location. The parameters foF2, hmF2, foE were highly correlated at pairs of ionosondes, however hmE time series were not. The lack of correlation between hmE time series may be caused by the fact the time series were shrunk to only 9am-3pm, removing the major part of the diurnal pattern from the time series.

7.2 Can ionospheric TEC be determined using a new method involving a geostationary satellite and a single frequency Global Positioning System (GPS) receiver?

In Chapter 5 this thesis demonstrated a new technique allowing 24-hour time series of relative TEC to be derived using a signal transmitted between a geostationary satellite and a single frequency terrestrial GPS receiver. This new technique is advantageous as it opens up a new potential data source, providing time series of relative TEC along a fixed path through the ionosphere. This data

could be assimilated into ionospheric products in the future, improving observation coverage.

An initial visual inspection of the produced slant TEC time series showed the results were sensible at three ground receivers and had similar diurnal variations with some similar short-term features.

The new technique has a potential source of error due to clock drift. The receivers used in the study which were not linked to an atomic clock were observed to have a timing drift in their derived raw TEC time series in the order of tens of nanoseconds over 24 hours. A linear detrending removed this drift from the final time series.

7.3 Does cross-correlation validation imply that the new TEC derivation technique produces consistent, reliable results?

In Chapter 5 a cross-correlation analysis was conducted between pairs of 24-hour TEC time series derived for different ground receivers for the same day for all usable days in 2015. Cross-correlations were high, peaking above a value of 0.9, with the peak attained at a shift away from time 0, caused by local solar time difference between receiver locations.

Cross-correlations were also found between GPS derived TEC and ionosonde observed TEC. Unlike the analysis completed for question 7.1, these correlations were performed purely to validate the new technique, and not to investigate parameter behaviour. The correlations were observed to be high consistently over a year, with a shift again caused by time difference. Correlations between pairs of GPS receivers in geomagnetically disturbed conditions remained high, similar to the month's median correlations with only one storm day outside the 5-95th percentile patch. The high correlations between pairs of GPS receivers and between GPS receivers and ionosondes suggests that the new technique continues to perform reliably and accurately in geomagnetically disturbed conditions. The size of the data set used for this analysis however means that this conclusion cannot be stated with absolute certainty.

The validation demonstrated that the technique was able to produce realistic, sensible time series of relative TEC on a routine basis.

7.4 How well correlated are time series of TEC derived using this new method with time series of ionosonde parameters?

In Chapter 4 a cross-correlation analysis was conducted between time series of ionosonde parameters and time series of TEC obtained using the new technique. For E region parameters a peak of 0.5 was observed between TEC and foE, and no correlation was observed between TEC and hmE. High correlation was observed between GPS derived TEC and foF2, with a peak above 0.9 sustained

for approximately 50 minutes. This relationship was expected as the F region is the densest part of the ionosphere and thus provides the biggest contribution towards TEC measurements. A strong anticorrelation was observed between hmF2 and GPS TEC with a peak of -0.8 sustained for approximately 100 minutes. As foF2 and hmF2 are strongly anti-correlated, and foF2 contributes strongly towards TEC values, an anti-correlation between hmF2 and TEC is logical. This suggests that time series of E region ionosonde parameters are not noticeably correlated with GPS derived TEC, but that F region ionosonde parameters are strongly correlated with GPS derived TEC.

No significant correlation was observed between ionosonde parameters and GPS derived TEC when the diurnal cycle had been removed from both parameters' time series. This suggests that foF2 and hmF2 are both strongly correlated with GPS derived TEC, and that the dominant cause for the high correlations is solar driving.

7.5 Do the correlation relationships hold for geomagnetically disturbed conditions?

The correlation response to geomagnetic conditions was also investigated, to see if the previously identified relationships held. The cross-correlation analysis was repeated for all identified geomagnetically disturbed days from December 2010 to December 2015. 13 days were identified that met the requirements. There was no consistent response to the cross-correlations between foF2 and hmF2, with some storm days showing typical correlations (compared to previous analysis over 6 Decembers' data) to a significant depletion in the strength of anticorrelation. The storm days were then split by time of day at which the storm occurred. No consistent response was seen for storms occurring at either dawn or dusk, however a storm covering both times of day caused the strength of the anti-correlation between the two parameters to be reduced at positive lags.

The cross-correlation analysis between ionosonde foF2 and GPS derived TEC (using the new technique) was also repeated for storm conditions. Only data from the year 2015 was available which allowed the response on 7 disturbed days to be examined. Cross-correlations between the parameters remained strong in disturbed conditions, always peaking above a value of 0.8. The cross-correlations were also often similar to the month's median values and rarely fell outside the 5^{th} - 95^{th} percentile. One storm showed a greater deviation than the others, but still only fell outside the 5-95^{th} percentile by a value of roughly 0.1. Cross-correlations between hmF2 and GPS TEC showed no consistent response, with a strengthening of the anti-correlation observed for one storm and a weakening for another such that the parameters were no longer considered anti-correlated (above -0.5). For the other 5 storm days cross-correlations stayed inside the 5^{th} - 95^{th} percentile patch at all lags and were often similar to the median correlations. As discussed in section 7.3, the cross-correlations between time series of TEC

measurements from pairs of GPS receivers also remained high in geomagnetically disturbed conditions.

The strongest storm, with Kp values of 5 or above for 7 out of 8 daily recordings was taken as a case study. On the case study storm day MIDAS showed elevated TEC values over Europe. A weakened anti-correlation was observed between foF2 and hmF2 at positive lags, correlations between foF2 and GPS TEC remained strong but moved outside the 5^{th}-95^{th} percentile at positive lags. Cross-correlations of hmF2 and GPS TEC remained typical, remaining within the 5^{th}-95^{th} percentile across most lags. The TEC measurements of pairs of GPS receivers remained strongly correlated. Comparing time series of GPS derived TEC time series for the case study day and TEC time series modelled by MIDAS for the same day, latitude and longitude, showed good agreement. This further supports the conclusion that the new technique continues to perform accurately in geomagnetically disturbed conditions.

Regarding the question 'Do the correlation relationships identified hold for geomagnetically disturbed conditions?', the answer is generally yes. However when geomagnetically disturbed conditions do cause a change in correlation behaviour there is no consistent response, suggesting correlation results themselves cannot imply much information about a storm. The strongest correlated pairs of parameters identified throughout this study are: foF2 and hmF2; foF2 and GPS TEC; hmF2 and GPS TEC. Strong correlations were seen between foF2 and GPS TEC, and strong anticorrelations between hmF2 and foF2, and between hmF2 and GPS TEC.

7.6 Quick overview

Correlation investigations in the ionosphere usually focus on analysing foF2 or TEC. This project was more comprehensive and included E region analysis, a study connecting the E and F regions, investigating the hmF2 / foF2 correlations, a study of the time-lagged correlations, and a study of the correlations with the diurnal cycle removed. The analysis demonstrated the dominance of the diurnal cycle in ionospheric correlations, and also showed discrepancies between IRI model outputs and ionosonde observations. The analysis also showed that correlations between foF2 and hmF2 and between hmF2 and GPS TEC showed no consistent response to storm conditions, whilst foF2 and GPS TEC remained strongly correlated.

The analysis is a powerful new tool that enables the analysis of new datasets including TEC derived using geostationary satellites and single frequency GPS receivers. The analysis shows that the new technique routinely produces reliable TEC time series, both in calm and geomagnetically disturbed conditions. The time series also show good agreement with ionosonde observations. The results

suggest that the new technique can confidently be used for ionospheric applications.

7.7 Potential further work

The analysis conducted here has been focused on six different Decembers' data for ionosondes, and either a year or a single December for GPS derived TEC. Consequently, it would be beneficial to repeat the analysis using a larger dataset. It would also be interesting to repeat the analysis in different seasons to see if the correlation relationships identified are unchanged, as most of this study used observations made in Northern hemisphere winter. In particular for the storm-time analysis conducted in Chapter 6, a larger dataset would make the results more robust, while for the new technique validation conducted in Chapter 5, a larger data set would help to demonstrate the robustness of the technique. Repeating the analysis using several years' data would be advantageous.

It would also be interesting to extend this investigation to include ionosonde observed extraordinary wave parameters. Both have random variations which are caused by features such as TIDs, so correlating for example foF2 with fxF2 could be interesting to see if there are any factors which influence one but not the other. In addition, repeating the cross-correlation analysis using extraordinary waves, for example fxF2 with hmF2 and fxF2 with GPS TEC, would hopefully reinforce the results found here.

In regards to the new GPS TEC derivation technique, a beneficial extension to this work would be to refine the technique by which invalid days data are discarded. In this initial validation the data of entire days were automatically discarded if there was a single problem within the 24-hour time series. The assessment was made manually by eye. A useful future project therefore would be firstly to find a way to automatically and reliably identify and reject missing and discontinuous data, and secondly to repair any time series where cycle slips have caused discontinuities. If repairing the time series is not possible, it is still possible that several hours of the time series are usable and only some of the data for that day needs to be discarded rather than the whole 24 hours. Data are also discarded if 15% or more of the data are missing, meaning that hypothetically 85% of a day could be usable. It is possible that a significant amount of data could be recoverable if a more skilful method was developed for discarding poor quality data whilst recovering usable data. In addition to this, clock drift should be further investigated across the different GPS receiver types to determine its impact, and potential techniques for mitigation should be identified.

As the new technique has been demonstrated to be capable of routinely producing reliable results, another interesting extension would be to incorporate the data into an existing assimilative model. By comparing the performance of the model using only current data, and the model using the new observational

data as well as current data, the impact of the new observations on the accuracy of nowcasts and forecasts could be analysed.

References

Ahrens, C.D., 2009. *Meteorology Today: An Introduction to Weather, Climate and the Environment* Ninth Edit., Brooks/Cole.

Akmaev, R.A., Juang, H.- & H, M., 2008. Using enthalpy as a prognostic variable in atmospheric modelling with variable composition. *Quarterly Journal of the Royal ...*, 134, pp.2193–2197. Available at: http://onlinelibrary.wiley.com/doi/10.1002/qj.71/abstract.

Amin, M.M., 2015. *Influence of lightning on electron density variation in the ionosphere using WWLLN lightning data and GPS data*. University of Cape Town.

Amin, M.M., Inggs, M. & Cilliers, P.J., 2014. Influence of lightning on total electron content in the ionosphere using WWLLN lightning data and GPS data. In *Proceedings of SAIP2014*.

Angling, M.J., 2008. First assimilations of COSMIC radio occultation data into the Electron Density Assimilative Model (EDAM). *Annales Geophysicae*, 26(2), pp.353–359. Available at: http://www.ann-geophys.net/26/353/2008/.

Appleton, E. V. & Barnett, M.A.F., 1925. On Some Direct Evidence for Downward Atmospheric Reflection of Electric Rays. *Proceedings of the Royal Society A: Mathematical, Physical and Engineering Sciences*, 109(752), pp.621–641. Available at: http://rspa.royalsocietypublishing.org/cgi/doi/10.1098/rspa.1925.0149.

Austen, J.R., Franke, S.J. & Liu, C.H., 1988. Ionospheric imaging using computerized tomography. *Radio Science*, 23(3), p.299.

Barlier, F. et al., 1978. A thermospheric model based on satellite drag data. *Annales de Geophysique*, 34, pp.9–24.

Barry, R.G. & Chorley, R.J., 2003. *Atmosphere, Weather and Climate* Eighth Edi., Routledge.

Baumjohann, W. & Treumann, R.A., 2011. *Basic Space Plasma Physics*, Imperial College Press.

Bernhardt, P. a. et al., 1998. Two-dimensional mapping of the plasma density in the upper atmosphere with computerized ionospheric tomography (CIT). *Physics of Plasmas*, 5(5), p.2010. Available at: http://scitation.aip.org/content/aip/journal/pop/5/5/10.1063/1.872872 [Accessed October 20, 2014].

Beyerle, G. et al., 2005. GPS radio occultation with GRACE: Atmospheric profiling utilizing the zero difference technique. *Geophysical Research Letters*, 32(13), pp.1–5.

Bilitza, D., 1990. International Ionosphere Reference 1990.

Bilitza, D. et al., 2017. International Reference Ionosphere 2016: From ionospheric climate to real-time weather predictions. *Space Weather*, 15(2), pp.418–429.

Bilitza, D. et al., 2014. The International Reference Ionosphere 2012 – a model of international collaboration. *Journal of Space Weather and Space Climate*, 4, p.A07. Available at: http://www.swsc-journal.org/10.1051/swsc/2014004.

Bilitza, D. et al., 2011. The international reference ionosphere today and in the future. *Journal of Geodesy*, 85(12), pp.909–920.

Browne, S., Hargreaves, J.K. & Honary, B., 1995. An imaging riometer for ionospheric studies. *Electronics & Communication Engineering Journal*,

7(5), pp.209–217. Available at: http://eprints.lancs.ac.uk/9824/.
Bruinsma, S., 2015. The DTM-2013 thermosphere model. *Journal of Space Weather and Space Climate*, 5, p.A1. Available at: http://www.swsc-journal.org/10.1051/swsc/2015001.
Bruyninx, C. et al., 2012. Enhancement of the EUREF permanent network services and products. *International Association of Geodesy Symposia*, 136, pp.27–34.
Buonsanto, M.J., 1999. Ionospheric storms – a review. *Space Science Reviews*, 88, pp.563–601.
Burns, A.G. et al., 1995. Large enhancements in the O/N2 ratio in the evening sector of the winter hemisphere during geomagnetic storms. *Journal of Geophysical Research*, 100671(1), pp.661–14.
Bust, G.S. et al., 2007. Four-dimensional GPS imaging of space weather storms. *Space Weather*, 5(2), p.S02003. Available at: http://www.agu.org/pubs/crossref/2007/2006SW000237.shtml [Accessed May 13, 2013].
Bust, G.S., Coco, D.S. & Gaussiran, T.L.I., 2001. Computerized ionospheric tomography analysis of the Combined Ionospheric Campaign. , 36(6), pp.1599–1605.
Bust, G.S., Garner, T.W. & Gaussiran, T.L., 2004. Ionospheric Data Assimilation Three-Dimensional (IDA3D): A global, multisensor, electron density specification algorithm. *Journal of Geophysical Research: Space Physics*, 109(A11), pp.1–14.
Bust, G.S. & Mitchell, C.N., 2008. History, current state, and future directions of ionospheric imaging. *Reviews of Geophysics*, 46(2006), pp.1–23.
Cerruti, A.P., Ledvina, B.M. & Kintner, P.M., 2006. Scattering height estimation using scintillating wide area augmentation system/satellite based augmentation system and GPS satellite signals. *Radio Science*, 41(6), pp.1–8.
Chapman, S., 1931. The absorption and dissociative or ionizing effect of monochromatic radiation in an atmosphere on a rotating earth. *Proceedings of the Physical Society*, 43(1), pp.26–45.
Chartier, A.T. et al., 2015. Modeled and observed equatorial thermospheric winds and temperatures. *Journal of Geophysical Research: Space Physics*, 120(7), pp.5832–5844.
Chartier, A.T., Jackson, D.R. & Mitchell, C.N., 2013. A comparison of the effects of initializing different thermosphere- ionosphere model fields on storm time plasma density forecasts. *Journal of Geophysical Research: Space Physics*, 118(October), pp.7329–7337.
Coster, A.J. et al., 2017. GNSS Observations of Ionospheric Variations During the 21 August 2017 Solar Eclipse. *Geophysical Research Letters*, 44(24), p.12,041-12,048.
Da Dalt, F. et al., 2014. Implementation of a new ionospheric model (ANIMo) into a three-dimensional variational analysis (3D-Var) for imaging and forecasting purposes. *2014 XXXIth URSI General Assembly and Scientific Symposium (URSI GASS)*, pp.1–4. Available at: http://www.scopus.com/inward/record.url?eid=2-s2.0-84919740705&partnerID=tZOtx3y1.
Dandenault, P.B. & Richards, P.G., 2015. The collapse of the midnight ionosphere and behavior of meridional neutral winds at Townsville over a

full solar cycle. *Journal of Geophysical Research: Space Physics*, 120(11), pp.9826–9838.
Daniels, F.B., 1956. *Electromagnetic propagation studies with a satellite vehicle, ch.30, Scientific uses of earth satellites* J. A. Van Allen, ed., Рипол Классик.
Daniels, F.B. & Bauer, S.J., 1959. The ionospheric faraday effect and its applications. *Journal of the Franklin Institute*, 267.
Davies, K., 1990. *Ionospheric Radio (No. 31)*, Peter Peregrinus Ltd.
Davis, C., 1998. Basic Ionosonde Theory. Available at: https://www.ukssdc.ac.uk/ionosondes/ionosonde_basics.html [Accessed August 8, 2018].
Dellinger, J.H., 1937. Sudden disturbances of the ionosphere. *Proceedings of the Institute of Radio Engineers*, 25(10), pp.111–142.
Denton, M.H., Ulich, T. & Turunen, E., 2009. Modification of midlatitude ionospheric parameters in the F2 layer by persistent high-speed solar wind streams. *Space Weather*, 7(4), pp.1–10.
Dobbin, A.L., 2005. *Modelling studies of possible coupling mechanisms between the upper and middle atmosphere*.
Dominici, P., 1998. My first fifty years in ionospheric research.
Dow, J.M., Neilan, R.E. & Rizos, C., 2009. The International GNSS Service in a changing landscape of Global Navigation Satellite Systems. *Journal of Geodesy*, 83(3–4), pp.191–198.
Elemo, E.O., 2015. Cross Correlation Analysis of Mozambique's 7.0 M Earthquake Using the Empirical Mode Decomposition. *Open Access Library Journal*, pp.1–8.
Fesen, C.G., 1997. Theoretical effects of tides and auroral activity on the low latitude ionosphere. *Journal of Atmospheric and Solar-Terrestrial Physics*, 59(13), pp.1521–1532.
Forbes, J.M. et al., 2008. Tidal variability in the ionospheric dynamo region. *Journal of Geophysical Research: Space Physics*, 113(2), pp.1–17.
Forbes, J.M. et al., 1997. Upper atmosphere tidal oscillations due to latent heat release in the tropical troposphere. *Annales Geophysicae*, 15(9), pp.1165–1175.
Forbes, J.M., Palo, S.E. & Zhang, X., 2000. Variability of the ionosphere. *Journal of Atmospheric and Solar-Terrestrial Physics*, 62(8), pp.685–693.
Ford, E. et al., 2008. Statistical analysis of thermospheric gravity waves from Fabry-Perot Interferometer measurements of atomic oxygen. *Annales Geophysicae*, pp.29–45. Available at: http://discovery.ucl.ac.uk/144961/.
Ford, E.A.K. et al., 2006. Thermospheric gravity waves in Fabry-Perot interferometer measurements of the 630.0 nm OI line. *Ann. Geophys.*, 24(2), pp.555–566. Available at: http://www.ann-geophys.net/24/555/2006/.
Fremouw, E.J. & Secan, J.A., 1992. Applicaton of stochastic inverse theory to ionospheric tomography. *Radio Science*, 27, pp.721–732.
Fuller-Rowell, T.J. et al., 2002. Storm-time changes in the upper atmosphere at low latitudes. *Journal of Atmospheric and Solar-Terrestrial Physics*, 64(12–14), pp.1383–1391.
Gardiner, G.W., 1969. Origin of the Term Ionosphere. *Nature*, 224, p.1096. Available at: http://dx.doi.org/10.1038/2241096a0.
Giday, N.M. & Katamzi-Joseph, Z.T., 2018. Performance of MIDAS Over East African Longitude Sector: Case Study During 4–14 March 2012 Quiet to

Disturbed Geomagnetic Conditions. *Space Weather*, 16(2), pp.126–137.
Giday, N.M., Katamzi, Z.T. & McKinnell, L.A., 2016. Ionospheric tomography over South Africa: Comparison of MIDAS and ionosondes measurements. *Advances in Space Research*, 57(1), pp.245–256. Available at: http://dx.doi.org/10.1016/j.asr.2015.08.017.
Gordon, W.E., 1958. Incoherent Scattering of Radio Waves by Free Electrons with Applications to Space Exploration by Radar. *Proceedings of the IRE*, 46(11), pp.1824–1829.
Haarlem, M.P. Van et al., 2013. Astrophysics LOFAR : The LOw-Frequency ARray. *Astronomy and Astrophysics*, 556, p.A2.
Hagan, M.E. & Forbes, J.M., 2003. Migrating and nonmigrating semidiurnal tides in the upper atmosphere excited by tropospheric latent heat release. *Journal of Geophysical Research: Space Physics*, 108(A2), pp.1–14.
Hajj, G.A. et al., 1994. Imaging the ionosphere with the global positioning system. *International Journal of Imaging Systems and Technology*, 5(2), pp.174–187. Available at: http://doi.wiley.com/10.1002/ima.1850050214.
Hajj, G.A. & Romans, L.J., 1998. Ionospheric electron density profiles obtained with the Global Positioning System: Results from the GPS/MET ecperiment. *Radio Sci*, 33(1), pp.175–190.
Hargreaves, J.K., 1992. *The solar-terrestrial environment*, Cambridge University Press.
Hargreaves, J.K., 1979. *The Upper Atmosphere and Solar-Terrestrial Relations*, Van Nostrand Reinhold Company Ltd.
Hayes, L.A. et al., 2017. Pulsations in the Earth's Lower Ionosphere Synchronized With Solar Flare Emission. *Journal of Geophysical Research: Space Physics*, 122(10), pp.9841–9847.
Hein, W.Z., Goto, Y. & Kasahara, Y., 2016. Estimation Method of Ionospheric TEC Distribution using Single Frequency Measurements of GPS Signals. *International Journal of Advanced Computer Science and Applications*, 7(12), pp.1–6.
Hocke, K. & Schlegel, K., 1996. A review of atmospheric gravity waves and travelling ionospheric disturbances: 1982–1995. *Annales Geophysicae*, 14(9), p.917.
Huang, X. & Reinisch, B.W., 2001. Vertical electron content from ionograms in real time. *Radio Science*, 36(2), pp.335–342.
Immel, T.J. et al., 2006. Control of equatorial ionospheric morphology by atmospheric tides. *Geophysical Research Letters*, 33(15), pp.2–5.
Immel, T.J. et al., 2001. Dayside enhancements of thermospheric O/N2 following magnetic storm onset. *Journal of Geophysical Research*, 106488(1), pp.471–15.
Jayawardena, T.S.P. et al., 2015. Imaging the topside ionosphere and plasmasphere with ionospheric tomography using COSMIC GPS TEC. *Journal of Geophysical Research: Space Physics*, pp.817–831.
Jin, H. et al., 2011. Vertical connection from the tropospheric activities to the ionospheric longitudinal structure simulated by a new Earth's whole atmosphere-ionosphere coupled model. *Journal of Geophysical Research: Space Physics*, 116(1), pp.1–9.
Van De Kamp, M.M.J.L., 2013. Medium-scale 4-D ionospheric tomography using a dense GPS network. *Annales Geophysicae*, 31(1), pp.75–89.
Kaplan, E.D. & Hegarty, C.J., 2006. *Understanding GPS: Principles and*

Applications Second Edi., Artech House.
Katamzi, Z., 2011. *Statistical Analysis of Ionospheric Total Electron Content*. University of Bath.
Kelley, M.C., 2009. *The Earth's Ionosphere, Plasma Physics and Electrodynamics* Second Edi., Academic Press, Elsevier.
Killeen, T.L., 1987. Energetics and Dynamics of the Earth's Thermosphere. *Reviews of Geophysics*, 25, pp.433–454.
Killeen, T.L. et al., 1984. Ion-neutral coupling in the high-latitude F region Evaluation of ion heating terms from Dynamics Explorer 2. , 89, pp.7495–7508.
Kinrade, J. et al., 2012. Ionospheric scintillation over Antarctica during the storm of 5-6 April 2010. *Journal of Geophysical Research: Space Physics*, 117(5), pp.1–23.
Kivelson, M.G. & Russell, C.T. eds., 1995. *Introduction To Space Physics*, Cambridge University Press.
Klimenko, M. V. et al., 2011. Ionospheric effects of geomagnetic storms at mid latitudes. *Russian Journal of Physical Chemistry B*, 5(3), pp.377–386. Available at: http://link.springer.com/10.1134/S1990793111030092.
Kotake, N. et al., 2011. Statistical Study of Medium-Scale Traveling Ionospheric Disturbances Observed with a GPS Receiver Network in Japan BT - Aeronomy of the Earth's Atmosphere and Ionosphere. *Aeronomy of the Earth's Atmosphere and Ionosphere*, 59(21), pp.291–299. Available at: http://www.springerlink.com/index/P5VW37879TG7620H.pdf%5Cnfile:///Users/jklenzi/Documents/Papers2/Books/2011/Otsuka/Otsuka 2011.pdf%5Cnpapers2://publication/uuid/1DCECE4C-FF14-48E5-8FE6-B9E7D458D24D.
Kouris, S.S. et al., 2004. TEC and foF2 variations: preliminary results. *Annals of Geophysics*, 47(August), pp.1325–1332.
Kunitsyn, V.E. et al., 2015. Ionospheric TEC estimation with the signals of various geostationary navigational satellites. *GPS Solutions*, 20(4), pp.877–884.
Laštovička, J., 2006. Forcing of the ionosphere by waves from below. *Journal of Atmospheric and Solar-Terrestrial Physics*, 68(3–5), pp.479–497.
Lei, J. et al., 2008. Observations and simulations of the ionospheric and thermospheric response to the December 2006 geomagnetic storm: Initial phase. *Journal of Geophysical Research: Space Physics*, 113(1), pp.1–15.
Leick, A., 2004. *GPS Satellite Surveying* Third Edit., John Wiley & Sons.
Leitinger, R., Schmidt, G. & Tauriainen, A., 1975. An evaluation method combining the differential Doppler measurements from two stations that enables the calculation of the electron content of the ionosphere. *Zeitschrift fuer Geophysik*, 41(2), pp.201–213.
Liu, H.L. et al., 2018. Development and Validation of the Whole Atmosphere Community Climate Model With Thermosphere and Ionosphere Extension (WACCM-X 2.0). *Journal of Advances in Modeling Earth Systems*, 10(2), pp.381–402.
Liu, H.L. et al., 2010. Ionospheric variability due to planetary waves and tides for solar minimum conditions. *Journal of Geophysical Research: Space Physics*, 115(6), pp.1–13.
Liu, J.Y. et al., 2001. Variaions of ionospheric total electron content during the Chi-Chi earthquake. *Geophysical Research Letters*, 28(7), p.86400.

Lowell Digisonde International, Instrument Description, Background to Ionospheric Sounding. Available at: http://www.digisonde.com/instrument-description.html [Accessed August 8, 2018].
Lu, G. et al., 2012. Ionospheric and thermospheric variations associated with prompt penetration electric fields. *Journal of Geophysical Research: Space Physics*, 117(8), pp.1–14.
Luhmann, J.G., 1983. Ionospheric disturbances resulting from ion-neutral coupling. *Space Science Reviews*, 34(3), pp.337–346.
Lühr, H., Häusler, K. & Stolle, C., 2007. Longitudinal variation of F region electron density and thermospheric zonal wind caused by atmospheric tides. *Geophysical Research Letters*, 34(16), pp.1–4.
Makela, J.J. et al., 2012. Large-scale measurements of thermospheric dynamics with a multisite fabry-perot interferometer network: Overview of plans and results from midlatitude measurements. *International Journal of Geophysics*, 2012(3).
Maltseva, O. & Mozhaeva, N., 2016. The Use of the Total Electron Content Measured by Navigation Satellites to Estimate Ionospheric Conditions. , 2016.
Mannucci, A.J. et al., 1998. A global mapping technique for GPS-derived ionospheric total electron content measurements. *Radio Science*, 33(3), pp.565–582.
Mannucci, A.J. et al., 2005. Dayside global ionospheric response to the major interplanetary events of October 29-30, 2003 “Halloween Storms.” *Geophysical Research Letters*, 32(12), pp.1–4.
Mannucci, A.J. et al., 1999. *GPS and Ionosphere* March 1999. W. R. Stone, ed., Oxford Univeristy Press.
Marsh, D.R. et al., 2013. Climate change from 1850 to 2005 simulated in CESM1(WACCM). *Journal of Climate*, 26(19), pp.7372–7391.
Matsushita, S., 1959. A study of the morphology of ionospheric storms. *Journal of Geophysical Research*, 64(3), pp.305–321. Available at: http://doi.wiley.com/10.1029/JZ064i003p00305 [Accessed October 16, 2017].
McKinnell, L.A., Opperman, B. & Cilliers, P.J., 2007. GPS TEC and ionosonde TEC over Grahamstown, South Africa: First comparisons. *Advances in Space Research*, 39(5), pp.816–820.
McNamara, L.F. & Wilkinson, P.J., 2009. Spatial correlations of foF2 deviations and their implications for global ionospheric models: 1. Ionosondes in Australia and Papua New Guinea. *Radio Science*, 44(2), p.n/a-n/a. Available at: http://doi.wiley.com/10.1029/2008RS003955.
McNamara, L.P., 1991. *Ionosphere: Communications, Surveillance and Direction Finding*, Krierger Publishing Company.
Meggs, R.W. & Mitchell, C.N., 2006. A study into the errors in vertical total electron content mapping using GPS data. *Radio Science*, 41(1), pp.1–8.
Mendillo, M., 2006. Storms in the ionosphere: Patterns and processes for total electron content. *Reviews of Geophysics*, 44(RG4001), pp.1–47.
Meyer-Vernet, N., 2007. *Basics of the Solar Wind*, Cambridge University Press.
Mitchell, C.N. et al., 2005. GPS TEC and scintillation measurements from the polar ionosphere during the October 2003 storm. *Geophysical Research Letters*, 32(12), pp.1–4.
Mitchell, C.N. & Spencer, P.S.J., 2003. A three-dimensional time-dependent

algorithm for ionospheric imaging using GPS. *Annals of Geophysics*, 46, pp.687–696.
Mosert, M., Ezquer, R. & Scida, L.A., 2002. Relations Between Critical Frequency foF2 and Total Electron Content. In *PROCEEDINGS OF THE IRI TASK FORCE ACTIVITY 2001*. p. 95.
Mrak, S. et al., 2018. Direct EUV / X-Ray Modulation of the Ionosphere During the August 2017 Total Solar Eclipse. *Geophys. Res. Lett.*, (2018), pp.1–9.
Muella, M.T.A.H. et al., 2011. Tomographic imaging of the equatorial and low-latitude ionosphere over central-eastern Brazil. *Earth, Planets and Space*, 63(2), pp.129–138. Available at: http://link.springer.com/10.5047/eps.2010.12.011.
Nava, B., Coïsson, P. & Radicella, S.M., 2008. A new version of the NeQuick ionosphere electron density model. *Journal of Atmospheric and Solar-Terrestrial Physics*, 70(15), pp.1856–1862.
Nicolls, M.J. et al., 2004. Imaging the structure of a large-scale TID using ISR and TEC data. *Geophysical Research Letters*, 31(9), pp.2–5.
Oliver, W.L., Kawamura, S. & Fukao, S., 2008. The causes of mid-latitude F layer behavior. *Journal of Geophysical Research: Space Physics*, 113(8), pp.1–14.
Panasenko, S. V. et al., 2018. Traveling ionospheric disturbances observed by Kharkiv and Millstone Hill incoherent scatter radars near vernal equinox and summer solstice. *Journal of Atmospheric and Solar-Terrestrial Physics*, 172, pp.10–23. Available at: https://doi.org/10.1016/j.jastp.2018.03.001.
Pedatella, N.M. et al., 2014. Ionosphere variability during the 2009 SSW: Influence of the lunar semidiurnal tide and mechanisms producing electron density variability. *Journal of Geophysical Research: Space Physics*, 119(5), pp.3828–3843.
Pedatella, N.M. & Forbes, J.M., 2010. Evidence for stratosphere sudden warming-ionosphere coupling due to vertically propagating tides. *Geophysical Research Letters*, 37(11), pp.1–5.
Pfister, W., 1956. *Study of Fine Structure and Irregularities of the Ionosphere with Rockets and Satellites, ch.31, Scientific uses of earth satellites* J. A. Van Allen, ed., Рипол Классик.
Pi, X.Q. et al., 1993. Diurnal Double Maxima Patterns in the F-Region Ionosphere - Substorm-Related Aspects. *J Geophys Res-Space Phys*, 98, pp.13677–13691.
Picone, J.M., 2002. NRLMSISE-00 empirical model of the atmosphere: Statistical comparisons and scientific issues. *Journal of Geophysical Research*, 107(A12), p.1468. Available at: http://doi.wiley.com/10.1029/2002JA009430.
Piggott, W.R. & Rawer, K. eds., 1978. *U.R.S.I. Handbook of Ionogram Interpretation and Reduction* Second Edi., World Data Center A for Solar-Terrestrial Physics.
Pulinets, S. a. et al., 2004. Correlation analysis technique revealing ionospheric precursors of earthquakes. *Natural Hazards and Earth System Science*, 4(5/6), pp.697–702.
Ratcliffe, J.A., 1972. *An introduction to the ionosphere and magnetosphere*, Cambridge University Press.
Reinisch, B.W. & Galkin, I.A., 2011. Global Ionospheric Radio Observatory (GIRO). *Earth, Planets, and Space,*, 63, pp.377–381.

Reinisch, B.W. & Huang, X., 2001. Deducing Topside Profiles and Total Electron Content From Bottomside Ionograms. *Advances in Space Research*, 27(1), pp.23–30.
Richmond, a. D., Ridley, E.C. & Roble, R.G., 1992. A thermosphere/ionosphere general circulation model with coupled electrodynamics. *Geophysical Research Letters*, 19(6), p.601.
Ridley, A.J., Deng, Y. & Tóth, G., 2006. The global ionosphere–thermosphere model. *Journal of Atmospheric and Solar-Terrestrial Physics*, 68(8), pp.839–864. Available at: http://linkinghub.elsevier.com/retrieve/pii/S1364682606000071.
Rishbeth, H., 1988. Basic physics of the ionosphere: a tutorial review. *Journal of the Institution of Electronic and Radio Engineers*, 58(6S), p.S207.
Rishbeth, H., 1998. How the thermospheric circulation affects the ionospheric F2-layer. *Journal of Atmospheric and Solar-Terrestrial Physics*, 60(14), pp.1385–1402.
Rius, A., Ruffini, G. & Cucurull, L., 1997. Improving the vertical resolution of ionospheric tomography with GPS occultations. *Geophysical Research Letters*, 24(18), pp.2291–2294.
Rocken, C. et al., 2000. COSMIC system description. *Terrestrial, Atmospheric and Oceanic Sciences*, 11(1), pp.21–52.
Röttgering, H., 2003. LOFAR, a new low frequency radio telescope. *New Astronomy Review*, 47, pp.405–409. Available at: http://adsabs.harvard.edu/abs/2003NewAR..47..405R.
Sardon, E., Rius, A. & Zarraoa, N., 1994. Estimation of the transmitter and receiver differential biases and the ionospheric total electron content from Global Positioning. *Radio Science*, 29(3), pp.577–586.
Sato, T., 1957. Disturbances in the Ionospheric F2 Region Associated with Geomagnetic Storms II. Middle Latitudes. *Journal of geomagnetism and geoelectricity*, 9, pp.1–22.
Schmidt, T. et al., 2004. GPS radio occultation with CHAMP: An innovative remote sensing method of the atmosphere. *Advances in Space Research*, 33(7), pp.1036–1040.
Schunk, R.W. et al., 2004. Global Assimilation of Ionospheric Measurements (GAIM). *Radio Science*, 39(1), p.n/a-n/a. Available at: http://doi.wiley.com/10.1029/2002RS002794.
Shim, J.S. et al., 2008. Spatial correlations of day-to-day ionospheric total electron content variability obtained from ground-based GPS. *Journal of Geophysical Research: Space Physics*, 113(9), pp.1–14.
Smith, A.M. et al., 2008. GPS scintillation in the high arctic associated with an auroral arc. *Space Weather*, 6(3), pp.1–7.
Space Weather Prediction Centre (SWPC), G2 (Moderate) Geomagnetic Storms Observed on 20 December. Available at: http://www.swpc.noaa.gov/news/g2-moderate-geomagnetic-storms-observed-20-december.
Space Weather Prediction Centre (SWPC), Planetary K-Index. Available at: https://www.swpc.noaa.gov/products/planetary-k-index.
Space Weather Prediction Centre (SWPC), Planetary K-Index.
Space Weather Prediction Centre (SWPC), 2015a. Space Weather Highlights 14 December - 20 December 2015. Available at: http://legacy-www.swpc.noaa.gov/weekly/pdf/prf2103.pdf.

Space Weather Prediction Centre (SWPC), 2015b. Space Weather Highlights 23 November - 29 November.
Spencer, P.S.J., 2014. Ionospheric precursors to scintillation activity. *Annals of Geophysics*, 57(1), p.A0185. Available at: http://www.annalsofgeophysics.eu/index.php/annals/article/view/6389.
Tascione, T.F., 1994. *Introduction to the Space Environment* Second Edi., Krierger Publishing Company.
Thomas, J.O., 1963. Canadian Satellite : The Topside Sounder Alouette. *Science*, pp.229–232.
Tsugawa, T., Saito, A. & Otsuka, Y., 2004. A statistical study of large-scale traveling ionospheric disturbances using the GPS network in Japan. *Journal of Geophysical Research: Space Physics*, 109(A6), pp.1–11.
Vadas, S.L., 2007. Horizontal and vertical propagation and dissipation of gravity waves in the thermosphere from lower atmospheric and thermospheric sources. *Journal of Geophysical Research: Space Physics*, 112(6), pp.1–23.
Vadas, S.L. & Fritts, D.C., 2005. Thermospheric responses to gravity waves: Influences of increasing viscosity and thermal diffusivity. *Journal of Geophysical Research D: Atmospheres*, 110(15), pp.1–16.
Vasyliunas, V.M. & Song, P., 2005. Meaning of ionospheric Joule heating. *Journal of Geophysical Research: Space Physics*, 110(A2), pp.1–8.
Verhulst, T.G.W. & Stankov, S.M., 2017. Height-dependent sunrise and sunset: Effects and implications of the varying times of occurrence for local ionospheric processes and modelling. *Advances in Space Research*, 60(8), pp.1797–1806.
Vierinen, J. et al., 2014. Beacon satellite receiver for ionospheric tomography. *Radio Science*, 49(12), pp.1141–1152.
Wright, C.J. et al., 2017. Exploring gravity wave characteristics in 3-D using a novel S-transform technique: AIRS/Aqua measurements over the Southern Andes and Drake Passage. *Atmospheric Chemistry and Physics*, 17(13), pp.8553–8575.
Yiğit, E. et al., 2018. Critical frequencies of the ionospheric F1and F2layers during the last four solar cycles: Sunspot group type dependencies. *Journal of Atmospheric and Solar-Terrestrial Physics*, 171(December 2017), pp.157–163.
Yin, P. et al., 2017. A multiresolution inversion for imaging the ionosphere. *Journal of Geophysical Research: Space Physics*, 122(6), pp.6799–6811.
Yin, P., 2004. Ionospheric electron concentration imaging using GPS over the USA during the storm of July 2000. *Geophysical Research Letters*, 31(12), p.L12806. Available at: http://doi.wiley.com/10.1029/2004GL019899 [Accessed November 26, 2014].
Yue, X. et al., 2014. Space Weather Observations by GNSS Radio Occultation: From FORMOSAT-3/COSMIC to FORMOSAT-7/COSMIC-2. *Space Weather*.
Zhang, S.P. & Shepherd, G.G., 2002. Neutral winds and O (1S) emission rates in the lower thermosphere as measured with WINDII/UARS during the April 4–5th 1993 and February 1994 geomagnetic storms. , 64(March 1979), pp.1201–1214.
Zhang, S.R. et al., 2017. Ionospheric Bow Waves and Perturbations Induced by the 21 August 2017 Solar Eclipse. *Geophysical Research Letters*, 44(24), p.12,067-12,073.

Zolesi, B. & Cander, L.R., 2014. *Ionospheric prediction and forecasting*, Springer.